Weak Lensing Flexion as a Probe of Galaxy Cluster Substructure

by

Benjamin Martin Cain

B.S., University of Wisconsin (2004)

Submitted to the Department of Physics
in partial fulfillment of the requirements for the degree of

Doctor of Philosophy

at the

MASSACHUSETTS INSTITUTE OF TECHNOLOGY

February 2011

Author .....
Department of Physics
November 16, 2010

Certified by .....
Marshall W. Bautz
Senior Research Scientist/Associate Director, MIT Kavli Institute
Thesis Supervisor

Certified by .....
Enectali Figueroa-Feliciano
Assistant Professor of Physics
Thesis Supervisor

Accepted by .....
Krishna Rajagopal
Chairman, Physics Department Committee on Graduate Theses

Weak Lensing Flexion as a Probe of Galaxy Cluster Substructure

by

Benjamin Martin Cain

Submitted to the Department of Physics
on November 16, 2010, in partial fulfillment of the
requirements for the degree of
Doctor of Philosophy

Abstract

Measuring galaxy cluster total masses and the amount of dark matter substructure within galaxy cluster haloes is a fundamental probe of the ΛCDM model of structure formation, as well as the interactions between baryonic and non-baryonic matter. In this thesis I approach the topic of cluster mass structure in two ways. With a combination of optical imaging, spectroscopy, and X-ray observations I determine that the cluster RCS043938-2904.7, while apparently anomalous initially due to its high optical richness and low X-ray surface brightness, is in fact an association of structures along the line of sight. Accounting for this structure brings the observed cluster properties into agreement with known scaling relations. I also present a novel method for measuring weak gravitational lensing flexion to inform mass measurements on small scales. While previously published methods for measuring flexion focus on measuring derived properties of the lensed images, such as shapelet coefficients or surface brightness moments, my method fits a fully mass-sheet-invariant parametrized Analytic Image Model (AIM) to the each galaxy image. This simple parametric model traces the distortion of lensed image isophotes. I tested the AIM method using simulated data images with realistic noise and a variety of input image properties, and I show that it successfully reproduces the input lensing fields. I also apply the AIM method for flexion measurement to Hubble Space Telescope observations of Abell 1689, and detect mass structure in that cluster using only flexion measured with the AIM method.

Thesis Supervisor: Marshall W. Bautz
Title: Senior Research Scientist/Associate Director, MIT Kavli Institute

Thesis Supervisor: Enectali Figueroa-Feliciano
Title: Assistant Professor of Physics

Acknowledgments

As with any big project, there are many people who have helped me along the way. I can't thank everyone who's buoyed me along individually, but I appreciate you all.

I would like to thank my advisor Mark Bautz for all his support. Mark was the first person from MIT that I spoke with after being accepted, though neither of us realized the connection until we'd been working together for two months. He has always been available when I've needed advice, and has allowed me the freedom to cut my own path with this project. I also want to thank Paul Schechter for his deep insights on the many problems I encountered along the way, for his pushing me to excellence and precision.

I also need to thank George Elbaum. During my first year as a graduate student I was supported as a Whiteman Fellow, a graduate fellowship endowed by George. The support and freedom from that fellowship allowed me to get my feet under me in graduate school, and let me explore all of the many research opportunities at MIT.

My thanks also go out to my friends at MKI, at the Muddy Charles Pub, and everywhere else. In particular my classmates Robyn Sanderson and Andrew Grier, who have been great friends throughout the entire grad school process. We've often relaxed together over a cold beer and a hot meal, which was essential to my survival.

I am also deeply indebted to my family. My brothers Jack, Mike, and Brian have been busy for years working on their own great accomplishments and always push me to keep up. And, of course, my mother. Patty has always encouraged me to excel and has always given me the tools to do it. I have gotten to where I am, doing what I love, thanks in no small part to her.

And finally, I'd like to thank my wife Natalie. We've both been keen on science as long as we've known each other, and her deep interest and passion for her own research has inspired me more times than I can count. Her love and support has gotten me through a lot of challenges, and has made me that much more excited about tackling whatever is around the corner. Thank you, Natalie, and I love you.

Contents

List of Figures

List of Tables

Chapter 1

Introduction

1.1 Galaxy Clusters

The largest gravitationally bound objects in the universe are galaxy clusters. They form in the rare, highest-density regions of the universe and are tracers of the most massive perturbations of the primordial density field. Because of this, galaxy clusters are important astrophysical laboratories for cosmological investigations.

The existence of dark matter was first posited after inconsistencies between the observed luminous mass and the cluster member galaxy velocity dispersions were observed (Zwicky, 1937), and it was later found to be essential for explaining not only the structure of galaxy clusters, but also the anisotropies in the cosmic microwave background radiation (e.g., Dunkley et al., 2009). The observed cosmic expansion history confirms a much higher matter content in the universe than is observed in luminous baryons (e.g., Astier et al., 2006; Mantz et al., 2008; Vikhlinin et al., 2009; Mantz et al., 2010). Measurements of the number density and mass of galaxy clusters puts significant constraints on cosmological parameters via comparison to the cluster mass function, and measurements of mass substructure within galaxy clusters test the ΛCDM paradigm when compared to numerical simulations and theoretical predictions (e.g., Jenkins et al., 2001; Tinker et al., 2008).

In order to use galaxy clusters as a cosmological probe, it is necessary to measure their mass. The mass function of galaxy clusters, particularly in the high mass limit,

is very sensitive to Ω_m and σ_8 (e.g., Wen et al., 2010, particularly Figure 6). The state of the field has reached a level of precision where significant discrepancies between X-ray and gravitational lensing mass estimates have been observed, leading to estimates of the line-of-sight structure of galaxy clusters (e.g. Peng et al., 2009; Newman et al., 2009).

In addition to their cosmological significance as a class of objects, galaxy clusters are also powerful probes for basic physics. By mass, galaxy clusters are dark matter dominated, and their baryonic mass is dominated by an extremely rarified ($n_e \sim 10^{-3}$ cm^{-3}), high temperature ($kT_e \sim 1 - 10$ keV), X-ray luminous plasma. Both of these conditions make galaxy clusters a singular astrophysical laboratory for studying the interaction between baryonic and non-baryonic matter, as well as a laboratory for plasma physics in extreme conditions.

The combination of data from multiple techniques (such as the Sunyaev-Zel'dovich effect, X-ray imaging spectroscopy, gravitational lensing, stellar kinematics, and/or galaxy kinematics) can constrain the mass distribution over many scales and can determine the line-of-sight structure of galaxy clusters (Newman et al., 2009; Peng et al., 2010, and others), and comparing the X-ray surface brightness, cluster member galaxy distribution and the weak-lensing measured total mass distribution in the "Bullet Cluster" 1E 0657-558 provided some of the strongest evidence for the existence of dark matter to date (Clowe et al., 2006).

Galaxy clusters are interesting objects, both astrophysically and cosmologically, and measuring their mass distributions is an important part of understanding them. Though the use of Sunyaev-Zel'dovich measurements to measure cluster masses has grown in recent years (Brodwin et al., 2010; Mason et al., 2010), the primary tools for studying galaxy cluster mass structure are X-ray imaging spectroscopy and gravitational lensing, both of which are topics of this thesis. I will postpone a discussion X-ray observations, as it is well covered in Chapter 2. In the rest of this chapter I will describe the formalism for gravitational lensing which will be used in this thesis.

1.2 Gravitational Lensing

Gravitational lensing is a well described physical process and a full treatment of the subject is beyond the scope of this thesis. For a more complete overview and a derivation of the lensing equations presented here starting from the theory of General Relativity, see the review article by Bartelmann & Schneider (2001). For the purpose of this thesis, I will discuss only a few major elements which are essential to the material presented in Chapter 3 and beyond.

Gravitational lensing preserves surface brightness. Because all photons from a lensed image follow geodesics, the phase-space density of the photons is unchanged as a consequence of Liouville's Theorem. This photon phase space density,

$$f(\vec{x},\vec{p}) = \frac{dN}{d^3\vec{x}d^3\vec{p}} \tag{1.1}$$

can be directly related to the surface brightness as a function of the frequency ν,

$$I_\nu = \frac{dE}{dAd\Omega d\nu dt}, \tag{1.2}$$

by noting that for photons $dN = dE/h\nu$, $d^3\vec{x} = dA\ cdt$, and $d^3\vec{p} = p^2\ dp\ d\Omega = (h^3\nu^2/c^3)\ d\nu\ dt$, so

$$I_\nu = \frac{h^4\nu^3}{c^2} f. \tag{1.3}$$

f is unaffected by lensing, and therefore neither is I_ν. This conservation of phase space density implies that the observed surface brightness of a lensed image at a given position is equal to the surface brightness that would have been observed at the corresponding location of that image if there had been no lensing.

It is useful to consider gravitational lensing as a coordinate transformation between two sky planes - the *source plane*, which is the image which would have been observed if there were no lensing, and the *image plane*, the image which is observed in fact. A third plane, the *lens plane*, at the location of the lens, is also useful for relating the lensing transformation to the mass density of the astrophysical lens. The surface brightness at a position in the image plane is equal to the surface brightness at the

corresponding position in the source plane. If the transformation between the image plane position $\vec{\beta}$ and the source plane position $\vec{\theta}$ is a well defined function $\vec{\beta}(\vec{\theta})$, then the observed surface brightness is given by

$$I_{\rm obs}(\vec{\theta}) = I_{\rm src}(\vec{\beta}(\vec{\theta})). \tag{1.4}$$

The physics of gravitational lensing are contained in the conservation of surface brightness and in the relationship between the source plane and image plane coordinates. A diagram of basic gravitational lensing geometry is presented in Figure 1-1.

Gravitational lensing is induced by mass, and for a projected surface mass density $\Sigma(\vec{\theta})$ the projected lensing potential $\psi(\vec{\theta})$ is defined by

$$\psi(\vec{\theta}) = \frac{1}{\pi}\int \mathrm{d}^2\theta' \frac{\Sigma(\vec{\theta'})}{\Sigma_c} \ln|\vec{\theta} - \vec{\theta'}|, \tag{1.5}$$

where

$$\Sigma_c = \frac{c^2}{4\pi G}\frac{D_S}{D_L D_{LS}} \tag{1.6}$$

is the critical lensing surface mass density which depends on the cosmological angular diameter distances to the source (D_S), to the lens (D_L) and between the lens and the source (D_{LS}). See, e.g., Hogg (2000) for formulae to calculate these distances in a variety of cosmologies. In this formulation is the assumption that the lens can be approximated as a thin lens at a discrete distance from the observer, meaning that the significant mass is confined to a region which is much narrower along the line of sight than any of the distances D_L, D_S, or D_{LS}. The ratio of the surface mass density to the critical value is called the convergence, $\kappa(\vec{\theta})$, and is related to the potential ψ in Equation 1.5 by the two-dimensional Poisson Equation: $\nabla^2\psi = 2\kappa$.

The lensing transformation $\vec{\beta}(\vec{\theta})$ is defined in terms of the lensing deflection $\vec{\delta}\left(\vec{\theta}\right) = \nabla\psi\left(\vec{\theta}\right)$ as

$$\vec{\beta}\left(\vec{\theta}\right) = \vec{\theta} - \vec{\delta}\left(\vec{\theta}\right). \tag{1.7}$$

Equations 1.4, 1.5, and 1.7 describe the effect of lensing from a specific mass distribution on the observed surface brightness profile.

1.2.1 Complex Formalism

The mathematical description of gravitational lensing, particularly that of weak lensing, is most compactly presented in complex notation. Vector quantities on a two dimensional plane can be represented as complex numbers, where $\vec{x} = x_1\hat{e_1} + x_2\hat{e_2}$ becomes $x = x_1 + ix_2$. The complex conjugate is denoted by a starred quantity (e.g., x^* for the conjugate of x). Derivative operations are also be described with complex operations: The gradient operator ∇ becomes $\partial = \partial_1 + i\partial_2$. With this formalism, the lensing transformation for complex positions β and θ is

$$\beta(\theta) = \theta - \partial\psi(\theta) = \theta - \delta(\theta). \tag{1.8}$$

The convergence is a real-valued field derived from the real valued $\psi(\theta)$

$$\kappa(\theta) = \frac{1}{2}\partial^*\partial\psi(\theta) = \frac{1}{2}\partial^*\delta. \tag{1.9}$$

In discussing weak lensing (see below) it is useful to define other lensing fields using derivatives of ψ. These fields have different spin properties. A field f has spin-m if a local coordinate rotation about the image by an angle ϕ is equivalent to transforming $f \to f' = fe^{-im\phi}$. The conjugate of a field of spin-m is spin-$(-m)$. Vector quantities (such as position, or the derivative operator) are spin-1, and real valued fields (such as κ) are spin-0.

1.2.2 Strong Lensing & Weak Lensing

Gravitational lensing in application is usually divided into two regimes - strong lensing and weak lensing. Strong lensing refers to the regime where light from a single source (at a single position β) is lensed to form images at multiple image positions θ. With multiple images of the same source, δ can be constrained. For extended source objects, such as galaxies, each resolution element that is identified in multiple images provides further constraint on the positional dependence of δ.

Weak lensing refers to the regime where only a single image of each background

source is observed. Lensing information is obtained by measuring the shape distortions of the source objects, and therefore requires the sources to be intrinsically extended. For weak lensing, the lensing equation (Equation 1.7) is expanded in small deviations about the observed image center. In weak lensing it is typically assumed that $\kappa \ll 1$ and the lensing equation is linearized about the image center θ_0. Doing so yields

$$\beta(\theta) = \beta(\theta_0) + \Delta\beta = \theta_0 - \delta(\theta_0) + (1-\kappa)\Delta\theta - \gamma\Delta\theta^* + \mathcal{O}(\Delta\theta^2). \tag{1.10}$$

Here I have introduced $\gamma = \frac{1}{2}\partial\partial\psi$, the spin-2 shear field. Both κ and γ are evaluated at θ_0 and are constant with respect to a small position offset $\Delta\theta$.

For weak lensing applications, the constant-order solution,

$$\beta(\theta_0) = \theta_0 - \delta(\theta_0), \tag{1.11}$$

is satisfied but $\beta(\theta_0)$ and $\delta(\theta_0)$ are unmeasurable, as there are no additional images to constrain the source-plane position. In this case, the second order lensing distortions are the source of information about the lensing fields. The local lensing equation is then

$$\Delta\beta = (1-\kappa)\Delta\theta - \gamma\Delta\theta^* + \mathcal{O}(\Delta\theta^2) \tag{1.12}$$

and it characterizes the distortion of galaxy image shapes by the lensing potential. These distortions depend only on the curvature of the lensing potential and affect the observed ellipticity of the lensed galaxies.

As was introduced by Goldberg & Natarajan (2002) and refined in Goldberg & Bacon (2005), this expansion can be extended beyond linear-order to include two additional lensing fields known as *flexion*[1]. Expanding the lensing equation to

[1]Other authors, including Goldberg & Bacon (2005), refer to flexion as "second-order weak lensing". To be consistent with a full description of gravitational lensing, I refer to the displacement of images by a potential gradient as first-order lensing, shear and magnification as second-order lensing, and flexion as third-order lensing. The order of a lensing effect thus matches the derivatives of ψ on which it depends.

quadratic/third-order yields

$$\Delta\beta = (1-\kappa)\Delta\theta - \gamma\Delta\theta^* - \frac{1}{4}\mathcal{F}^*\Delta\theta^2 - \frac{1}{2}\mathcal{F}\Delta\theta\Delta\theta^* - \frac{1}{4}\mathcal{G}(\Delta\theta^*)^2 + \mathcal{O}(\Delta\theta^3). \quad (1.13)$$

Consider a resolved, circular image. The lensing transformation described in Equation 1.11 displaces the image center, the lensing transformation in Equation 1.12 distorts the circle into a magnified ellipse, and the lensing transformation described in Equation 1.13 will additionally distort the ellipse into the familiar "arclet" or "banana" shape seen in many lensing systems. See Figure 1-2 for images of arclets in an HST data image of Abell 1689 (the dataset will be described in more detail in Chapter 5).

The flexion field $\mathcal{F}$ is called *first flexion* or *1-flexion*, and $\mathcal{G}$ is *second flexion* or *3-flexion*. I use the latter designations because the 1 and 3 refer to the spin properties of the flexion fields: 1-flexion is a vector field and 3-flexion is a spin-3 field. $\mathcal{F}$ and $\mathcal{G}$ are the two complex derivatives of the shear field, with $\mathcal{F} = \partial^*\gamma$ and $\mathcal{G} = \partial\gamma$, and furthermore the 1-flexion field is the gradient of the convergence:

$$\mathcal{F} = \partial^*\gamma = \partial^*\left(\frac{1}{2}\partial^2\psi\right) = \partial\left(\frac{1}{2}\partial\partial^*\psi\right) = \partial\kappa. \quad (1.14)$$

This relationship makes the connection between flexion and the mass distribution very clear. Though the combination of the derivatives is different and not as directly relatable to the surface mass density, 3-flexion independently constrains the mass distribution as well, assuming that it is equally well measured (Bacon et al., 2006).

Unlike the shear and convergence fields, the flexion fields are not unitless. Flexion has the units of inverse-angles, and the product of the image size Θ and the magnitude of the flexion $|\mathcal{F}|$ or $|\mathcal{G}|$ is a unitless quantity which characterizes the contribution of flexion to the coordinate tranformation.

1.2.3 Mass-Sheet Invariant Lensing

Because the source position β is not constrained in weak lensing, the images are subject to the mass-sheet degeneracy described by Falco et al. (1985). This degeneracy

implies that measurements of κ can only be constrained to a family of solutions, where $\kappa' = \lambda\kappa + 1 - \lambda$ is also valid for any real value of κ, equivalent to rescaling the source plane relative to the image plane by a factor of λ while maintaining the same critical curves (locations where $\kappa = 1$). Constraints from lensing properties only apply to quantities which are invariant under such a mass-sheet transformation, and therefore any weak lensing measurement must be quantified in terms of mass-sheet invariant parameters. This mass-sheet degeneracy extends to the flexion fields, as well as any possible higher-order lensing fields which are locally measured. Breaking the mass-sheet degeneracy and relating the observed lensing fields to the true physical lensing fields requires the source plane scale to be fixed using information from multiple images, or by fixing the distance to one or more sources and to the lens. Strong lensing intrinsically constrains the position of the unlensed source position with the multiple observed image positions, meaning that the scale of the source plane is fixed. This breaks the mass-sheet degeneracy.

For both second-order and third-order weak gravitational lensing, the transformation can be reparametrized to include only those parameter combinations which are invariant under the mass-sheet transformation. Equation 1.13 has seven parameters to define $\Delta\beta$ in terms of $\Delta\theta$. Instead of referring to the true source plane and its coordinates, I refer to a rescaled version of it with coordinates $\Delta\bar{\beta} = \Delta\beta/(1-\kappa)$, following Schneider & Er (2008). *Reduced shear* (g), and *reduced flexions* (Ψ_1 and Ψ_3) are defined as:

$$g = \frac{\gamma}{1-\kappa}, \tag{1.15}$$

$$\Psi_1 = \frac{\mathcal{F}}{4(1-\kappa)}, \tag{1.16}$$

$$\Psi_3 = \frac{\mathcal{G}}{4(1-\kappa)}. \tag{1.17}$$

With these definitions, the third-order lensing transformation becomes

$$\Delta\bar{\beta} = \Delta\theta - g\Delta\theta^* - \Psi_1^*\Delta\theta^2 - 2\Psi_1\Delta\theta\Delta\theta^* - \Psi_3(\Delta\theta^*)^2. \tag{1.18}$$

See Figure 1-3 for a depiction of the effect of each of the three lensing fields individually as well as together. All of the physically measurable shear and flexion information is quantified in the reduced shear, reduced 1-flexion and reduced 3-flexion, and the seventh parameter corresponding to the mass-sheet scaling λ has been eliminated. Ψ_1 and Ψ_3 can also be defined in terms of g, $\partial^* g$, and ∂g, though the formulation presented here is simpler (Schneider & Er, 2008).

From this point forward in this thesis, when referring to shear I will be implicitly referring to the reduced shear, and likewise with flexion for reduced flexion. In referring back to γ, $\mathcal{F}$, or $\mathcal{G}$, I will call them *physical shear* and *physical flexion* to distinguish them. Additionally, from here onward I will assume that on an image-by-image basis the lensing fields are defined at the origin of the lensing coordinates and I will only consider a domain of the lensing transformation where the flexion terms remain small with respect to the image scale Θ. This means that the unitless quantity $D_n = |\Psi_n|\Theta \ll 1$ for both $n = 1$ and $n = 3$.

1.3 Thesis Structure

The rest of this thesis is structured as follows. Chapter 2 describes my published work on the measurement of line-of-sight structure in the cluster RCS043938-2904.7 using a combination of X-ray and optical spectroscopy observations. The remainder of the thesis focuses on a new method of weak lensing analysis with flexion: the Analytic Image Model (AIM) method. Chapter 3 describes the AIM method in detail and its implementation for this work; Chapter 4 describes the process I used to validate the method with simulated data images; and Chapter 5 describes the application of the AIM method to a Hubble Space Telescope dataset of Abell 1689. A1689 is an extremely well-studied galaxy cluster across all wavelengths, and serves as an observational testbed for the AIM method. I show that AIM is successful in measuring galaxy cluster substructure in A1689 using an adaptation of a flexion aperture mass statistic. In Chapter 6 I summarize the results and present future goals and directions to extend the applicability of the AIM method.

1.4 Figures

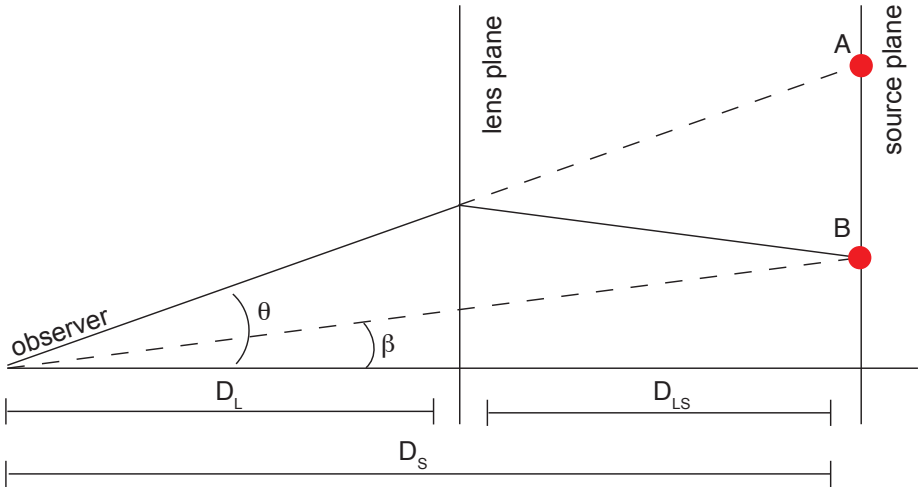

Figure 1-1: A schematic of the geometry of a gravitational lensing system, assuming that the lensing occurs at a single, thin plane along the line of sight. The solid, bent line indicates the actual path of a single light ray and the solid horizontal line is the axis through the center of the lens system. To an observer, the source appears at a position θ in the image plane (the red dot labelled A), though if there had been no lensing the source image would have formed at β in the image plane (indicated by the red dot labelled B). The angular diameter distances D_L, D_S, and D_{LS} are also labelled.

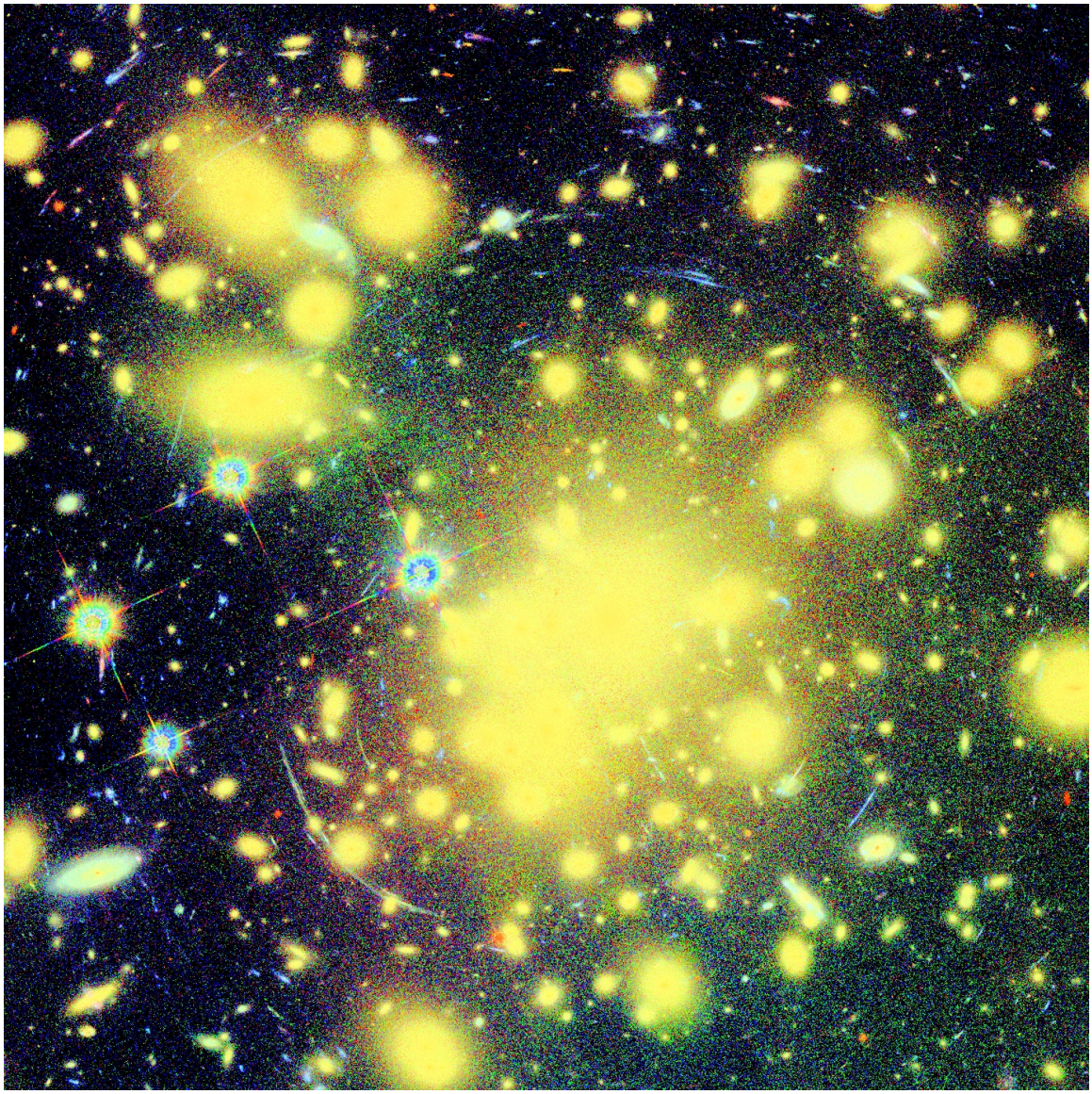

Figure 1-2: The central region of Abell 1689 has many lensing arcs which are easily identified by eye. They differ in color (either bluer or redder) and in morphology (thin and arced) from the large, yellow, elliptical cluster members in this image. For reference, north is up and east is to the left, and the image is 145″ on a side.

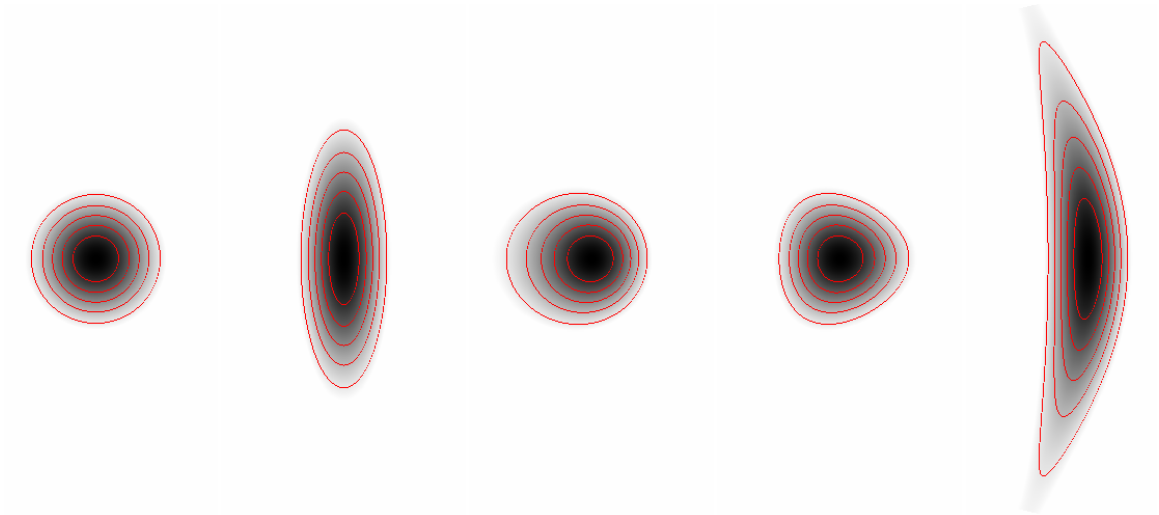

Figure 1-3: A decomposition of the effect of each lensing field. Going left to right: An unlensed, circular image; the circular image with shear; the circular image with 1-flexion; the circular image with 3-flexion; and the circular image with all three lensing fields combined. Note that in the 1-flexion and 3-flexion images the field has been exaggerated to make the effect more apparent on its own.

Chapter 2

RCS043938-2904.7: A Case Study in Galaxy Cluster Substructure

2.1 Preface

The content of this chapter was published as *Evidence for line-of-sight structure in a comparison of X-ray and optical observations of the high-redshift cluster RCS043938-2904.7* (Cain et al., 2008). The paper is reproduced here in full as a motivation for the importance of accurately measuring mass structure in galaxy clusters.

2.2 Introduction

There is considerable interest in measuring the evolution of the galaxy cluster mass function with redshift. In principle, such a measurement can test structure formation and constrain the cosmic expansion history. One of the observational challenges in such an undertaking is to identify all clusters in a particular volume; the other is to reliably infer cluster mass from observable cluster properties, over a range of cluster redshifts. Recent optical surveys, such as the Red-Sequence Cluster Survey (RCS, Gladders & Yee, 2005); and the Sloan Digital Sky Survey (e.g., Koester et al., 2007) have found large numbers of clusters at moderate to high redshift, with $0.2 \lesssim z \lesssim 1$ and $0 < z \lesssim 0.3$, respectively. At the high redshift extent, where

spectroscopic information can be difficult to obtain on a survey scale, various optical properties, such as richness or optical luminosity, can be taken to be mass proxies, and have been shown to be strongly correlated with observables understood to be related to cluster mass, such as galaxy velocity dispersion and X-ray temperature (e.g., Yee & Ellingson, 2003; Lin et al., 2003; Popesso et al., 2004; Lopes et al., 2006). In order to use optical richness (or any other optical property) as a mass proxy, understanding the evolution of the mass-richness relation is critical to extracting cosmological information, since any evolution in the relation must be separated from the evolution of the mass function. In particular, some care must be taken when attempting to extend the mass/observable relation to high redshift as many of these relations are computed using local data.

Previous work has shown that optically-selected, high-redshift clusters at a fixed optical richness are typically lower in temperature and underluminous in X-rays when compared to local clusters (Hicks et al., 2005; Gilbank et al., 2004; Lubin et al., 2002; Donahue et al., 2001). Since these clusters generally follow the local luminosity-temperature relationship, the low temperatures and luminosities are interpreted as an indication that the cluster galaxies are not in virial equilibrium with the X-ray emitting gas. However, it is important to account for the significant scatter in the relation between optical richness and X-ray luminosity, as an Eddington-like bias will scatter points of lower than expected X-ray luminosity into an optically-selected sample (e.g., Bower et al., 1994). Observing these high redshift clusters is thus an avenue to study how clusters approach equilibrium.

RCS043938-2904.7 is part of a larger sample of high redshift, high richness RCS clusters selected for X-ray follow up observations. X-ray properties of the sample as a whole are described in a forthcoming paper by Hicks et al. (2008). Here we present *Chandra* X-ray observations and optical spectroscopy of this apparently rich, X-ray underluminous object. In §2 we describe the X-ray data reduction and analysis. In §3 we compare mass estimates from the X-ray data to the known mass-temperature and mass-richness relations in literature. In §4 we describe the optical spectroscopy, in §5 we discuss our results and we summarize in §6. Throughout the paper we take

a standard ΛCDM cosmology with $H_0 = 70$ km s^{-1} Mpc^{-1}, $\Omega_m = 0.3$ and $\Omega_\Lambda = 0.7$. At the cluster redshift, $z = 0.9558$, $1''$ corresponds to a metric distance of 6.64 kpc. Errors are indicated with 90% confidence intervals unless otherwise noted.

2.3 X-ray observations & data analysis

2.3.1 Reduction

The X-ray data consists of two *Chandra* ACIS-S3 observations. A log of the observations of RCS043938-2904.7 is presented in Table 2.1. Both observations were performed in the VFAINT mode, and the CTI correction was applied with a focal plane temperature of -120°C. Data reduction was done using CIAO version 3.2 tools and CALDB 3.3.0 starting with level 2 event lists from the standard *Chandra* pipeline.

The first observation of RCS043938-2904.7 (obsid 3577) had a highly variable background and the second observation was kindly provided by the Director of the *Chandra* X-ray Center to compensate. This second observation (obsid 4438) had a low background and was analyzed by standard lightcurve methods to select the acceptable background rate intervals, keeping 28.7 ks of the total 28.8 ks. More care had to be taken with obsid 3577 because standard lightcurve methods eliminated more than three-quarters of the data as unusable.

In order to maximize the useful portion of the data, we took the following approach. We binned the data into 100-second segments and sorted them from lowest number of counts to highest number of counts. We assume that the cluster flux is constant in time. This means that the signal-to-noise ratio is highest in the bin with the least number of counts and lowest in the bin with the most counts. Suppose then that there are S signal counts in each bin and C_n total counts in the first n bins. Since C_n monotonically increases with n, we want to find the lowest value of n for which

$$\frac{Sn}{\sqrt{C_n}} > \frac{S(n+1)}{\sqrt{C_{n+1}}}, \tag{2.1}$$

or equivalently,

$$n > \frac{1}{\sqrt{\frac{C_{n+1}}{C_n}} - 1}, \tag{2.2}$$

meaning that adding the data in the $(n+1)^{\text{th}}$ bin will reduce the total signal-to-noise ratio in our filtered data set. This determined the time intervals we included in our final data set independent of the source count rate. In total, 64.6 ks of the total 76.2 ks of data (85%) from obsid 3577 were kept. These data were combined with the second observation (obsid 4438) using the CIAO script `merge_all` for a total good-data exposure time of 93.3 ks. The same script was used to create an exposure map and exposure-corrected image.

The X-ray data were then filtered to the energy range of 0.3-7 keV and point sources were identified and removed using `wavdetect`. Pulse-height spectra and associated response files were created from a 100 pixel (49.2″) radius circular region around the X-ray centroid. Background spectra were obtained from another 100 pixel radius circular region over 400 pixels (196.8″) away from the cluster center, though still from the same merged image. Care was taken to choose the background region in a location where the two observations overlapped. Spectral analysis was performed using XSPEC version 12.2.0 (Arnaud, 1996), and cluster emission was modeled as an optically-thin thermal plasma (Mewe et al., 1985, 1986). The redshift was fixed at the value determined from optical spectroscopy and the heavy element abundance was fixed at 0.3 times Solar abundance (Anders & Grevesse, 1989). An attempt was made to determine the metal abundances, but the data do not provide a significant constraint. The spectral model also included Galactic photoabsorption. The nH FTOOL from NASA's HEASARC (Dickey & Lockman, 1990) was used to fix the column density of HI. Spectra were binned so that a minimum of 20 counts were in each energy bin.

2.3.2 Temperature, surface brightness, mass profile & gas mass fractions

The best fit temperature, fluxes and luminosities (with 90% confidence intervals) are listed in Table 2.2. The bolometric luminosity was estimated by integrating the model spectra between 0.05 and 50 keV, and over the 49.2″ radius aperture. The corresponding metric aperture radius at the cluster redshift is 391 kpc for RCS043938-2904.7.

We extracted a radial profile of the cluster emission from the exposure-corrected image. Point sources were removed using the CIAO script `dmfilth` and a β-model (Cavaliere & Fusco-Femiano, 1976) was fit to the data. Data for the fit was taken from a circular aperture with a radius of 98.4″. This aperture was split into circular annuli with 4.92″ thicknesses and fit using the Sherpa program included in the CIAO software The β-model for the surface brightness is:

$$I(r) = I_0 \left(1 + \left(\frac{r}{r_0}\right)^2\right)^{-3\beta+\frac{1}{2}}. \tag{2.3}$$

We used the observed flux within the 49.2″ radius spectral aperture to express the normalization in terms of physical units. We also determine the central electron density, n_{e0}, using the thermal-plasma emission model discussed above and assuming that the plasma is isothermal throughout the intra-cluster medium (ICM). The β-model fitting results and 90% confidence intervals are presented in Table 2.3.

Assuming that the cluster is isothermal and in hydrostatic equilibrium, we can infer the mass distribution (e.g., Neumann, 2005) of

$$M(r) = \frac{3\beta T_X}{G\mu m_p} \frac{r^3}{r^2 + r_0^2}, \tag{2.4}$$

where μ is taken at 0.59 for fully ionized hydrogen and helium of cosmic abundances. To test the validity of the isothermality assumption we fit temperatures for two portions of the spectral aperture: A circular region about the center of the emission and an annulus immediately outside the circle. The border between these sub-regions was

chosen so that the annulus and the circle each contain roughly the same number of source counts. Results are consistent with the isothermal assumption but provide no additional constraint.

We extrapolated the mass profile to obtain r_δ, the radius at which the spherically-averaged cluster density is δ times the critical density at the cluster redshift, and M_δ, the cluster mass within r_δ. We evaluate these parameters for δ =200, 500 and 2500. We detect cluster emission above background to a radius of approximately r_{500}, meaning that we see cluster emission from the majority of the area inside the aperture used for obtaining the spectral data ($r_{500} = 38.9''$ versus the spectral aperture of $49.2''$). Values for M_δ and r_δ are listed in Table 2.4. We find that though the X-ray temperature, and by extension the inferred mass, is low compared to other RCS clusters of similar richness, the measured core radius is comparable (Hicks et al., 2008). Lastly, we estimate the cluster gas mass and gas mass fraction at these three density contrasts by applying our β-model for the gas density and comparing to our mass estimates. Results from this analysis are presented in alongside the mass estimates in Table 2.4.

2.4 Relations between observables

2.4.1 Mass-temperature relation

We compare the values of M_δ calculated from the β-model to the mass-temperature relations for M_{500} and M_{2500} determined by Vikhlinin et al. (2006) in Figure 2-1. This figure also includes data from six other RCS clusters, similarly analyzed, for comparison. A full treatment of this larger sample will be included in Hicks et al. (2008). We scaled masses by $E(z) \equiv H(z)/H_0$ to account for redshift evolution expected in the self-similar model (e.g., Bryan & Norman, 1998). The M–T_X relation is then parametrized as

$$E(z)M_\delta = M_0 \left(\frac{T_X}{5 \text{ keV}}\right)^\alpha 10^{14}\ h_{70}^{-1}\mathrm{M}_\odot, \tag{2.5}$$

with M_0 and α taken directly from Vikhlinin et al. (2006): For $\delta = 500$, $M_0 = 2.93 \pm 0.16$ and $\alpha = 1.61 \pm 0.11$; for $\delta = 2500$, $M_0 = 1.28 \pm 0.05$ and $\alpha = 1.64 \pm 0.06$. RCS043938-2904.7 agrees with the relation (at 90% confidence) for both $\delta = 500$ and $\delta = 2500$.

An additional mass estimator based on X-ray data which is known to have a tight correlation with cluster mass is the integrated pressure $Y_\delta \equiv M_{g,\delta} T_X$ (Kravtsov et al., 2006; Nagai et al., 2007). We compare our cluster data to the relation obtained through simulations done by Kravtsov et al. (2006) and with the relation obtained from *Chandra* data by Nagai et al. (2007). Our data agree at the 90% confidence level with both relations.

2.4.2 Luminosity-temperature relation

We adopt the luminosity-temperature parametrization of a simple power law and redshift evolution following the self-similar evolution model

$$E(z)^{-1} L_X = L_0 \left(\frac{T_X}{6 \text{ keV}} \right)^{\alpha} 10^{44} \, h_{70}^{-2} \text{ erg s}^{-1}. \tag{2.6}$$

For the temperature dependence exponent and normalization, we take the local relation determined by Arnaud & Evrard (1999) for luminosity in the 2-10 keV band extrapolated to r_{200}. This gives $\log_{10} L_0 = 0.54 \pm 0.03$ and $\alpha = 2.88 \pm 0.15$. Maughan et al. (2006), who analyzed 11 high-z clusters observed with XMM and/or *Chandra*, find this relation to be an acceptable fit to their data as well. Their assumed redshift evolution includes an additional factor to account for evolution of the density contrast needed for virialization, but they note that it is dominated by the self-similar evolution factor. Given the size of the errors in our measurements, we neglect this smaller term. We compare our extrapolated luminosity in the 2-10 keV band with the relation in Figure 2-2, which shows that the present data are consistent with the local relation. Six other RCS clusters, whose complete treatment will be presented in Hicks et al. (2008), are included in the figure for comparison.

2.4.3 Mass-richness relation

Optical richness can be quantified using the B_{gc} parameter introduced by Longair & Seldner (1979), which has been shown to correlate well with cluster velocity dispersion, as well as other observables which have been used for cluster mass proxies (Yee & Ellingson, 2003). See Yee & López-Cruz (1999) for a detailed review of richness measures. The RCS measures a modified version of this parameter, B_{gcR}, considering only the red-sequence galaxies in their richness calculation as an attempt to better estimate the cluster mass (Gladders & Yee, 2005). The mass-richness relation is parametrized as

$$M_{200} = 10^{A} B_{gcR}^{\alpha} (1+z)^{\gamma}\ 10^{14}\ \mathrm{M}_{\odot}, \tag{2.7}$$

as in Gladders et al. (2007). The measured B_{gcR} value for RCS043938-2904.7 of 1591±494 $(h_{50}^{-1}\ \mathrm{Mpc})^{1.77}$ (also listed in Table 2.3) was derived from the RCS data using the method described in Gladders & Yee (2005). We use the relation obtained by Blindert et al. (2008, in preparation) from a dynamical study of 33 low- to moderate-redshift (z <0.6) RCS clusters. They found values of $A = -5.7 \pm 3.4$ and $\alpha = 2.1 \pm 1.2$ (68% confidence) and a ±0.46 dex scatter in mass at a constant richness. This is consistent with the values measured by Yee & Ellingson (2003) for the X-ray selected CNOC1 sample, over a similar redshift range. The Blindert sample was limited in redshift and places no constraint on redshift evolution, so we take $\gamma \equiv 0$. This is also consistent with the values and evolution inferred from the cosmological study of Gladders et al. (2007). In Figure 2-3 we compare our cluster to the Blindert relation. Assuming that the spherically symmetric β-model is a good representation of the system, RCS043938-2904.7 is a significant outlier, with far too large a richness mass for its X-ray mass. Optical spectroscopy measurements of RCS043938-2904.7 show evidence of significant substructure, as will be described in the next section.

2.5 Optical spectroscopy

Optical spectra have been obtained for galaxies in RCS043938-2904.7 (Gilbank et al., 2007; Barrientos et al., 2004). The details of the observations are given in these papers. Briefly, the datasets comprise 34 spectroscopically confirmed members of the RCS043938-2904.7 system, with redshifts from LDSS-2 and IMACS on the 6.5-m Magellan Baade telescope and FORS2 on the VLT. The spectra of Gilbank et al. (2007) were classified on a scale of 1-5 in terms of redshift quality. For this discussion we take classes 1-3 to be secure redshifts and class 4 to be lower confidence redshifts. Redshift measurements were not possible for class 5 spectra. The VLT spectra of Barrientos et al. (2004) have been reclassified onto the same system. To this sample we add recent spectroscopy from FORS2 on the VLT, similar to those described in Barrientos et al. (2004). These data will be presented in Barrientos et al., in preparation.

As discussed in Gilbank et al. (2007), RCS043938-2904.7 displays a clear double peak in the redshift histogram at $z \sim 0.96$. Figure 2-4 shows a redshift histogram centered on the mean redshift of the two components, $z = 0.9558$. Only galaxies within a radius of 5 arcminutes, corresponding to a projected distance of $\sim 2.0\ h_{70}^{-1}$ Mpc, are considered. Fitting a double-gaussian to the peaks yields central locations of the two peaks which are insensitive to the redshift quality class under consideration. The separation of the two peaks in the mean rest frame ranges from 3000 km s^{-1} to 3250 km s^{-1} depending on the redshift quality chosen. The difference between the two cases is comparable with the redshift uncertainty on a single measurement (~ 200 km s^{-1}, Gilbank et al., 2007).

With the new spectroscopy, there are now enough redshifts to attempt to measure approximate velocity dispersions for the two components. Using all galaxies of redshift quality 4 or better gives: $\sigma = 1080 \pm 320$km s^{-1} for the z=0.9435 component and $\sigma = 560 \pm 160$km s^{-1} for the z=0.9681 component, where the errors are based on jackknife uncertainties as in Gilbank et al. (2007). Such velocity dispersions would correspond to masses of 7.5×10^{14} M$_\odot$ and 1.0×10^{14} M$_\odot$ respectively (Carlberg et al.,

1997). However, velocity dispersion estimates based on so few points may be biased and the formal uncertainties are large enough that the values are consistent with both components having equal velocity dispersions. We note that both peaks in the velocity histogram contain approximately equal numbers of galaxies and use this, coupled with the velocity dispersion uncertainties, to adopt the conservative assumption that both systems have approximately equal masses. Refined mass estimates from dynamics will require more redshifts and such work is ongoing. Figure 2-5 shows the spatial distribution of these galaxies on the sky in a composite R, I and K band image, overlaid with X-ray contours. Contours begin 1σ, assuming Poisson statistics, above the average number of counts per pixel in the entire image (which is essentially the background), and are spaced in 0.25σ intervals. Figure 2-6 shows the same X-ray contours along with RCS galaxy overdensity contours, starting at 2σ and spaced in 0.25σ increments, as well as the positions of galaxies with measured spectroscopic redshifts, including field galaxies and galaxies from each of the two redshift peaks. The two redshift peaks overlap in position on the sky and thus it is not possible to say for certain which system is responsible for the X-ray emission measured, or whether both systems contribute, though the latter seems most likely. From Figures 2-5 and 2-6 it can be seen that the peak of the X-ray emission is nearly coincident with the brightest cluster galaxy (BCG) of the z=0.94 cluster, and that the emission is elongated in the direction of the z=0.96 cluster's BCG. This adds further support to the idea that the observed X-ray emission is likely due to a combination of emission from each of the two systems.

Figure 2-3, as noted above, shows B_{gcR} plotted against M_{200} for our RCS043938-2904.7 and a selection of other RCS clusters. RCS043938-2904.7 lies well outside the region bounded by the 1-σ scatter, appearing significantly richer than its X-ray mass would suggest. This is not surprising given that the spectroscopy discussed above suggests that RCS043938-2904.7 is an extended structure containing two comparable, less rich systems. Since these systems lie so close together in redshift that their red sequences overlap, the red-sequence B_{gcR} measurement is the sum of that of both these systems. A more reasonable estimate of the true richness associated with the

measured mass X-ray mass, in light of the double-peaked velocity distribution, would be to halve the measured B_{gcR}. Doing so brings the X-ray mass and the richness mass into agreement, within the large scatter.

2.6 Discussion

RCS043938-2904.7 has an inferred X-ray mass which is one to two orders of magnitude lower than the mass indicated by its red-sequence richness, assuming that the X-ray emission is from a single, spherical, isothermal gas distribution and that the richness is associated with a single cluster ($M_{200,X} = 4.6 \pm^{6.0}_{1.7} \times 10^{13}$ $M_\odot$ versus $M_{200,B_{gcR}} = 1.1 \times 10^{15} \pm 0.46$ dex $M_\odot$). This is a significant discrepancy for two reasons. First, as mentioned before, richness is well correlated on average with other observable properties. Secondly, clusters with masses above 10^{15} $M_\odot$ are quite rare, especially at $z \sim 1$. This means that if the richness mass estimate of RCS043938-2904.7 were truly indicative of its size, it would be among the largest overdensities in the observable universe, while also being very underluminous. Yet the X-ray properties, which suggest a much less massive object, are consistent with the expected M_δ–T_X and L_X–T_X relations, meaning that the temperature of the plasma is consistent with its observed distribution. One possible interpretation of these results is that the red-sequence galaxies used to measure the optical richness and the X-ray emitting gas trace different volumes. Specifically, while the X-ray luminous plasma is confined within one or more deep gravitational potential wells, the galaxy population may occupy a more extended region which is not yet dynamically relaxed. The existence of such a structure in RCS043938-2904.7 is supported by its two-peaked radial velocity distribution.

Merging and dynamically active clusters are expected and observed to be increasingly common at higher redshifts (e.g., Jeltema et al., 2005). Thus any cluster sample will include an increasing fraction of dynamically young systems at higher redshift. Furthermore, N-body simulations indicate that a significant fraction of cluster samples selected using broadband color discrimination will be systems whose galaxy members

are not predominantly associated with a single, large potential well, but rather are spread amongst a number of smaller, but still physically associated, dark matter halos distributed along the line-of-sight (Cohn et al., 2007). Simulations of the RCS technique on mock catalogs tuned to reproduce observables such as the observed galaxy color distribution and the two-point correlation function show that we expect false-positive cluster detections to occur at a frequency of $\sim$5% in the RCS (Gladders, 2002). This agrees with initial results based on a small number of clusters (Gilbank et al., 2007; Blindert et al., 2007).

Since the red-sequence galaxies used in the RCS richness measurements form very early ($z \gtrsim 2$) in high density regions, overdensities of red-sequence galaxies can be associated with very large structures which may not be relaxed during the observed epoch. The X-ray luminous plasma, on the other hand, will be confined to one or more gravitational potential wells whose size is limited by the collapse timescale. In the hierarchical collapse paradigm of a ΛCDM universe, the large, virialized wells seen in local clusters do not develop until long after the galaxies have formed. In this scenario, for any evolving cluster, there is likely to be an epoch at which the apparent richness overestimates the virialized mass.

Moreover, the misinterpretation of the X-ray emission from a complex, dynamically young cluster as a single, virialized structure can lead to an overestimate of the inferred gas mass fraction and an underestimate of the total mass, which can be seen as follows. Let us consider two models for the X-ray emission seen in RCS043938-2904.7. Our one-component model (Model I) is the set of assumptions used in our X-ray analysis thus far: X-ray emission is from a single, spherically-symmetric distribution of gas in hydrostatic equilibrium with a gravitational potential which is well-described by a β-model. The two-component model (Model II) assumes that there are two nominally identical (i.e. with the same values of β, r_0 and T_X), virialized gas distributions, separated along the line of sight, and that each of the two gas distributions is responsible for half of the measured X-ray flux. Each component is assumed to obey the local M_δ–T_X and L_X–T_X relation.

Because it assumes the flux is halved between the two components, the luminosity

inferred per cluster in Model II is half that of Model I. The luminosity scales as the square of the gas mass, so since the spatial distribution is the same for each cluster, the inferred gas mass and thus also the electron density will be reduced by a factor of $\sqrt{2}$ in each of the clusters relative to Model I. Since our total mass estimate for each cluster depends only on the temperature of the X-ray emitting gas and its distribution in the plane of the sky, each of the two components in Model II will have the same total mass as the single component in Model I. This means that the inferred gas mass fraction will be a factor of $\sqrt{2}$ lower using Model II versus Model I. The total mass, total gas mass and gas mass fraction results using each of the two models can be found in Table 2.4.

Similarly, n identical components along the line of sight would reduce the inferred gas mass per component and the overall gas mass fraction by a factor of $\sqrt{n}$ in addition to reducing the luminosity per component by a factor of n. In principle, luminosity measurements and the L_X–T_X relation constrain the number of components allowed, but our luminosity errors are too large to distinguish between Model I and Model II.

Mathiesen & Evrard (2001), using a suite of hydrodynamic cluster simulations, found that during merger events the ICM spectral fit temperature will underestimate the mass-weighted ICM temperature by $\sim 20\%$, because the cool, denser inflowing gas will dominate the emission over the gas already heated by the merger. This means that for a dynamically young system, such as RCS043938-2904.7, where even the most virialized components are likely to have undergone recent mergers, X-ray mass estimates for those clusters may still be below the virialized masses by several tens of percent. In a recent detailed study of the cluster Cl 0024+17, Jee et al. (2007) found a similar underestimation of the true mass distribution due to the assumption of a single virialized mass structure rather than two components extended along the line of sight and in a state of ongoing dynamic interaction.

In summary, the assumption of spherical symmetry and virial equilibrium for a cluster system containing extended line-of-sight structure and dynamic evolution can lead to overestimation of the gas mass fraction and underestimation of the total mass. The baryon mass fraction in relaxed galaxy clusters is expected to be a uni-

versal quantity (e.g., White et al., 1993; Vikhlinin et al., 2003), suggesting that the comparison of cluster gas mass fractions inferred by assuming spherical symmetry to canonical cluster values might be used to infer the presence of line-of-sight structure. As noted by White et al. (1993), the cosmological baryon mass ratio, Ω_b/Ω_m, provides an upper limit to the total gas mass fraction. This ratio from the WMAP three-year data results is $\Omega_b/\Omega_m = 0.175 \pm 0.012$ (Spergel et al., 2007).

Galaxy cluster samples at high redshift are expected to have lower cluster gas mass fractions than local samples (Hicks et al., 2008; Sadat et al., 2005; Ettori et al., 2004, e.g.,). Also, a positive correlation between temperature and gas mass fraction has been observed (e.g., Vikhlinin et al., 2006; Sanderson et al., 2003). This suggests that a high-redshift cluster with a low X-ray temperature, such as RCS043938-2904.7, ought to have a correspondingly low gas mass fraction. Instead, we observe a very high gas mass fraction assuming that it is a single, spherical matter distribution, especially measured within a large radius. At r_{500}, we find $f_{gas,500} = 0.17\pm^{0.07}_{0.08}$. We observe cluster emission to approximately this radius, so this gas mass fraction estimate is unlikely to have the extrapolation errors that the measurement at r_{200} might. Assuming that Model II is more appropriate for the physical state of RCS043938-2904.7 lowers the gas mass fraction towards what is expected.

Would this pair of clusters be physically associated? As an order-of-magnitude argument, we note that the richness mass ($\sim 1\times10^{15}$ $M_\odot$) is roughly equal to that of a sphere of radius $\sim$13 Mpc with the cosmic density of $z = 0.96$. Optical spectroscopy shows that the redshift separation of the two components in RCS043938-2904.7 is $\Delta z \approx 0.005$, or a physical separation of about 12 Mpc in the Hubble flow. This rough agreement supports the conclusion that RCS043938-2904.7 is an incompletely-virialized system which is still approaching equilibrium, and that the galaxy distribution traces unvirialized matter extended along the line-of-sight, as well as the virialized matter traced by the X-ray gas. The free-fall collapse time for the two components given by the richness mass is approximately equal to the lookback time, indicating that this cluster would be nearly virialized by about the present epoch.

Additional observations are required to determine the physical state of RCS043938-

2904.7. Due to the low number of source photons from this cluster, there are large errors in the X-ray luminosity and temperature. Improvements on both would increase the precision of the X-ray mass estimates and the gas mass fractions. An independent mass estimate, such as might be obtained from weak lensing, could also help distinguish which mass estimate (richness or X-ray) is more appropriate, as well as giving additional insight into the distribution of matter. A weak lensing measurement, though difficult, would be particularly interesting for this system if it could trace the spatial distribution of cluster mass perpendicular to the line of sight, possibly revealing more substructure. Additional spectroscopy, currently underway, will help to further constrain line-of-sight substructure.

2.7 Summary

We present new CXO observations and optical spectroscopy measurements for the high-redshift galaxy cluster RCS043938-2904.7 detected in the Red-sequence Cluster Survey. We have obtained a spectral temperature and estimated total mass, gas mass and gas mass fractions from the X-ray data. The measured X-ray properties and mass estimates agree well, within errors, to the locally derived L_X–T_X and M_δ–T_X relations for galaxy clusters, but not with the local M_{200}–B_{gcR} relation. Spectroscopy of RCS043938-2904.7 shows a two-peaked velocity distribution, suggesting substructure along the line-of-sight. Assuming that there is a single, virialized mass distribution in RCS043938-2904.7 results in gas mass fraction measurements which are higher than others in the RCS, which may also indicate line-of-sight structure. Accounting for the substructure with a two-component model for the mass distribution brings the richness mass into agreement with the X-ray mass and the gas mass fractions into agreement with expected values. Weak lensing measurements, additional X-ray observations and additional spectroscopy would be useful in further constraining both the total amount of mass in the system and its distribution.

2.8 Tables & Figures

Obsids	Observation Dates[a]	Livetime[b]	Counts[c]
3577, 4438	04/16/2003, 06/06/2003	93.3/105.0	359/2093

Table 2.1: Observation Log. a: Dates are in m/d/y format. b: Livetime is in ks, and split into good/total amounts. c: Counts are in the 0.3-7.0 keV band, and split into source/source+background totals.

Redshift	T_X [a]	$L_{0.5-2}$ [b]	L_{2-10} [b]	L_{bol} [b]	$S_{0.3-7}$ [c]
0.9558	$1.5\pm^{1.0}_{0.4}$	$4.0\pm^{3.1}_{2.7}$	$2.1\pm^{1.7}_{1.4}$	$6.9\pm^{4.0}_{3.5}$	$13.7\pm^{7.5}_{7.0}$

Table 2.2: Spectral Analysis Results. a: Temperature is in keV. b: Luminosities in 10^{43} erg s^{-1}. Subscripts refer to the rest frame energy band; the bolometric luminosity is estimated by the 0.05-50 keV band. c: Measured flux in the 0.3-7.0 keV band, in units of 10^{-15} erg cm^{-2} s^{-1}. All values are from within the 49.2″ radius spectral aperture.

I_0 [a]	n_{e0} [b]	r_0 [c]	β	B_{gcR} [d]
$3.7\pm^{2.5}_{2.0}$	3.9 ± 1.5	$14.7 \pm 1.9/117 \pm 15$	$0.56\pm^{0.06}_{0.04}$	1591 ± 464

Table 2.3: β-model Results and Optical Richness. a: Central surface brightness, in 10^{-14} erg cm^{-2} s^{-1} arcmin^{-2}. b: Central electron number density, in 10^{-3} cm^{-3}. c: β-model core radius, in arcseconds/kpc. d: Optical richness, in $(h_{50}^{-1}$ Mpc$)^{1.77}$, as measured by the RCS (Gladders & Yee, 2005).

		Model I			Model II		
δ	r_δ [a]	M_δ [b]	$M_{gas,\delta}$ [c]	$f_{gas,\delta}$ [d]	M_δ [b]	$M_{gas,\delta}$ [c]	$f_{gas,\delta}$ [d]
200	$510\pm^{160}_{70}$	$4.6\pm^{6.0}_{1.7}$	$1.05\pm^{0.47}_{0.34}$	$0.23\pm^{0.09}_{0.11}$	$9.2\pm^{12.0}_{3.4}$	$1.48\pm^{0.66}_{0.48}$	$0.16\pm^{0.07}_{0.08}$
500	$310\pm^{110}_{50}$	$2.6\pm^{3.7}_{1.0}$	$0.45\pm^{0.25}_{0.16}$	$0.17\pm^{0.07}_{0.08}$	$5.2\pm^{7.4}_{2.0}$	$0.64\pm^{0.35}_{0.23}$	$0.12\pm^{0.05}_{0.06}$
2500	$90\pm^{65}_{50}$	$0.33\pm^{1.32}_{0.30}$	$0.03\pm^{0.08}_{0.03}$	$0.09\pm^{0.03}_{0.04}$	$0.7\pm^{2.6}_{0.6}$	$0.04\pm^{0.11}_{0.04}$	$0.07\pm^{0.02}_{0.03}$

Table 2.4: Total Mass, Total Gas Mass and Gas Mass Fraction Estimates. Mass values are for a single component in Model I and for the sum of two components in Model II. a: The physical radii corresponding to each of the three density contrast radii, in h_{70}^{-1} kpc. b: Total mass for each model and density contrast, in 10^{13} h_{70}^{-1} $M_\odot$. c: Gas mass for each model and density contrast, in 10^{13} $h_{70}^{-5/2}$ $M_\odot$. d: Gas mass fractions for each model and density contrast, in units of $h_{70}^{-3/2}$.

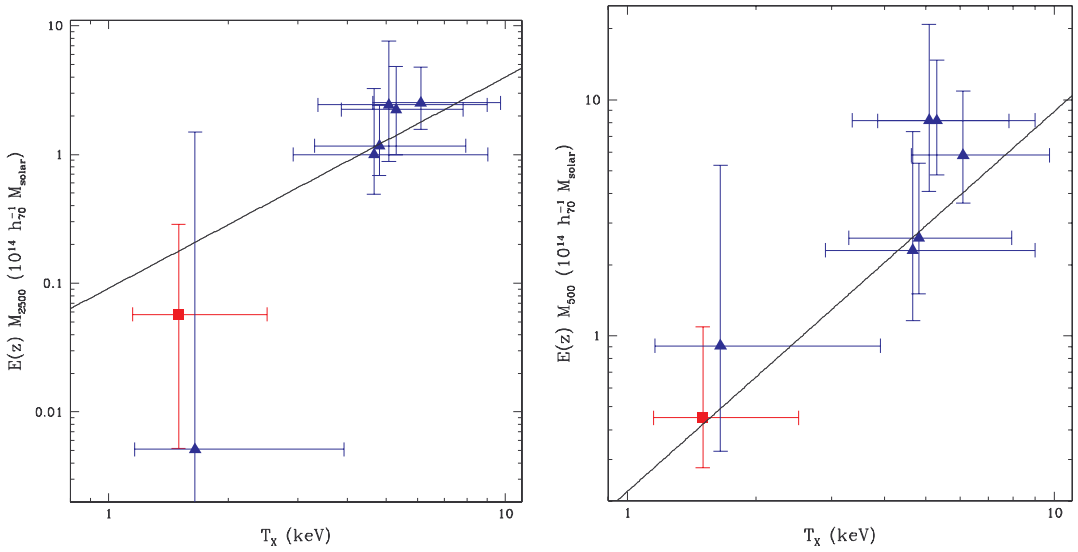

Figure 2-1: Mass-Temperature Relation for M_{2500} (at left) and M_{500} (at right). The solid lines are the relation obtained by Vikhlinin et al. (2006). The red square point on each plot indicates RCS043938-2904.7. The blue triangle points indicate a selection of other RCS clusters which were similarly analyzed and are provided only for comparison. A detailed analysis of the set of RCS clusters and their redshift evolution is beyond the scope of this paper and will be provided in Hicks et al. (2008).

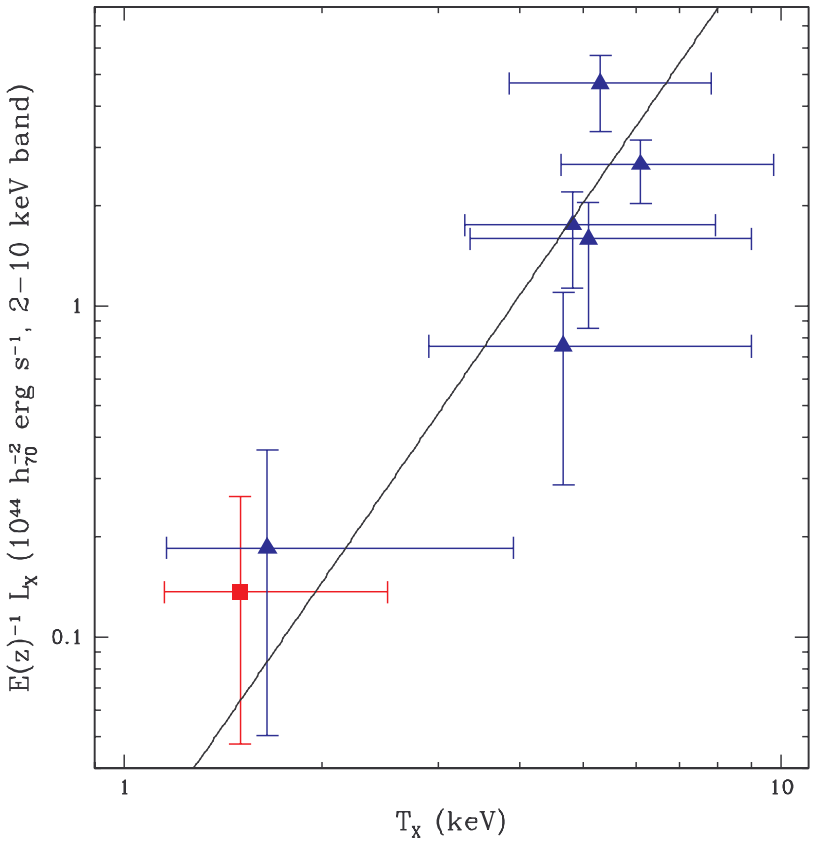

Figure 2-2: Luminosity-Temperature Relation. Luminosity is in the 2-10 keV band, extrapolated to the radius r_{200}. Redshift evolution is scaled out according to the self-similar model. The red square point indicates RCS043938-2904.7. The blue triangle points indicate a selection of other RCS clusters which were similarly analyzed and are provided only for comparison. A detailed analysis of the set of RCS clusters and their redshift evolution is beyond the scope of this paper and will be provided in Hicks et al. (2008).

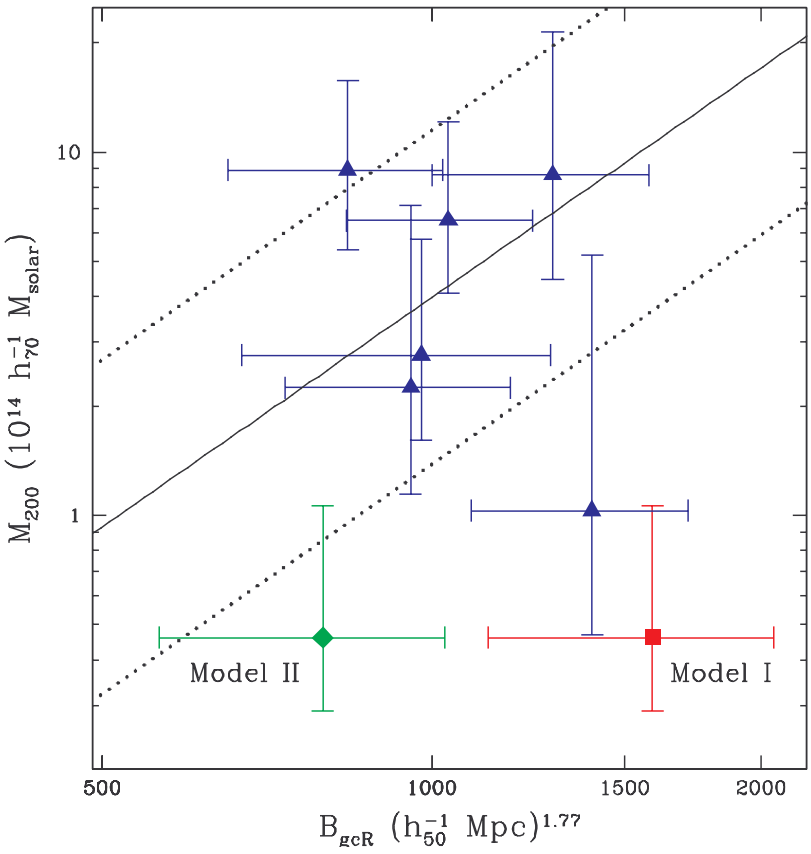

Figure 2-3: The M_{200}–B_{gcR} relation, plotting X-ray mass against richness. The solid line is the Blindert et al. relation and the dotted lines above and below are the 1σ scatter (± 0.46 dex). The red square point indicates RCS043938-2904.7 assuming that all the richness is associated with a single component (Model I). The green diamond point indicates each of the two equal-mass components within RCS043938-2904.7 assuming Model II, with half the observed richness associated with each component. The blue triangle points indicate a selection of other RCS clusters which were similarly analyzed and are provided only for comparison. A detailed analysis of the set of RCS clusters and their redshift evolution is beyond the scope of this paper and will be provided in Hicks et al. (2008).

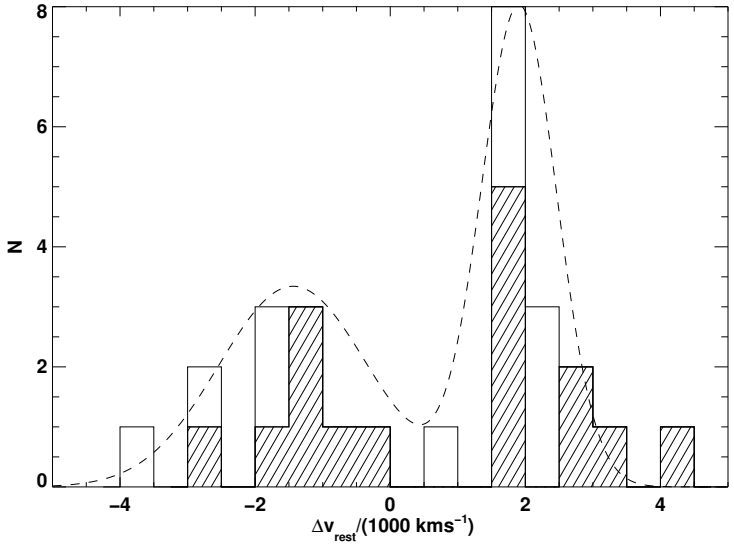

Figure 2-4: Rest-frame velocity histogram centered around the mean velocity of the RCS043938-2904.7, z=0.9558. Hatched histogram shows secure redshifts and open histogram shows lower confidence measurements. The overplotted curves show best double-gaussian fits to these, solid and dashed curves respectively. Uncertainties are sufficiently large that velocity dispersion measurements for each of the two components are consistent with equal velocity dispersions.

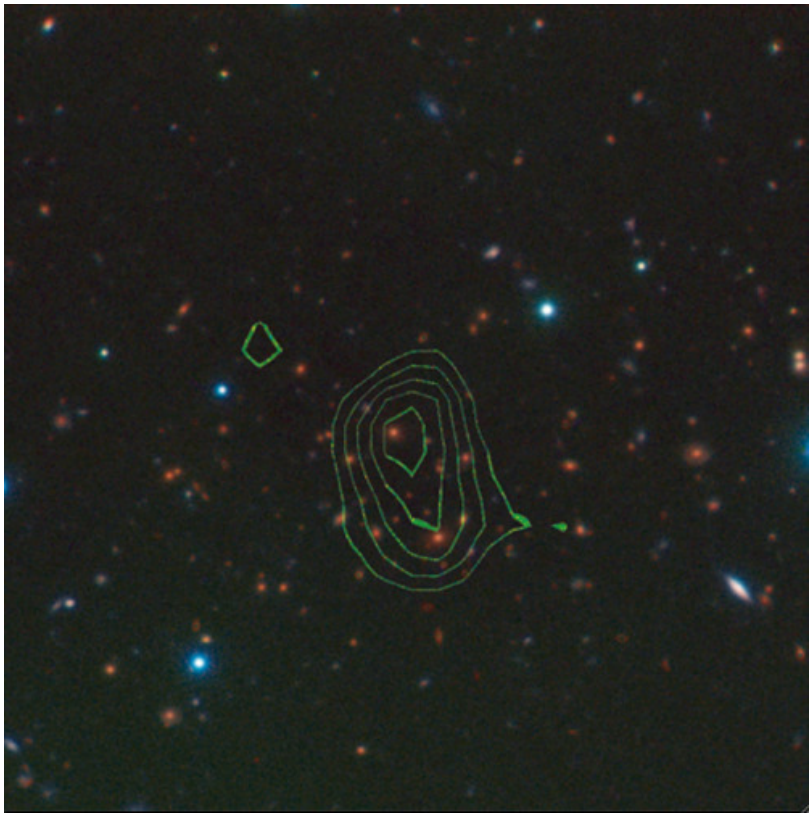

Figure 2-5: Three-color image (Red, green and blue are K, I and R bands, respectively) of RCS043938-2904.7 with overlaid green X-ray contours. North is up and east is to the left, and the image is $2'$ (797 kpc) on a side. The X-ray image was smoothed using a $0.75''$ gaussian kernel and X-ray point sources were removed using the CIAO script `dmfilth`. Contours begin 1σ above the mean counts per pixel (assuming Poisson statistics) and contours are separated by a 0.25σ spacing.

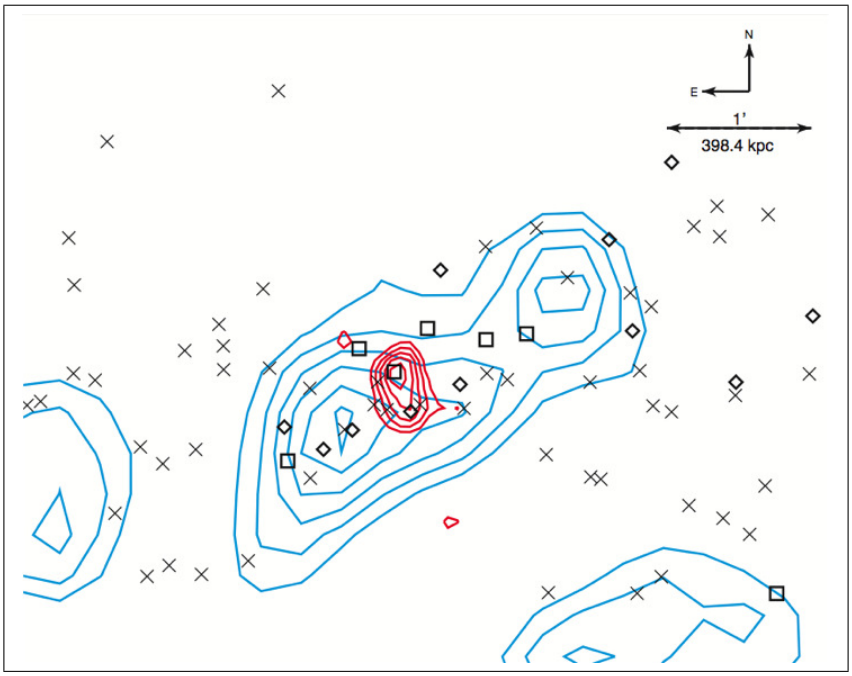

Figure 2-6: In red, X-ray contours as in Figure 2-5 and in blue RCS galaxy overdensity contours, starting at 2σ and increasing in 0.25σ increments. Points indicate galaxies with measured redshifts from optical spectroscopy. X points indicate galaxies with which are not within a ± 5000 km s^{-1} window of the mean cluster redshift, box points indicate galaxies associated with the z=0.94 cluster, and diamond points indicate galaxies associated with the z=0.96 cluster.

Chapter 3

The Analytic Image Model Method for Measuring Flexion

3.1 Measuring Flexion

Techniques for measuring the gravitational lensing fields and inferring the lens mass distribution are well established for both strong lensing and weak lensing (e.g., Kaiser et al., 1995; Coe et al., 2008, and others). In recent years, several approaches have been developed for measuring flexion fields from galaxy images. In this chapter I will describe each briefly, and then extensively describe the Analytic Image Model (AIM) method which this thesis focusses on.

3.1.1 Shapelets

Goldberg & Natarajan (2002) introduced a method of improved shear estimation based on measurements of the octupole moments of the lensed galaxy surface brightness distribution in addition to the usual quadrupole moment measurements. Similar work was done independently by Irwin & Shmakova (Irwin & Shmakova, 2005, 2006). Goldberg & Bacon (2005) refined the mathematics of this method and applied the shapelets image decomposition (Refregier, 2003; Refregier & Bacon, 2003). The shapelets method decomposes each data image over a set of basis images, and

characterizes the lensing transformation as a linear operation on this set of basis functions. The basis functions are the Gauss-Hermite polynomials which describe the two-dimensional quantum simple harmonic oscillator (QSHO) wavefunctions, and the linear operation is cast in the well-described mathematical raising and lowering operators of the QSHO. Since the Hermite polynomials are a complete, orthonormal basis, any image can be decomposed into shapelets.

However, as noted in Leonard et al. (2007), shapelet decomposition can be computationally slow for large images and the appropriate maximum number of required shapelets coefficients is not well defined *a priori* and must be determined empirically. This is because, although shapelets provide a complete set of basis functions, the shapelets are not the most natural basis functions. Massey et al. (2007) improve on the Cartesian shapelets by introducing a polar shapelets approach to shear and flexion estimation which more naturally describes the surface brightness profile of observed galaxies, though in the case of steep or highly elliptical unlensed galaxy profiles these basis functions do not accurately reproduce the shear field and underestimate it by as much as 20% (Melchior et al., 2010). In the regime where flexion is a significant effect, the shear magnitude is a non-trivial fraction of unity, meaning that lensed objects have high observed elllipticity, and steep, Sérsic-type galaxy profiles are commonly observed. This raises significant questions about the validity of using a shapelet decomposition for the more highly-lensed objects where flexion is non-negligible.

Additionally, to describe gravitational lensing as a linear operation on the basis functions, the surface brightness distribution is expanded in a Taylor series, which adds another approximation to the modeling of the light distribution on top of the quadratic lens equation approximation. The inversion of this linear operation requires the assumption that some shapelet coefficients are zero, either individually or as an average over an ensemble of galaxies. While this assumption is often justified, there are systematic effects such as the intrinsic co-alignment of galaxies due to large scale structure which must be considered.

3.1.2 Higher Order Lensing Image Characteristics (HOLICs)

It is also possible to characterize the lensing transformation by observing its effect on moments of the surface brightness profile. As discussed in Chaper 1, gravitational lensing is a coordinate transformation between the source plane and the image plane. Moments of the observed surface brightness profile can be measured, and under some assumptions on the moments in the source plane an inversion can be made to determine the lensing fields. In many weak-lensing shear measurements this is done using quadrupole moments to measure the observed ellipticity and relate that to the shear. These moments are usually calculated using a window function to reduce noise from high radius but low signal pixels. Irwin & Shmakova (2006) produced an early approach to measuring what they referred to as "sextupole lensing", which is now called flexion. Okura et al. (2007, 2008) adapted the mathematics of the moment approach, or, as they call it, Higher-Order Lensing Image Characteristics (HOLICs), to be in terms of the flexion fields defined by Goldberg & Bacon (2005). Assuming that the intrinsic odd moments of the unlensed images are randomly distributed about zero, third-order or higher moments of the lensed image can be inverted to yield estimates of the flexion fields.

The work by Okura et al. does not fully take into account the mass sheet degeneracy and in many places assumed that the shear was small. This is not a good assumption for most regions where flexion is measurable, as noted by Schneider & Er (2008) who modify the HOLICs approach to be fully mass-sheet invariant and describe the moments and the lensing fields in a consistent mathematical framework using complex variables instead of indexed tensors.

It is useful to note that the shapelets approach and the HOLICs approach share the assumption of a zero value (or zero mean value) for the odd-order moments and shapelet coefficients of the unlensed images. Fundamentally, the shapelets method is a specialized version of the HOLICs method. The HOLICs approach assumes a quadratic local lensing transformation and inverts windowed moments to yield shear and flexion measurements. The shapelets method combines the window function and

moment orders into the specific combinations which correspond to the QSHO wavefunctions and use a linearized approximation to the surface brightness distribution to invert the lensing transformation and measure the shear and flexion.

3.1.3 AIM

In the rest of this chapter I describe a new alternative to the shapelets and HOLICs methods: the Analytic Image Model (AIM) method. This method is a local lensing measurement, meaning that unlike strong lensing methods it considers each galaxy image individually, rather than associating multiple images with a single source. It is a parametrized analytic approach to measuring the lensing transformation which is fully invariant to the mass sheet degeneracy. The AIM method assumes a generic analytic model for the unlensed surface brightness profile and a quadratic lensing transformation. By optimizing a figure of merit, best fit parameters are found and the flexion can be measured.

3.2 The Analytic Image Model

3.2.1 General Method

As described in Chapter 1, Liouville's theorem implies that the gravitational lensing transformation conserves surface brightness. Therefore, the observed surface brightness $I_{\rm obs}$ at field position θ is

$$I_{\rm obs}(\theta) = I_{\rm src}(\beta(\theta)), \tag{3.1}$$

where $I_{\rm src}(\beta)$ is the unlensed surface brightness profile and $\beta(\theta)$ is the lensing coordinate transformation. The AIM method imposes an analytic model on both the lensing transformation and the unlensed surface brightness profile, and by fitting the analytic model to a data image yields an accurate estimate of the flexion fields at the location of each lensed galaxy image. Therefore I assume that there is a vector

of lensing parameters $\vec{p}_L$ and a vector of intrinsic source image parameters $\vec{p}_S$. The observed surface brightness profile can be modelled as

$$I_{\rm model}\left(\theta, \vec{p}_S, \vec{p}_L\right) = I_{\rm src}\left(\beta\left(\theta, \vec{p}_L\right), \vec{p}_S\right) \tag{3.2}$$

With a parametrized source surface brightness model and lens model, I solve for optimal model parameters by minimizing a figure of merit integrated over the image (with pixels indexed by n)

$$\chi^2 = \sum_n \frac{\left(I_{\rm data}\left(\theta^{(n)}\right) - I_{\rm model}\left(\theta^{(n)}, \vec{p}_S, \vec{p}_L\right)\right)^2}{\sigma_n^2}. \tag{3.3}$$

over a reasonable range of lens and source profile parameters. σ_n is an estimate of the error in the image surface brightness, which can be different at each pixel location $\theta^{(n)}$. If the data image in question is background limited, the noise in each pixel will be well-approximated as Gaussian.

3.2.2 Model Parametrization

In principle, ny parametrized surface brightness profile can be used for the source image. I choose an elliptical Gaussian profile, characterized by six parameters. A more complicated analytic profile (e.g. a Sérsic profile) could be substituted, though additional parameters creates the possibility of complicated parameter degeneracies.

I define the elliptical Gaussian as

$$I(\beta) = \frac{S_0}{2\pi\alpha^2} \exp\left[-\frac{(1+EE^*)\beta\beta^* - (\beta^2 E^* + (\beta^*)^2 E)}{2\alpha^2}\right]. \tag{3.4}$$

In terms of the semi-major and -minor axes, a and b, and the position angle ξ of the semi-major axis of the 1σ ellipse:

$$\begin{aligned} \alpha &= \sqrt{ab}, \\ E &= \frac{a-b}{a+b} e^{i2\xi}. \end{aligned} \tag{3.5}$$

I will refer to the real and the imaginary parts of the ellipticity as E_+ and $E_\times$ because of the directions of the elongation induced in the 1σ ellipse by each: E_+ elongates along one of the principle coordinate axes (the β_1 axis if $E_+ > 0$, else the β_2 axis), while $E_\times$ elongates along an axis rotated by 45° from either the β_1 or β_2 axis (along the line $\beta_2 = \beta_1$ if $E_\times > 0$, else along $\beta_2 = -\beta_1$). The motivation for selecting this particular definition of ellipticity is that it matches the effect of shear. Neglecting flexion for the moment, consider the exponential argument in Equation 3.4. Defining

$$E' = \begin{cases} \dfrac{E+g}{1+Eg^*} & |g| \leq 1 \\ \\ \dfrac{1+E^*g}{E^*+g^*} & |g| > 1 \end{cases} \tag{3.6}$$

and

$$\alpha' = \begin{cases} \dfrac{\alpha}{|1+Eg^*|} & |g| \leq 1 \\ \dfrac{\alpha}{|E+g|} & |g| > 1 \end{cases} \tag{3.7}$$

this argument can be written as

$$\frac{(1+EE^*)\beta\beta^* - (\beta^2 E^* + (\beta^*)^2 E)}{2\alpha^2} = \frac{(1+E'E'^*)\theta\theta^* - (\theta^2 E'^* + (\theta^*)^2 E')}{2\alpha'^2}, \tag{3.8}$$

where the image size has been rescaled and the new complex ellipticity has replaced both the shear and the true ellipticity exactly. This substitution highlights a fundamental degeneracy between shear and ellipticity (which will be discussed further in Chapter 4) and indicates that the effect of shear is to produce an image with ellipse properties E' and α' from one with E and α.

This ellipticity parametrization also puts $E = 0$, or circular images, in the center of the ellipticity parameter space with maximally elongated images at the extrema, rather than both minimal and maximal elongations at extrema, which allows the fitting algorithm to explore the region near circularity without encountering branch cuts, such as selection of a "major" axis. I choose the geometric mean of the 1σ semi-axis lengths to set the scale of the ellipse for two main reasons. The first is that α as

defined is agnostic to which axis is the major axis, consistent with not requiring branch cuts. This is particularly important for crossing through zero ellipticity, where the distinction between the major and minor axes vanishes. Secondly, α is, in a sense, an "integrated" quantity. The area of the 1σ ellipse is $\pi\alpha^2$, and therefore α is constrained by a large fraction of the image and individual pixels are less likely to dominate in the estimation of the parameter.

I parametrize the peak brightness of the image by the logarithm of the total integrated flux of the unlensed Gaussian, $\log S_0$ in Equation 3.4. Like α, this is an integrated quantity and is well constrained by the whole image, rather than being dominated by a few pixels at the center. I choose the logarithm of S_0 as a parameter rather than the linear flux to allow for a larger dynamic range during fitting.

The remaining parameters required to fully define the elliptical Gaussian are the center position coordinates of the Gaussian in either the source plane or the image plane. Rather than defining a center position β_c in the source plane, I define θ_c, the center of the image in the observed image plane. Because the transformation between the source and image coordinates is uniquely defined, these two are entirely interchangeable, and I choose the image plane center because it allows the fitting to converge more robustly. Instead of fitting for the center position of the unlensed image, I fit for the position in the image plane which maps to the center of the unlensed image.

The lensing transformation is described by six parameters, defining the three complex reduced lensing fields $g = g_1 + ig_2$, $\Psi_1 = \Psi_{12} + i\Psi_{12}$, and $\Psi_3 = \Psi_{32} + i\Psi_{32}$. These fields define $\beta(\theta)$ using equation 1.18.

3.2.3 Additional Model Elements

For each galaxy image, in addition to the analytic profile described above, I assume as given an estimate of the noise in each pixel, the background surface brightness, and the point-spread function (PSF). The noise image can be a constant (as for background-dominated noise), be proportional to the square-root of the model image (as with Poisson statistics), or some other, externally defined error specific to the

dataset being used. I assume that both the background and the PSF are constant over the individual galaxy image. For a background surface brightness I_B and a PSF $P(\theta)$, the final model image is then given by

$$\begin{aligned}\beta(\theta) = (\theta - \theta_c) - g(\theta^* - \theta_c^*) \\ - \Psi_1^*(\theta - \theta_c)^2 - 2\Psi_1(\theta - \theta_c)(\theta^* - \theta_c^*) - \Psi_3(\theta^* - \theta_c^*)^2,\end{aligned} \tag{3.9}$$

$$I(\beta) = \frac{S_0}{2\pi\alpha^2} \exp\left[-\frac{(1 + EE^*)\beta\beta^* - (\beta^2 E^* + (\beta^*)^2 E)}{2\alpha^2}\right], \tag{3.10}$$

and

$$I_{\rm model}(\theta) = \int d^2\theta' \; P(\theta - \theta') I(\beta(\theta')) + I_B. \tag{3.11}$$

This image, $I_{\rm model}$, is compared to the data image using Equation 3.3. By minimizing χ^2 over the twelve free parameters ($\log S_0$, θ_{c1}, θ_{c2}, α, E_+, $E_\times$, g_1, g_2, Ψ_{11}, Ψ_{12}, Ψ_{31}, Ψ_{32}) I find the best fit lensing parameters while accounting for the unknown intrinsic shape of the source image.

3.3 Implementation of the AIM Method

The software implementing this method has been written in the Interactive Data Language (IDL) and is compatible with version 7.1[1]. Though I have written the majority of the code, there are some functions and procedures from the NASA IDL Astronomy User's Library[2]. Additionally, minimization of χ^2 is performed using the `MPFIT` function, which is a robust IDL implementation of the Levenberg-Marquardt non-linear least-squares minimization algorithm (Markwardt, 2009). In this section I will outline the functions written for the AIM implementation of single-image fitting. Where I indicate pixel-referencing conventions in these functions, it is important to recall that IDL is "zero-indexed", meaning that the first pixel in an array is labelled by 0. In some places I use pixel indices as coordinates, so this detail could lead to pixel offsets if not considered.

[1]IDL is produced by ITT Visual Information Solutions: http://www.ittvis.com
[2]The NASA IDL Astronomy User's Library is available at: http://idlastro.gsfc.nasa.gov

3.3.1 AIM_MK_IMAGE

This function creates an image model to compare with the data image. The required inputs are the model parameters (as a 12-element array), the background surface brightness (in flux per square pixel units), a PSF image (normalized to have unit integral), and a window image. The window image defines the size of the output model image (and therefore should be the same size as the data image), and it defines the set of pixels which are to be used to calculate χ^2. This window image can be used to mask out bad pixels, impose a particular aperture, or to variably weight pixels. The model parameters are indexed from 0 to 11, ordered $\log S_0$, θ_{c1}, θ_{c2}, α, E_+, $E_\times$, g_1, g_2, Ψ_{11}, Ψ_{12}, Ψ_{31}, Ψ_{32}.

For a window of dimensions $L_1 \times L_2$ pixels, the model image is created using the analytic form described above in an array of dimensions $(L_1+D)\times(L_2+D)$, where D is the largest dimension of the PSF. The extra border is to prevent edged effects due to the PSF convolution, since the pixels along the edge of the image are convolved with pixels off the edge for a finite PSF width. After convolution, the central $L_1 \times L_2$ section of the image is excised, multiplied by the window function and returned.

There is one important convention with regards to the data image: the image center position (θ_c) is defined as an offset from the center of the image, meaning that a model without lensing and $\theta_c = 0$ will return an elliptical Gaussian centered at pixel position $[(L_1-1)/2, (L_2-1)/2]$.

AIM_MK_IMAGE also allows for additional intrinsic image models to be substituted for the standard elliptical Gaussian. For the definition of

$$r^2 = \frac{(1+EE^*)\beta\beta^* - (\beta^2 E^* + (\beta^*)^2 E)}{\alpha^2} \tag{3.12}$$

the profiles which are currently implemented include the Sérsic profile:

$$I(r) \propto \exp(-r^n/2), \tag{3.13}$$

with the additional model parameter n; a Moffat profile:

$$I(r) \propto (1 + r^2)^{-b}, \tag{3.14}$$

with the additional model parameter b; and a pseudo-Gaussian profile:

$$I(r) \propto (1 + x + k_1 x^2/2 + k_2 x^3/6 + x^4/24)^{-1}, \tag{3.15}$$

with $x = r^2/2$ and additional model parameters k_1 and k_2. These more general models have more degrees of freedom and therefore caution must be used if fitting with them in addition to fitting for lensing parameters. Note that this version of the Sérsic profile defines the index n as the inverse of the canonical Sérsic index. This is done to make the fitting convergence more straightforward, as a linear parameter exponent is better behaved than the inverse, and less likely to make the numerical derivatives which go into the curvature matrix in `MPFIT` singular.

3.3.2 `AIM_START_PARS`

This function returns a set of parameters as an initial guess of the shape of the elliptical Gaussian based on the data image. It takes as required inputs the data image, the background surface brightness, and a window image. As additional, optional input the function also takes a background-subtracted threshold below which pixels will be ignored for the purposes of determining parameters, and a limit on the maximum magnitude of the initial ellipticity that will be returned. By default, the pixel threshold is set to zero (meaning all pixels which are above the background are considered), and the full range of $0 \leq |E| < 1$ is available.

To determine initial parameters, the background level is subtracted from the data image and all pixels below the threshold are set to zero. The center position θ_c is set to the image centroid, and the size and ellipticity are derived from centroid-subtracted

second order moments:

$$M_{jk} = \frac{\sum_n I_n(\theta_j - \theta_{cj})(\theta_k - \theta_{ck})}{\sum_n I_n}, \tag{3.16}$$

$$\alpha = \left(M_{11}M_{22} - M_{12}^2\right)^{1/4}, \tag{3.17}$$

$$E = \frac{(M_{11} - M_{22}) + 2iM_{12}}{M_{11} + M_{22} + 2\sqrt{M_{11}M_{22} - M_{12}^2}}. \tag{3.18}$$

Here n indexes the pixels above the threshold. The initial estimate of $\log S_0$ is set by the sum of the thresholded pixels

$$\log S_0 = \log\left(\sum_n I_n\right), \tag{3.19}$$

though this is usually an underestimate of the true flux. This function always returns the lensing parameters as zero.

3.3.3 AIM_IMAGE_DEVIATE

This function is where the AIM code interfaces with MPFIT, which calls AIM_IMAGE_DEVIATE repeatedly during the fitting process. In order to deal with the large range in typical values for the model parameters, I rescale each parameter by the allowed parameter range so that AIM_IMAGE_DEVIATE takes in a 12-element array of parameters between -1 and 1. This allows the MPFIT algorithm to compare derivatives of χ^2 with respect to α, which has a typical scale of one to a few arcsec, with derivatives with respect to Ψ_{jk}, which has a typical scale of $\lesssim 0.1$ arcsec^{-1}. Depending on the pixel scale, this can lead to many orders of magnitude between the parameter values in the pixel-based units that this AIM implementation uses. The difference will scale by the square of the pixel scale.

AIM_IMAGE_DEVIATE takes in the scaled parameters, the parameter centers and ranges, the data, window, and PSF images, and the background surface brightness as required parameters. By default, the function will assume that the error in χ^2 (see Equation 3.3) $\sigma_n = \sqrt{I_{\rm model}\left(\theta^{(n)}\right)}$. This error estimate can be scaled by an arbitrary

factor, or overridden by a user-defined error estimate (either as a single value, or as a noise image).

The function returns a linear array of values Δ_n, where

$$\Delta_n = \frac{I_{\rm data}\left(\theta^{(n)}\right) - I_{\rm model}\left(\theta^{(n)}, \vec{p}\,\right)}{\sigma_n}. \tag{3.20}$$

Here I have combined the intrinsic shape parameters and the lensing parameters into one vector (as they are in the code), and n indexes all pixels for which the window image is non-zero. The values $I_{\rm model}\left(\theta^{(n)}, \vec{p}\,\right)$ are obtained by calling `AIM_MK_IMAGE`. Δ_n is what is required by `MPFIT`. Note that $\sum \Delta_n^2 = \chi^2$,and as an additional option `AIM_IMAGE_DEVIATE` can return χ^2 instead of Δ_n.

3.3.4 AIM_FIT_IMAGE

This function combines `AIM_IMAGE_DEVIATE` and `MPFIT` and returns a set of fit model parameters. It takes as required input the data, window, and PSF images, and the background surface brightness. Additional optional input parameters include a noise level scaling, or an error estimate (either a single value or a full noise image), a subset of parameters to fix and corresponding values to fix them at (all parameters are free by default), and the maximum number of iterations allowed for the fitting.

`AIM_FIT_IMAGE` returns a the parameters of the best fit, including the values of any fixed parameters. Other, secondary output which can be caught in variables are the χ^2 value of the best fit, the number of degrees of freedom of the fit, the covariance matrix of the χ^2 function at the best fit parameters, error estimates for each parameter (from the diagonal elements of the covariance matrix), a "failure flag" for fits that exceed the maximum number of iterations and/or have singularities, and a "pegged flag" for parameters which become locked at the maximum or minimum parameter range. These flags are zero if no fit parameters peg or fail, and are valued at

$$\texttt{FLAG} = \sum_p 2^p \tag{3.21}$$

where p ranges over the IDL indices of the failed or pegged parameters. `AIM_FIT_IMAGE` assumes an elliptical Gaussian model for the fitting ansatz, but any of the other models implemented for `AIM_MK_IMAGE` can be used instead if desired. There will be 12 fit parameters (+1 for the Sérsic and Moffat profiles and +2 for the pseudo-Gaussian) that `MPFIT` will minimize over, and reasonable default parameter ranges for all implemented image profiles are included.

This function sets the parameter ranges, calls `AIM_START_PARS` to retrieve initial parameters, scales each of the parameters to the $(-1, 1)$ range, and calls `MPFIT` with `AIM_IMAGE_DEVIATE`. `MPFIT` returns the (scaled) best fit parameters, parameter errors, and covariances, the χ^2 value and the number of degrees of freedom. The `MPFIT` output is then rescaled to the original parameter ranges, and the pegged/failed parameters are identified and the flags are computed as described above, then the fit parameters are returned.

As an example, Figure 3-1 shows an example of a simulated arced data image (constructed using `AIM_MK_IMAGE`) and the model image fit to it using `AIM_FIT_IMAGE`. Chapter 4 delves more deeply into quantitative testing of the AIM method.

3.4 Discussion

The AIM lensing profile is a well defined analytic image model which accounts for the mass-sheet degeneracy with only one major assumption on the unlensed surface brightness profile: that it can be well-modeled as an elliptical Gaussian. The validity of this approximation when the lensed image is non-Gaussian is an issue that will be discussed in Chapter 4, but I proceed with this justification: The major reason that Gaussian surface brightness profiles are disfavored in modeling galaxy images is that they do not adequately and simultaneously match the galaxy cores and the slope of the extended light distributions. However, such a match is not the goal of the AIM method. Rather, I use a Gaussian profile to model the lens-distorted shape of the intrinsic galaxy isophotes, which are assumed to be elliptical prior to the lensing. With this in mind, it is a much more plausible approach than it might initially seem.

The best fit model is the one which best matches the shape of the lensed image isophotes, and it is this shape that contains the lensing information.

Though I have implemented the AIM method with several specific choices (an elliptical Gaussian source, a constant background, etc.), many of these choices are flexible in principle. However, it is important to be cautious of parameter degeneracies. Overwhelming the data with too many degrees of freedom, even if there are formally enough pixels for a χ^2 minimum to be well defined, leads to unreliable convergence and/or erroneous fit results. I attempted to use some of the other source profiles in fitting, hence their implementation here, but the fitting procedure was no longer robust. Fits failed to converge 20-30% of the time during testing, so until there is a better understanding of the type of profile required to converge successfully and robustly, the elliptical Gaussian will remain the primary choice.

3.5 Figures

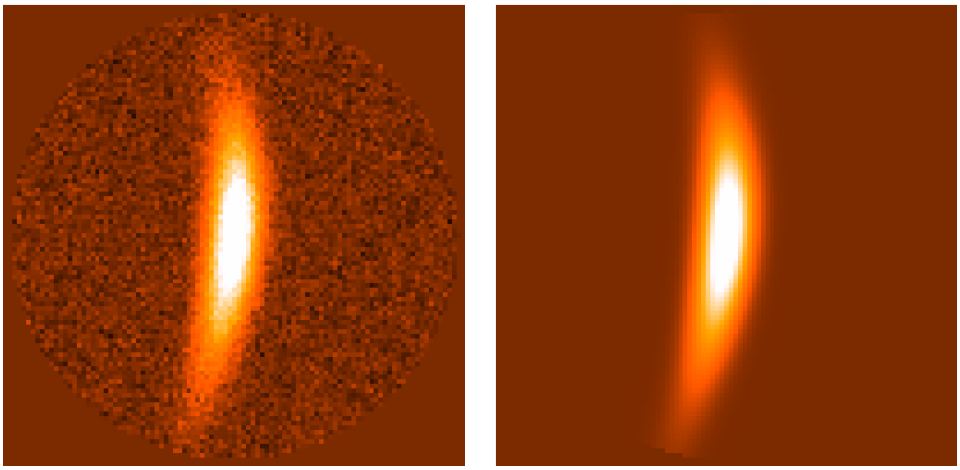

Figure 3-1: Example of data and fit images. Left: A high signal data image. Right: The AIM fit to that data image.

Chapter 4

Testing the AIM Method

4.1 Introduction

This chapter describes the methodology for and results of testing the AIM method described in Chapter 3. In general, models with a large number of parameters will not converge to accurate solutions if there are parameter degeneracies which have not been constrained. By generating simulated data images with well-defined input properties and fitting for the known lensing fields, I test the robustness of the fitting algorithm and the AIM assumptions. Reliable retrieval of known lensing field values from simulated data is a prerequisite for application to observational data.

In creating simulated data images, the properties of these images are motivated by the Hubble Space Telescope Advanced Camera for Surveys Wide Field Camera (HST ACS WFC) data set described in Chapter 5. I use a pixel scale equivalent to the HST ACS pixel scale, $0\farcs05$/pixel. The scale of data images is set by the typical scale of lensed galaxy images, meaning scales of tens of pixels. The background level, PSF size, and noise properties of the images are also selected to echo the values determined in Chapter 5.

I create six sets of 1000 images and find the best fit parameters using AIM. The intrinsic parameters are selected similarly in each dataset, as described below in §4.2. The lensing parameter selection is slightly more complicated. For datasets where the parameters are selected randomly from a given range, the image is generated using

the AIM, and the dataset will test how robustly the AIM technique fits to itself. However, if an analytic lens model is used for determining the true lensing parameters, then the lensing transformation can be exactly determined using Equation 1.11. This creates an image which is analytically lensed without approximations. In this case, the "true" lensing parameters are the shear and flexion fields which correspond to the AIM approximation of the lensing transformation at that point. Four of the datasets have lensing parameters selected from a range, and the other eight use a Singular Isothermal Sphere (SIS) lens model and are lensed without approximation. All datasets use a PSF with full-width at half maximum (FWHM) of 1.8 pixels and no background surface brightness (akin to a real dataset that has been accurately background-subtracted). Noise is added to each image pixel from a normal distribution, with $\sigma_{\rm IMG} = 1.3 \times 10^{-3}$ (arbitrary units). The noise level is chosen to be a realistic match to the HST ACS background surface brightness noise (in e^-/s) described in Chapter 5, as are the intrinsic galaxy shape parameters. Finally, two of the datasets (5 and 6) use an intrinsic Sérsic image profile, rather than a Gaussian, though the AIM profile used in fitting remains a Gaussian. The Sérsic profile is defined in Equation 3.13, and the specific property combinations for each dataset are listed in Table 4.1.

4.1.1 The Shear-Ellipticity Degeneracy

As indicated in Section 3.2.2, my choice of ellipticity parametrization is equivalent and interchangeable with the shear, meaning that in the absence of constrained flexion these two complex fields are completely degenerate. This is a well understood fact of the lensing transformation, and it is the basis of the shear measurements made using standard weak lensing techniques. Locally averaged galaxy ellipticities can be used to estimate the reduced shear and measure the mass distribution, as in the KSB weak lensing method (Kaiser et al., 1995). This degeneracy is problematic for robust convergence of the fitting algorithm. Initial tests of the fitting with the ellipticity and shear both unconstrained did not always converge and produced flexion results with errors much larger (factors of 10 or more) than with either shear or ellipticity

fixed. Correlation coefficients between the flexion parameters and the shear/ellipticity parameters (when all are free) take typical values of $\rho \sim 0.7$. While this is not an extremely large correlation, in conjunction with the complete ($\rho \sim 1$) shear-ellipticity prevents measurement of the flexion to any precision. To constrain the fitting problem further, the four-dimensional ellipticity-shear parameter space must be constrained in order to better determine the flexion.

Because the shear and ellipticity are spin-2 fields, whereas the flexions are spin-1 and spin-3 fields, there ought not be a similar correlation between the flexion and the shear or ellipticity, so the source of the degeneracy is expected to be in the shear/ellipticity pairs. The flexions are, in a sense, orthogonal distortion effects to the shear. I choose to constrain the space of ellipticity and shear by fixing the shear to be a constant. Since α, E_+, and $E_\times$ are free fitting parameters, I hypothesize that the errors in the input shear field will be absorbed into incorrect measurements of E and α, while the flexion will be largely unaffected. This hypothesis is tested with the set of simulated data fits described in this chapter and errors in the shear model are well-compensated by the freedom in the ellipticity parameter while still allowing for an accurate flexion measurement.

The choice of fixing the shear instead of the ellipticity is motivated by the ability to choose an input shear which is physically motivated by empirical data. In application to a cluster of galaxies, a tentative shear model can me assumed based on an estimate of the mass of the cluster (e.g., from X-ray observations or optical richness). There is no specific *a priori* constraint on the ellipticity of individual galaxies. Once the flexion fields are measured, the shear derivatives across the entire cluster image field can be calculated and integrated to inform and update the input shear model. This could be used to create an iterative joint solution for the shear and flexion fields, where the input shear is corrected based on the output flexion and reused as a new input.

Despite the fact that fits do not converge reliably without fixing either the shear or the ellipticity, an incorrect input shear model does not preclude an accurate flexion measurement, as I will show in these simulations. Half of the datasets described above

fix each shear parameter to the input shear value, and the other half assume a shear value drawn from a normal distribution about the input value with $\sigma_g = 0.1$.

4.2 Intrinsic Parameter Selection

I select the true unlensed elliptical Gaussian parameters uniformly from the ranges described in Table 4.2. The flux ranges from 0.1 to 10 counts/time (the flux units are arbitrary). The image size α ranges from 1.5 pixels (FWHM$\sim$0.″25) to 8 pixels (FWHM$\sim$1.″2). The magnitude of the ellipticity is drawn from a distribution where

$$p(|E|) = \frac{1}{\pi\sigma_E^2} \frac{\exp(1/\sigma_E^2)}{\exp(1/\sigma_E^2) - 1} \exp\left(-\frac{|E|^2}{\sigma_E^2}\right). \tag{4.1}$$

The spread in ellipticity σ_E is set at 0.2. This distribution is the same as is used in Schneider (1996) for testing the generalized method for shear lensing aperture densiometry with a realistic distribution of galaxy axis ratios. Ellipticities with $|E| < \sigma_E$ are nearly uniformly distributed, and large ellipticities are exponentially disfavored. The phase of the ellipticity is drawn from a uniform distribution between 0 and 2π. The center offset θ_c is not selected randomly, but rather the lensed data image is created such that the centroid of the image located at the image center.

In the datasets using an intrinsic Sérsic profile, the index is selected uniformly from 0.2 to 5, which is a wide range that includes most of the plausible galaxy image profiles of this type, as profiles with smaller indices become very sensitive to errors in background due to large wings, and profiles with larger indices are sharply truncated for $r > \alpha$ (e.g., Peng et al., 2010).

4.3 Lensing Parameter Selection

For the datasets with randomly selected lensing parameters, each lensing parameter is selected from the circular regions with $|g| < 0.5$, $|\Psi_1| < 1 \times 10^{-3}$ pixels^{-1}, and $|\Psi_3| < 1 \times 10^{-3}$ pixels^{-1}: for HST pixel scale, this limits the flexion to be less than 0.02 arcsec^{-1}. The phase of each complex field is selected uniformly from 0 to 2π.

The limit on the flexion fields maintains the approximation of the flexion being a small correction to the lensing transformation. The effect of flexion scales as $\sum_n |\Psi_n|\alpha$, a dimensionless quantity that should be much less than unity across the data image. This dimensionless figure of merit is less than 0.02 for the parameter ranges included. At the limits of the parameter range in the random parameter selection cases (datasets 1 and 2) there will be some aphysical simulated images produced, as some combinations of shear, flexion, and ellipticity push the bounds of the applicability of the AIM for lensing measurements. However, for real data the more extremely distorted objects are those which are identified for strong lensing studies and are not the ideal candidates for AIM analysis. Table 4.3 shows the fraction of fits converged for each dataset, along with several other figures of merit.

The limit on shear prevents the magnification from becoming singular. Adapted from Schneider & Er (2008) Equation (13), the determinant of the lensing transformation Jacobian (the inverse of the magnification) is given by

$$\det J = 1 - gg^* - \eta\theta^* - \eta^*\theta, \tag{4.2}$$

where θ is the usual complex image plane position and

$$\eta \equiv 4\left(\Psi_1 + 2(g\Psi_1^* + g^*\Psi_3)\right). \tag{4.3}$$

If the product of the flexion and the image scale is constrained to be small, $|\eta|$ will be small. From the parameter ranges described above, $\alpha|\Psi_n| \lesssim 0.02$. Therefore, the main consideration for preventing a singular magnification is the magnitude of the reduced shear. By restricting the shear magnitude to be away from unity, the determinant will be non-zero and the magnification will not become singular.

In the other two thirds of the datasets (3–6), the lensing parameters are derived from a SIS lens model, where for an Einstein radius θ_E and lensed image position $\theta_0 = r\exp(i\phi)$ from the lens centered at the origin, the lensing fields are

$$g = \frac{\theta_E}{2r - \theta_E} e^{i2\phi}, \tag{4.4}$$

$$\Psi_1 = -\frac{\theta_E}{8r^2 - 4r\theta_E} e^{i\phi}, \tag{4.5}$$

$$\Psi_3 = \frac{3\theta_E}{8r^2 - 4r\theta_E} e^{i3\phi}. \tag{4.6}$$

A derivation of the physical shear and flexion field definitions can be found in Lasky & Fluke (2009) and combined with Equations 1.15–1.17 to give these results. For specific parameter values, I draw each of the lensing parameters as before and use them to determine values for θ_E, r and ϕ in Equations 4.4–4.6 as follows: $|g|$ defines r/θ_E, $\Psi_1/|\Psi_1|$ defines ϕ, and $|\Psi_3|$, combined with the value of r/θ_E determined from g, defines θ_E. Then g, Ψ_1, and Ψ_3 are recalculated using the SIS lens model and the original values for the lensing fields are replaced. This procedure maintains the same overall lensing field parameter limits while imposing a randomly selected SIS lens model.

4.3.1 Data Image Generation

The data images are created as follows. For all datasets, an initial image is created using a window image of radius seven times that of the true, input semi-major axis size $A = \alpha\sqrt{(1 + |E|)/(1 - |E|)}$. From this initial image, `AIM_START_PARS` is used to estimate the apparent ellipse parameters and the centroid of the image. Then a smaller data image is extracted from the initial image using a window with radius 1.5 times the apparent semi-major axis size. The choice of the factors 7 and 1.5 is motivated empirically - the former is large enough to include the entire lensed image for the ranges of parameters considered, and the latter is motivated similarly to the Gaussian window function size in Goldberg & Leonard (2007). The radius of $1.5A$ includes the majority of the flux from the image without including excess area with only noise, and corresponds to a diameter slightly larger than the FWHM.

For the randomly selected lensing parameter datasets (1–2), the initial image is created using the AIM described in Chapter 3. However, for the SIS lensing datasets (3–6) the lensing transformation is known exactly. Therefore, the image can be created using Equation 1.11. In terms of the small image offsets in the source and image

planes, β and θ, and image center θ_0, the exact lensing transformation is

$$\beta(\theta) = \frac{\theta - (\delta(\theta_0 + \theta) - \delta(\theta_0))}{1 - \kappa(\theta_0)}, \tag{4.7}$$

where $\delta(\theta) = \theta_E \theta / \sqrt{\theta\theta^*}$. This lensing transformation, if expanded in θ about θ_0 yields the quadratic expansion in Equation 1.13 with the shear and flexion fields defined above. This lensing transformation sets the true value of the fitting parameter $\theta_c = 0$ by construction. With this exact lensing model, I create the large initial data image and extract a smaller stamp as described above.

4.4 Fitting

Each data image is fit using `AIM_FIT_IMAGE` with the error estimate for each pixel set to the constant input value of the image noise. Statistics on the convergence and the quality of the fits in broad strokes can be found in Table 4.3. Overall, the convergence rate is extremely high, and the failures are in cases where the true parameter combinations yield extremely distorted lensed images. Inspection of the failed fits show large axis ratios and/or small curvature radii, or very low surface brightness, none of which correspond to the objects where the AIM is an intended to be a successful lensing measurement method.

The mean and median number of iterations to convergence shows that the fitting procedure arrives at a solution efficiently and that if a fit happens to proceed to the maximum number of 500 iterations, then that is a true non-convergence, since the maximum is well above the usual convergence value. The mean and median χ^2 per degree of freedom values show that the figure of merit in Equation 3.3 is a good statistical measure of the data-model deviations, and that most of the fits converge to χ^2/D.o.F~ 1. A typical data image has 500-1000 degrees of freedom.

4.5 Fit Results

Figures 4-1–4-6 show the fit parameters as compared to the true input parameters for each dataset, along with a line indicating unity. The fit results plotted are a randomly-selected subset of those converged results where $\chi^2/\mathrm{D.o.F} < 1.5$ and $\sqrt{\sigma(\Psi_{11})^2 + \sigma(\Psi_{12})^2} > 1 \times 10^{-5}$ pixels^{-1}. I remove those fits where the flexion errors are extremely small because in roughly 1% of the fits the flexion parameters become very large and become trapped in local minima of the χ^2 surface. This seems to be due to the noise instance and the particular set of parameters in some combination, though it bears further investigation. Since it is a small fraction of the fits, I simply remove them as failures.

From the figures it is clear that overall, even in the case of a Sérsic input profile, the intrinsic parameters are well reproduced. The few major exceptions are the fits where $\log S_0$ and α are overestimated for the Sérsic profile. These parameter are overestimated together, meaning that for cuspy Sérsic profiles there is a greater sensitivity to the peak surface brightness, as the core of the Sérsic contributes a larger fraction of the total flux than for the Gaussian. The ellipticities show a larger variance when the shear parameters are erroneously fixed, with $\sigma(E_n) \sim \sigma(g_n)$, as is expected due to the shear-ellipticity degeneracy. The ellipticity parameters compensate completely for the erroneous shear input.

The one major discrepancy in the shape parameters is in regard to the image center position. The center positions X_c and Y_c show a systematic pixel rounding error. This is due to a code bug in the simulation script when the "true" center position is recorded after selecting the region of the large ($7A$ radius) image which will be cut out for the data image to be fit. This is not an error in the fitting. Because of the bug, there is a discontinuous offset in the difference between the true and fit parameters near the origin, though none of the fit parameter values are affected. This bug can be seen in the X_c/Y_c panels of Figures 4-1–4-6.

Table 4.4 contains the error-weighted RMS variation of the shape parameters after the quality cuts described above. All of the RMS values are quite small with respect

to the parameter ranges, meaning that both the fitting is accurate and the errors returned by the fits yield an accurate quantification of the confidence level of the parameter estimate. The similarly weighted means are all consistent with zero.

Figure 4-7 shows the effect of the point-spread function on the flexion error as a function of the ratio of the image size to the PSF FWHM. The data are presented for three different flux bins: $\log S_0 > 0.5$, $0.5 > \log S_0 > 0$, and $0 > \log S_0$. The error estimate depends minimally on the relative size of the object to the PSF size, so long as the image size is greater than the PSF (when $\alpha/\mathrm{FWHM}_{\mathrm{PSF}} > 1$).

Figures 4-8–4-13 and Table 4.5 show the same results for the flexion parameters, after removing obvious outliers. The plots for the flexions are in residual (Fit – True) values. These plots show that the accurate fits successfully reproduce the input flexion values for all six datasets. Table 4.6 lists the slopes and their errors for linear regressions between the true and fit parameter values for each of the datasets. The constant offset in each regression is consistent with zero.

4.6 Discussion

The AIM described in Chapter 3 is a 12 parameter model with two pairs of parameters which are nearly completely degenerate. These simulations show that as long as the shear is constrained, the flexion can be determined even with errors in the input shear field. Furthermore, even with a variety of non-Gaussian input profiles, the fitting still converges accurately. This is because the AIM fitting traces the overall shape of the surface brightness profile, not its innermost slope. The flexion signal arises from those regions where there is significant surface brightness *away* from the image center: A zero size object cannot produce a flexion signal. The extent of an object is its lever-arm for flexion measurements.

These simulations show that the AIM method for measuring flexion in gravitationally lensed objects with realistic input intrinsic object properties and lensing fields is a viable technique. There are no fatal parameter degeneracies provided that the shear and flexion are appropriately constrained, and the resulting parameter fits are still

accurate. The next step is to apply this method to observational data and to attempt to measure mass structure in a real lensing system. In Chapter 5 I will describe my application of the AIM method to HST observations of the galaxy cluster Abell 1689.

4.7 Tables & Figures

Dataset	Image RMS	True Profile	Lens	Shear Error
1	1.3×10^{-3}	Gaussian	Random	0.0
2	1.3×10^{-3}	Gaussian	Random	0.1
3	1.3×10^{-3}	Gaussian	SIS	0.0
4	1.3×10^{-3}	Gaussian	SIS	0.1
5	1.3×10^{-3}	Sérsic	SIS	0.0
6	1.3×10^{-3}	Sérsic	SIS	0.1

Table 4.1: Parameter selection method and error properties for each of the generated datasets. Each dataset uses a PSF FWHM of 1.8 pixels.

Parameter	Minimum	Maximum	Note
$\log S_0$	-1	1	Units: log(counts/time)
α	1.5	8	Units: pixels
$\|E\|$	0	1	See Equation 4.1
$\arg(E)$	0	2π	–
n	0.2	5	$n = 2$ is Gaussian

Table 4.2: Parameter ranges for intrinsic image shapes. The true center position is zero by construction. The background level is set at 0 and the PSF FWHM is 1.8 pixels. Note that n is only applicable to datasets 5 and 6.

Dataset	%Converged	Mean/Median Fit Iterations	Mean/Median χ^2/D.o.F.
1	99.7	13.5/8	1.11/1.01
2	94.4	15.6/8	1.10/1.01
3	99.8	13.6/8	1.02/1.01
4	99.6	18.4/8	1.28/1.01
5	99.7	15.0/11	3.71/1.17
6	99.7	20.7/11	2.68/1.15

Table 4.3: Overview of the convergence properties for each dataset, including the fraction converged, the mean and median values for the number of iterations needed to converge, and the mean and median χ^2 per degree of freedom of the converged fits.

Dataset	$\log S_0$	X_c	Y_c	α	E_+	$E_\times$
1	0.02	0.23	0.22	0.01	0.01	0.01
2	0.04	0.12	0.08	0.09	0.10	0.06
3	0.02	0.05	0.70	0.07	0.03	0.08
4	0.04	0.38	0.05	0.12	0.12	0.11
5	0.08	0.11	0.27	0.87	0.02	0.01
6	0.17	0.07	0.22	1.12	0.12	0.14

Table 4.4: For each dataset, the error-weighted RMS deviation between the input parameter value and the fit parameter value for the intrinsic ellipse shapes. $\log S_0$ is in arbitrary units, X_c, Y_c, and α are in pixels, and E_+ and $E_\times$ are unitless.

Dataset	Ψ_{11}	Ψ_{12}	Ψ_{31}	Ψ_{32}
1	5.0	9.2	8.8	4.6
2	6.8	2.4	2.0	10.8
3	4.0	9.2	4.6	13.2
4	3.2	5.2	2.6	5.6
5	9.0	3.6	3.4	3.6
6	4.4	2.4	6.2	6.0

Table 4.5: For each dataset, the error-weighted RMS deviation between the input parameter value and the fit parameter value for the flexion fields. The values are in units of 10^{-3} arcsec^{-1}, assuming a HST ACS pixel scale of $0\farcs05$.

Dataset	1	2	3	4	5	6
Ψ_{11}	0.97 ± 0.04	1.06 ± 0.04	0.96 ± 0.06	0.91 ± 0.07	0.91 ± 0.07	0.94 ± 0.08
Ψ_{12}	1.03 ± 0.03	0.97 ± 0.04	1.09 ± 0.06	1.11 ± 0.07	1.08 ± 0.07	1.00 ± 0.07
Ψ_{31}	0.90 ± 0.05	1.00 ± 0.06	0.94 ± 0.06	0.96 ± 0.06	1.17 ± 0.08	0.90 ± 0.08
Ψ_{32}	1.02 ± 0.06	1.01 ± 0.07	1.03 ± 0.05	0.92 ± 0.06	1.12 ± 0.05	1.18 ± 0.08

Table 4.6: Linear regression slopes for true/fit flexion parameters and their errors. Exact reproduction of the flexions would result in a unity slope. The is no significant constant bias between the true and fit parameters.

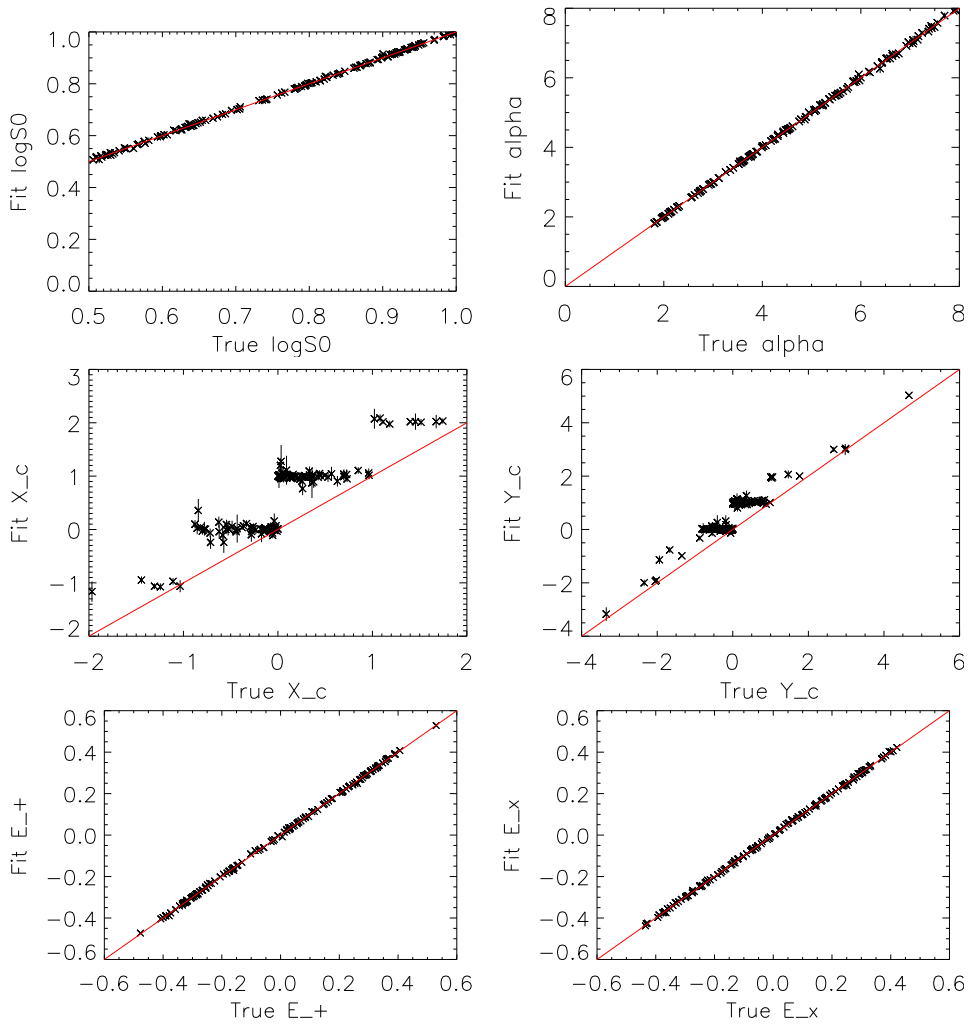

Figure 4-1: Dataset 1: Intrinsic shape results. The converged fit values are plotted against the true input values for each shape parameter. The error bars are those returned by `AIM_FIT_IMAGE`. For clarity, I have only plotted a randomly selected subsample of the full 1000 fits. The red line is a unity line ($y = x$), not a fit to the data. $\log S_0$ is in arbitrary units, X_c, Y_c, and α are in pixels, and E_+ and $E_\times$ are unitless.

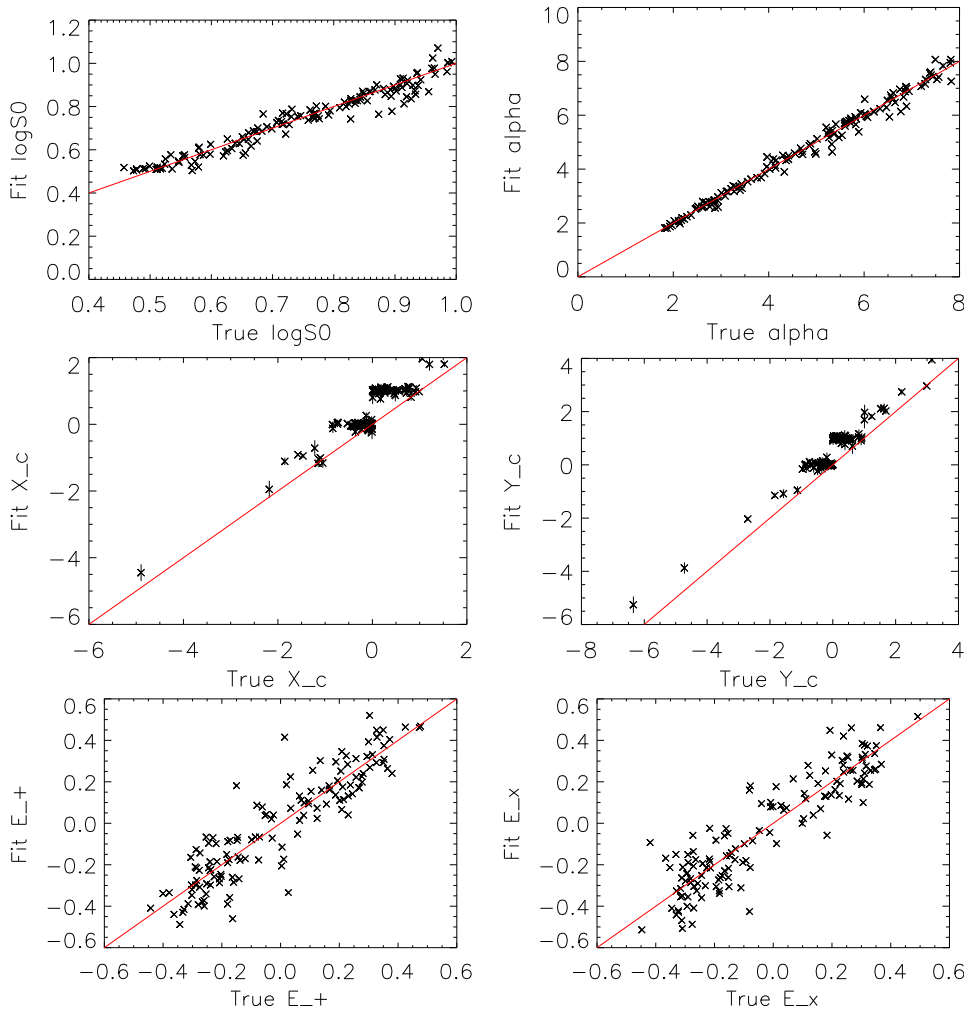

Figure 4-2: Dataset 2: Intrinsic shape results. The converged fit values are plotted against the true input values for each shape parameter. The error bars are those returned by `AIM_FIT_IMAGE`. For clarity, I have only plotted a randomly selected subsample of the full 1000 fits. The red line is a unity line ($y = x$), not a fit to the data. $\log S_0$ is in arbitrary units, X_c, Y_c, and α are in pixels, and E_+ and $E_\times$ are unitless.

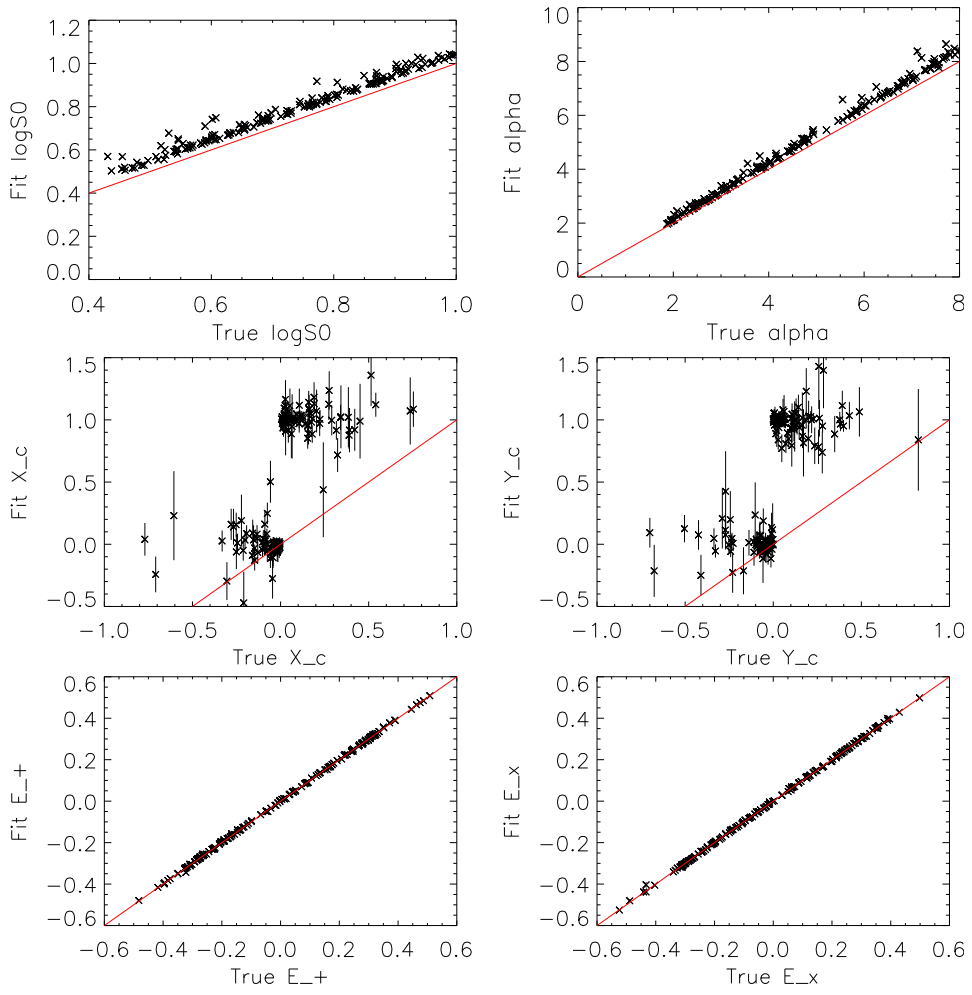

Figure 4-3: Dataset 3: Intrinsic shape results. The converged fit values are plotted against the true input values for each shape parameter. The error bars are those returned by `AIM_FIT_IMAGE`. For clarity, I have only plotted a randomly selected subsample of the full 1000 fits. The red line is a unity line ($y = x$), not a fit to the data. $\log S_0$ is in arbitrary units, X_c, Y_c, and α are in pixels, and E_+ and $E_\times$ are unitless.

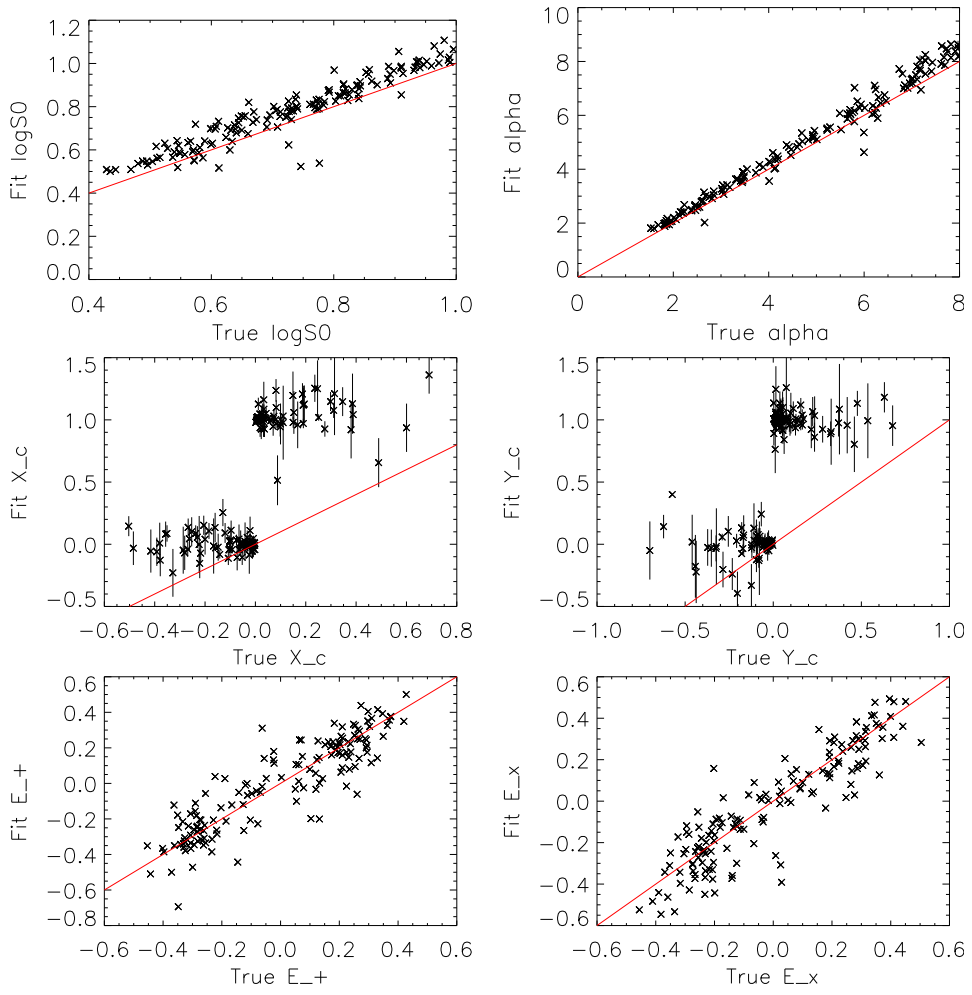

Figure 4-4: Dataset 4: Intrinsic shape results. The converged fit values are plotted against the true input values for each shape parameter. The error bars are those returned by `AIM_FIT_IMAGE`. For clarity, I have only plotted a randomly selected subsample of the full 1000 fits. The red line is a unity line ($y = x$), not a fit to the data. $\log S_0$ is in arbitrary units, X_c, Y_c, and α are in pixels, and E_+ and $E_\times$ are unitless.

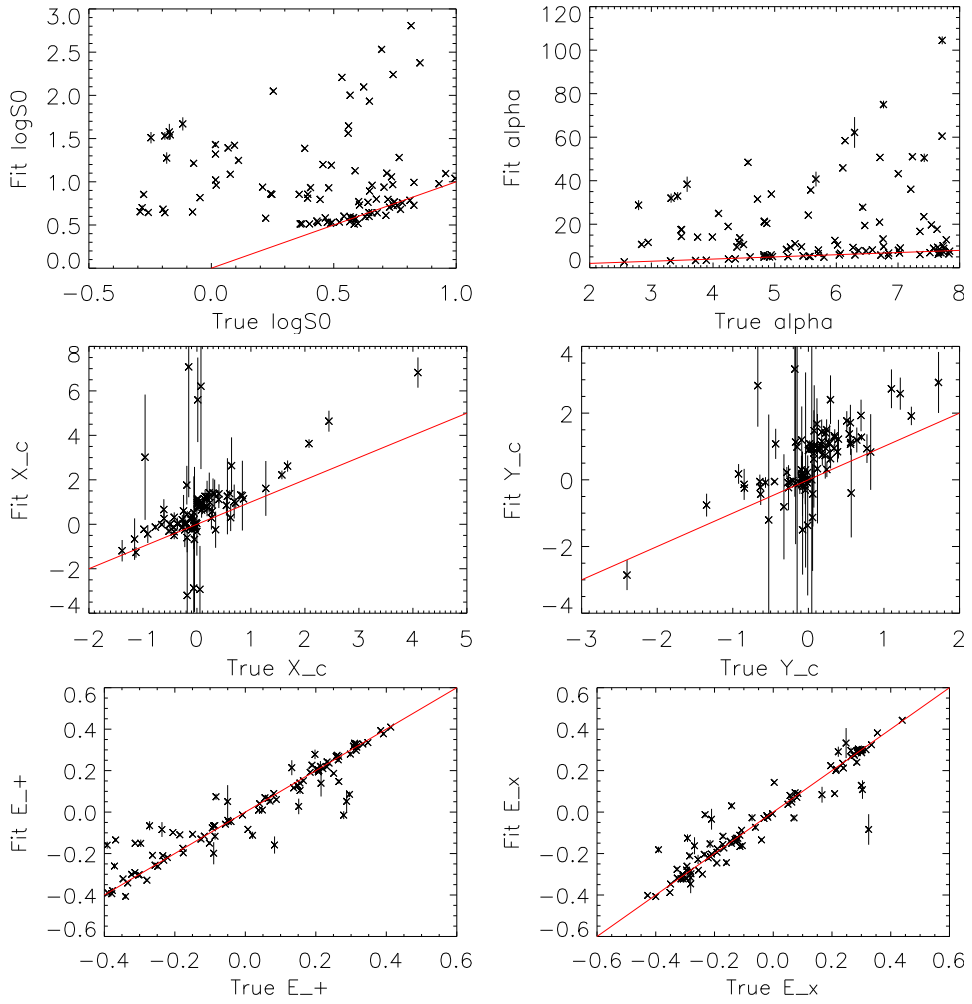

Figure 4-5: Dataset 5: Intrinsic shape results. The converged fit values are plotted against the true input values for each shape parameter. The error bars are those returned by `AIM_FIT_IMAGE`. For clarity, I have only plotted a randomly selected subsample of the full 1000 fits. The red line is a unity line ($y = x$), not a fit to the data. $\log S_0$ is in arbitrary units, X_c, Y_c, and α are in pixels, and E_+ and $E_\times$ are unitless.

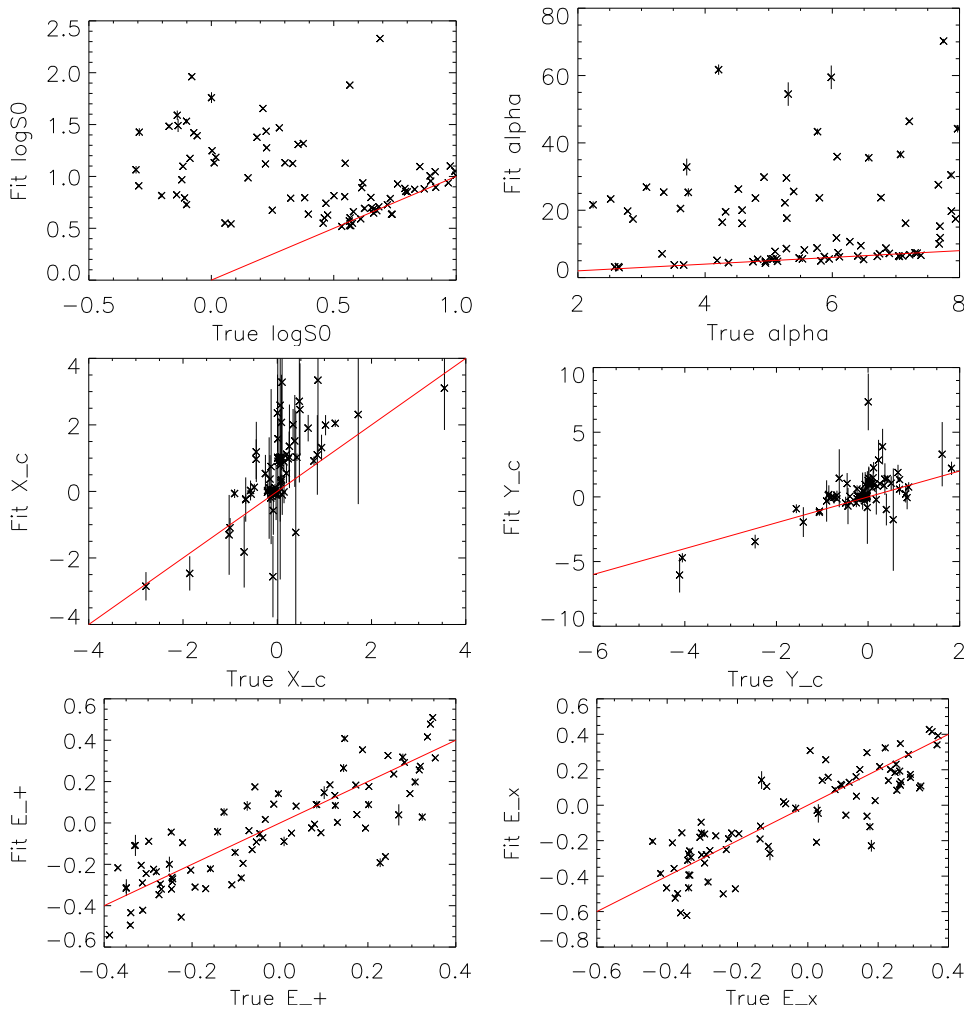

Figure 4-6: Dataset 6: Intrinsic shape results. The converged fit values are plotted against the true input values for each shape parameter. The error bars are those returned by `AIM_FIT_IMAGE`. For clarity, I have only plotted a randomly selected subsample of the full 1000 fits. The red line is a unity line ($y = x$), not a fit to the data. $\log S_0$ is in arbitrary units, X_c, Y_c, and α are in pixels, and E_+ and $E_\times$ are unitless.

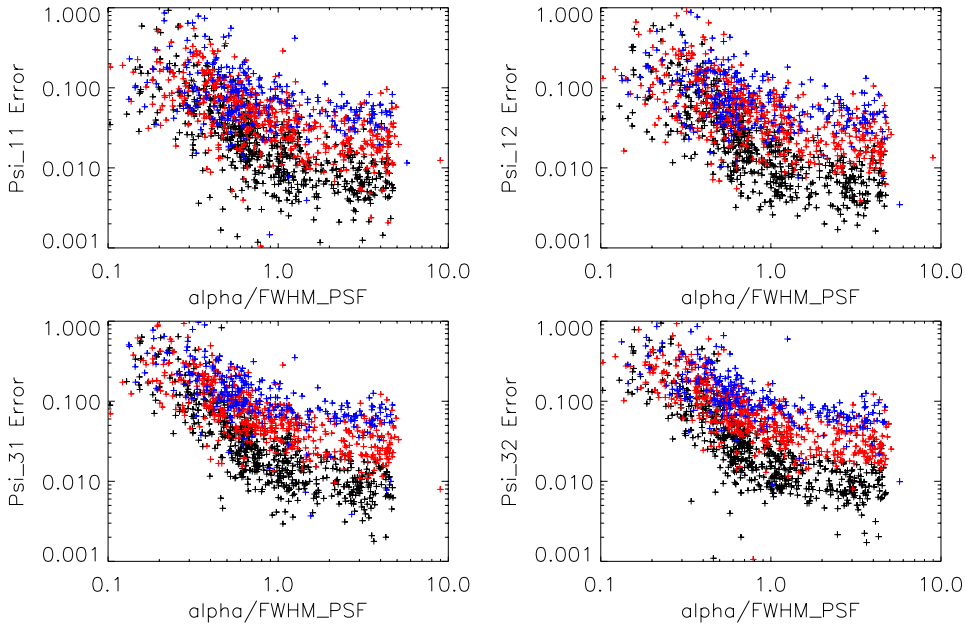

Figure 4-7: Flexion Error as a function of $\alpha/\mathrm{FWHM_{PSF}}$. The different colors are flux bins: black is $\log S_0 > 0.5$; red is $0.5 > \log S_0 > 0$; blue is $0 > \log S_0$. The errors are in arcsec^{-1}, assuming a HST ACS WFC pixel scale of $0\farcs05$/pixel. Note that the flexion errors increase sharply as the PSF becomes larger than the object size.

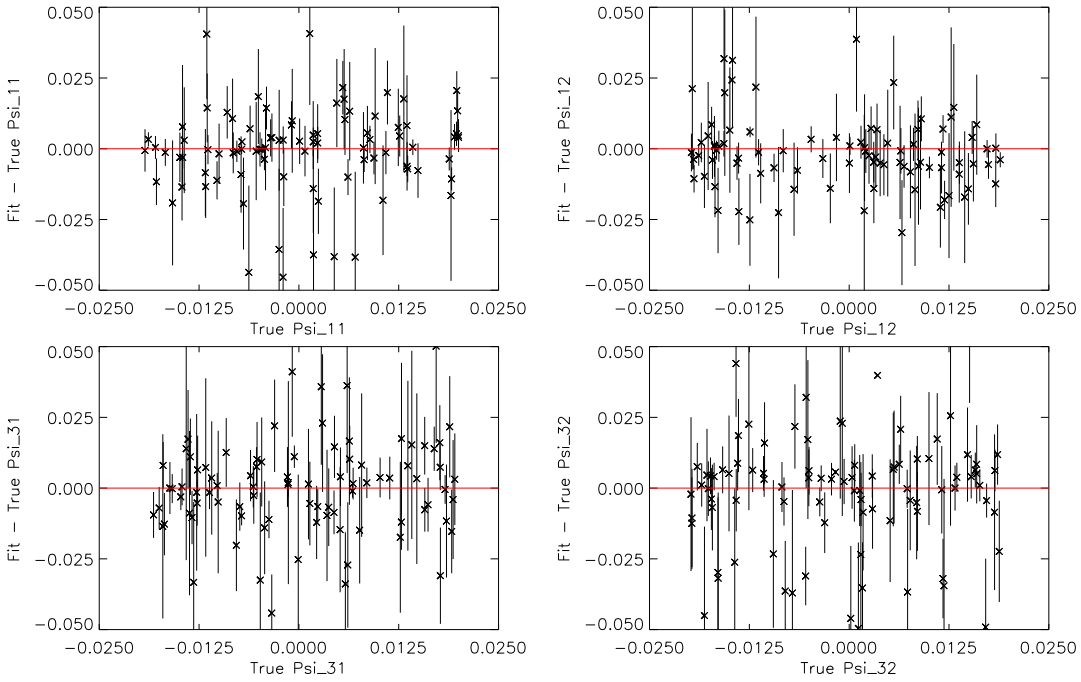

Figure 4-8: Dataset 1: Flexion residuals. This dataset has a Gaussian input profile, randomly selected lensing parameters, and correctly fixed input shear. The converged fit values are plotted against the true input values for each flexion parameter, with error bars are those returned by `AIM_FIT_IMAGE`. The flexion is in units of arcsec^{-1}, assuming a $0\farcs05$/pixel scale. For clarity, I have only plotted a randomly selected subsample of the full 1000 fits. The red line indicates $y = 0$, not a fit to the data.

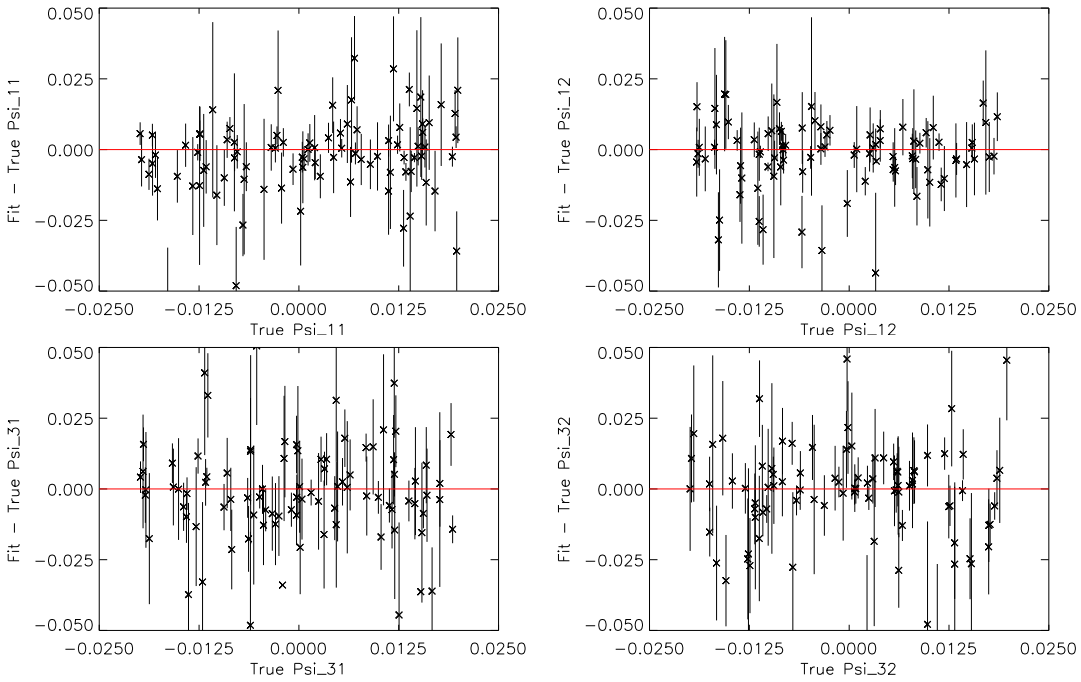

Figure 4-9: Dataset 2: Flexion residuals. This dataset has a Gaussian input profile, randomly selected lensing parameters, and fixed input shear with $\sigma(g) = 0.1$. The converged fit values are plotted against the true input values for each flexion parameter, with error bars are those returned by `AIM_FIT_IMAGE`. The flexion is in units of arcsec^{-1}, assuming a $0\farcs05$/pixel scale. For clarity, I have only plotted a randomly selected subsample of the full 1000 fits. The red line indicates $y = 0$, not a fit to the data.

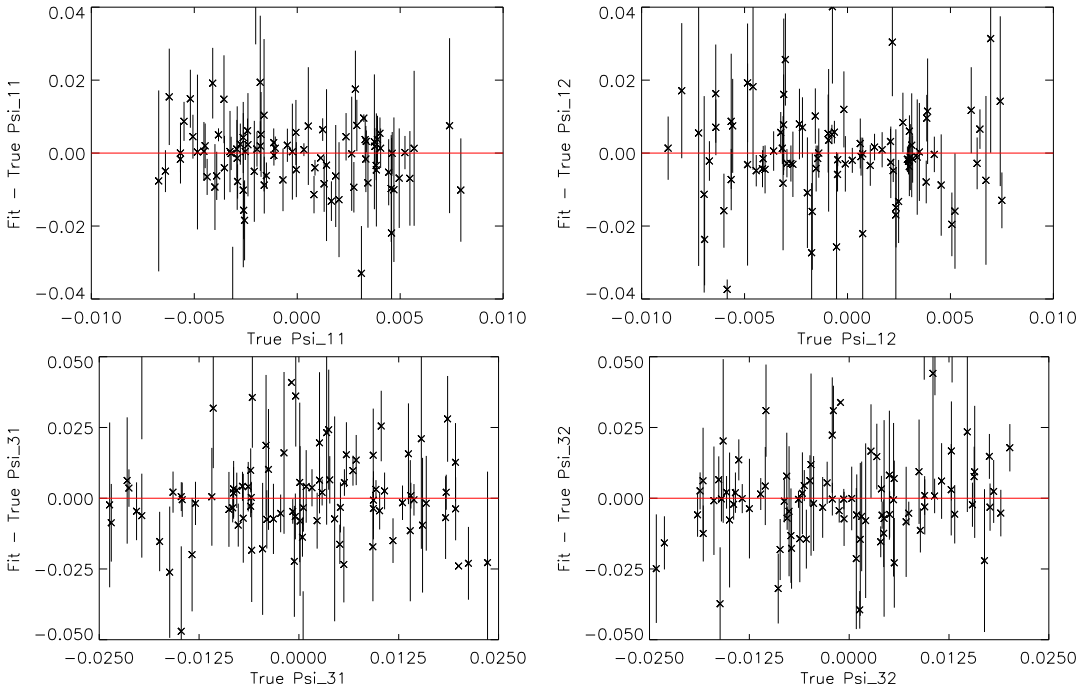

Figure 4-10: Dataset 3: Flexion residuals. This dataset has a Gaussian input profile, SIS selected lensing parameters, and correctly fixed input shear. The converged fit values are plotted against the true input values for each flexion parameter, with error bars are those returned by `AIM_FIT_IMAGE`. The flexion is in units of arcsec^{-1}, assuming a $0\farcs05$/pixel scale. For clarity, I have only plotted a randomly selected subsample of the full 1000 fits. The red line indicates $y = 0$, not a fit to the data.

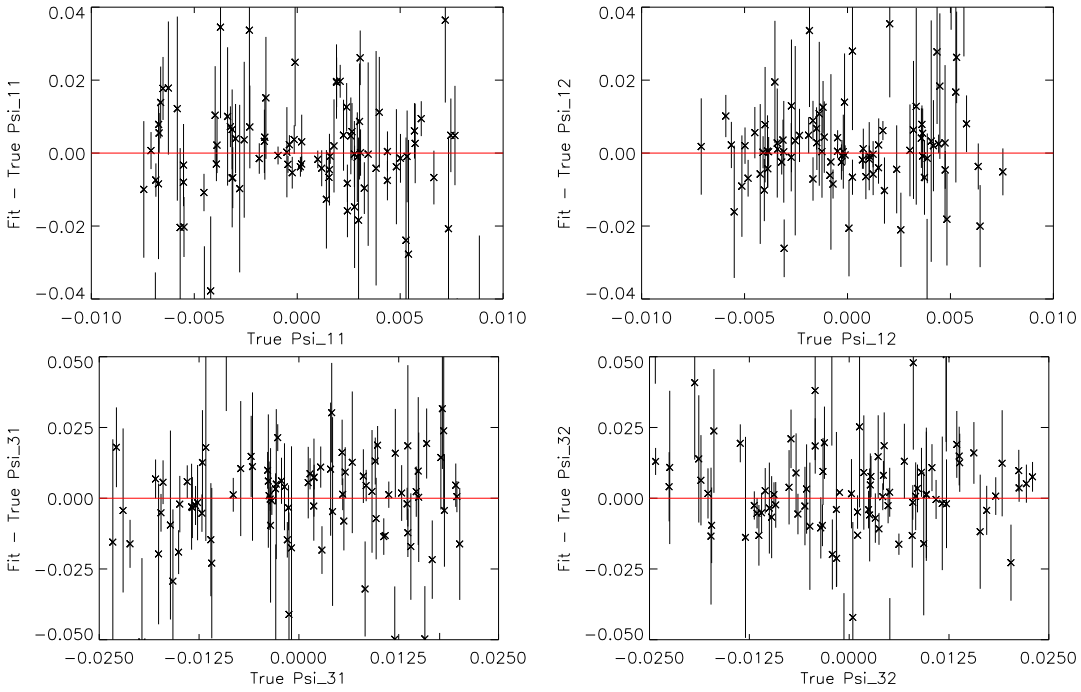

Figure 4-11: Dataset 4: Flexion residuals. This dataset has a Gaussian input profile, SIS selected lensing parameters, and fixed input shear with $\sigma(g) = 0.1$. The converged fit values are plotted against the true input values for each flexion parameter, with error bars are those returned by `AIM_FIT_IMAGE`. The flexion is in units of arcsec^{-1}, assuming a $0\farcs05$/pixel scale. For clarity, I have only plotted a randomly selected subsample of the full 1000 fits. The red line indicates $y = 0$, not a fit to the data.

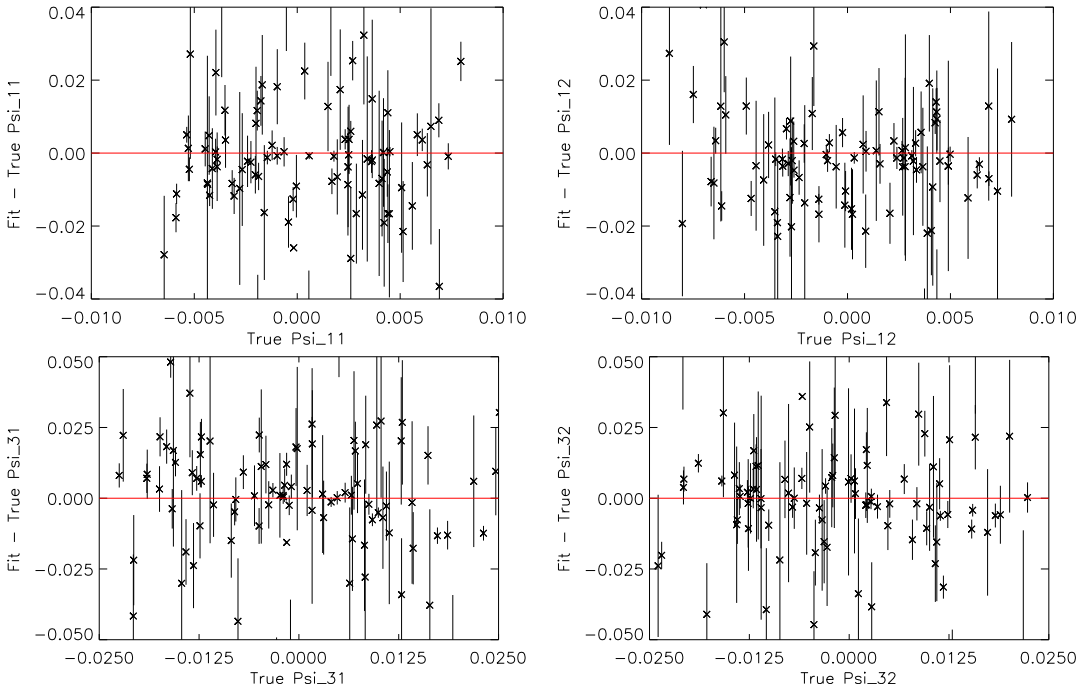

Figure 4-12: Dataset 5: Flexion residuals. This dataset has a Sérsic input profile, SIS selected lensing parameters, and correctly fixed input shear. The converged fit values are plotted against the true input values for each flexion parameter, with error bars are those returned by `AIM_FIT_IMAGE`. The flexion is in units of arcsec^{-1}, assuming a $0\farcs05$/pixel scale. For clarity, I have only plotted a randomly selected subsample of the full 1000 fits. The red line indicates $y = 0$, not a fit to the data.

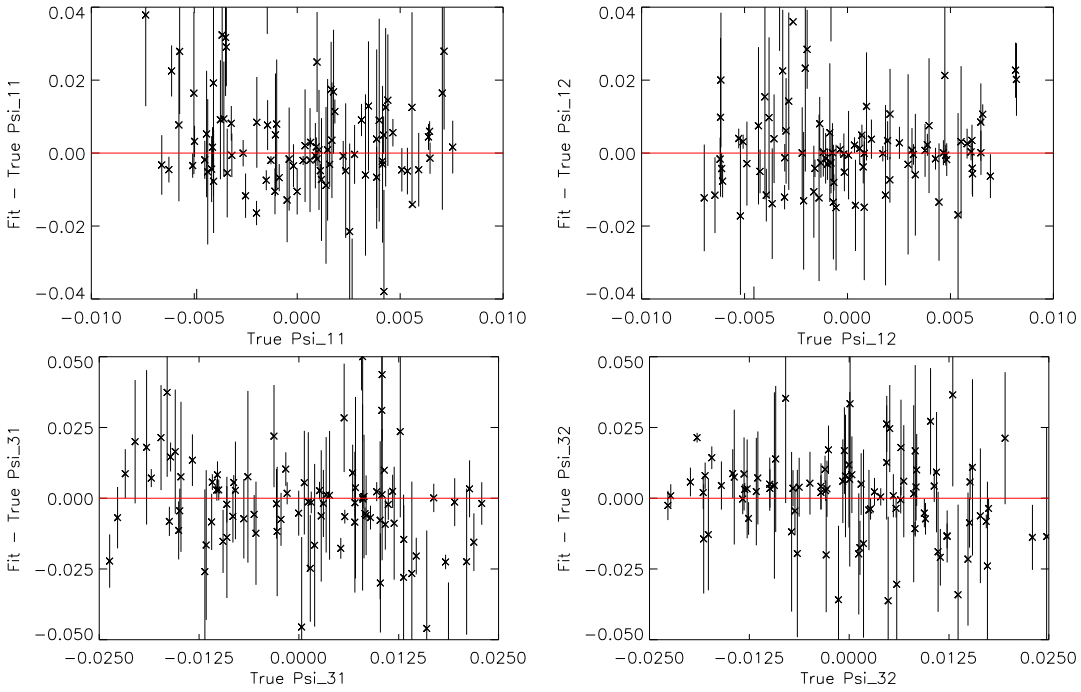

Figure 4-13: Dataset 6: Flexion residuals. This dataset has a Sérsic input profile, SIS selected lensing parameters, and fixed input shear with $\sigma(g) = 0.1$. The converged fit values are plotted against the true input values for each flexion parameter, with error bars are those returned by `AIM_FIT_IMAGE`. The flexion is in units of arcsec^{-1}, assuming a $0\farcs05$/pixel scale. For clarity, I have only plotted a randomly selected subsample of the full 1000 fits. The red line indicates $y = 0$, not a fit to the data.

Chapter 5

Application of the AIM method to Abell 1689

The rich galaxy cluster Abell 1689 is one of the most-studied galaxy clusters in the universe. It is located at a redshift $z = 0.1872$ (Frye et al., 2007) and has a mass $M_{200} \sim 10^{15}$ $M_{\odot}$(Peng et al., 2009). There is some disagreement in the literature regarding the exact mass of this cluster and its distribution. Andersson & Madejski (2004) observed and asymmetry in the X-ray luminous baryon temperature distribution, suggesting either substructure or merger activity. Numerous lensing studies have also observed asymmetrical convergence maps (e.g., Broadhurst et al., 2005; Saha et al., 2007; Okura et al., 2008; Coe et al., 2010). Since flexion traces shear variations, flexion is sensitive to mass variations on smaller scales than is the standard weak lensing approach.

Furthermore, A1689 has become the observational test case for nearly every flexion measurement method to date. Leonard et al. (2007) used Hubble Space Telescope (HST) data to measure flexion with shapelets and detect mass substructure in A1689 with a parametric mass model. They also revisit these data using a mass aperture statistic technique (Leonard et al., 2010). Okura et al. (2008) measure similar structure in A1689 using flexion from HOLICS and ground-based Subaru observations. I apply the AIM method to HST observations of A1689 described below.

5.1 The Data

The data are HST Advanced Camera for Surverys (ACS) images obtained using the Wide Field Camera (WFC). I have obtained data in each of four filters (F475W, F625W, F775W, F850LP) from the HST Legacy Archive (HLA)[1]. These data have been reduced by a standard pipeline to create deep mosaic images of all HST observations of A1689. See Table 5.2 for the total exposure for each filter. The HLA mosaics are background subtracted and photometrically calibrated. I also use a coadded four-filter sum image which provides an extremely deep image for object detection.

The observed field is $3.4'$ (4100 pixels) on a side and square. The angular scale of the cluster is 3.1 kpc/$''$ assuming a concordance cosmology, meaning the field is 0.64 Mpc on a side. The pixel scale is $0\farcs05$/pixel and the point-spread function FWHM is $0\farcs09$ (1.8 pixels). Photometric zero-points for each filter are taken from Sirianni et al. (2005).

5.1.1 Mosiac Image PSF

As noted by Leonard et al. (2007) and Leonard et al. (2010), time-domain effects such as a varying PSF are negligible for flexion measurements. This is expected because of the way flexion is influenced by the PSF. The induced flexion due to an imperfect PSF in terms of the flexion signal in the PSF shape itself is

$$\mathcal{F}_{\rm induced} \sim \mathcal{F}_{\rm PSF}\left(\left(\frac{\Theta_{\rm src}}{\Theta_{\rm PSF}}\right)^4 + 1\right)^{-1}, \tag{5.1}$$

where $\Theta_{\rm src}$ and $\Theta_{\rm PSF}$ are the scales of the source object and the PSF, respectively (Leonard et al., 2007). This means that for well-resolved images ($\Theta_{\rm PSF} < \Theta_{\rm src}$) with a small intrinsic flexion shape, the PSF-induced flexion is negligible. This is particularly true for the small HST ACS WFC PSF, which has a FWHM of approximately $0\farcs09$ (1.8 pixels). This means that by choosing source galaxies which are larger than the PSF, the fine-scale structure of the PSF can be neglected. For source galaxies at

[1]The Hubble Legacy Archive can be found at: http://hla.stsci.edu/

redshifts of $z \sim$1-2, $1''$ corresponds to $\sim$8 kpc. A source galaxy whose intrinsic size is only a few kpc will be well resolved. It is therefore a reasonable approximation that the PSF does not contribute any significant systematic flexion so long as an explicit cut is made on the size of the source objects considered. Since I do not attempt to accurately measure the ellipticity of the intrinsic galaxy shape, any ellipticity induced by the PSF is also unimportant. As in Chapter 4, I use a circular Gaussian PSF with a FWHM of 1.8 pixels when fitting the A1689 source images.

5.2 Data Reduction

In order to extract measurements of the flexion field, there are several steps which need to occur:

1. Generate an initial catalog of objects in the field.
2. Match catalog objects to known foreground or cluster member objects.
3. Use the size of the detected objects to reject of galaxies which are too small to be fit with AIM.
4. Remove the source flux due to each of the foreground/member objects.
5. Generate a catalog from the cleaned image of objects to be used for AIM fitting.

I will describe the details of this cleaning and catalog generation process in this section.

5.2.1 SExtractor

The catalog generation steps are performed with SExtractor (Bertin & Arnouts, 1996) in a two-pass strategy for object detection motivated by that of Rix et al. (2004), though modified for this application. For the first pass, I set the SExtractor input parameters `DETECT_THRESH` and `ANALYSIS_THRESH` to both be $0.75\sigma_I$, where σ_I is the overall RMS background variation of the entire image as estimated by SExtractor,

and DETECT_MINAREA set to 500 pixels. I want to find the largest objects and identify object pixels down to the noise level. The large minimum area above the detection threshold prevents spurious small-object or noise-peak detections that would fill the full image.

I run SExtractor in its two-input-image mode. For the detection image I use the coadded four-filter image, and use one of the individual filter images for photometry. This makes the catalog object detection and numbering uniform across all filters. Included in each filter's catalog is the location, magnitude (using MAG_BEST), the apparent semi-major axis, the semi-minor axes, the ellipse orientation angle, and a local estimation of the background level at the object location. SExtractor also produces three other useful data products: a background image, an object image, and an RMS image.

The background image is a map of the background estimate across the field. Though overall the images have little background, there is some variation over the field, due in large part to intra-cluster light (ICL). Because the ICL is not what I am trying to measure, I want to be sure that it is removed from the smaller image "postage stamps" that I will extract from the full images for AIM fitting.

The object image is the full image with the background map subtracted and any pixels below the detection threshold set to zero. It is a map of only the signal counts from the detected objects. I use this image for cleaning the data image of unwanted foreground and cluster member galaxy objects.

Similar to the background image, the RMS image is a map of the root-mean squared variation of the image about the background across the field. I use this map to define the pixel-by-pixel error σ_n in Equation 3.3, and also as a noise estimate to replace the values of the signal subtracted in the cleaned images.

5.2.2 Known Object Identification

To remove known foreground objects or cluster member galaxies which have been identified spectroscopically, I have compiled a rejection catalog from literature. This includes objects identified by Duc et al. (2002), Coe et al. (2010), or otherwise com-

piled in the NASA/IPAC Extragalactic Database (NED)[2]. All objects with redshifts $z < 0.2$ are included in the rejection catalog. This redshift limit includes the cluster mean of $z = 0.187$ and the spread due to the cluster member velocity dispersion. Any non-member galaxies included in this overlap to higher redshift would give minimal lensing signal regardless, and are well ignored.

I match the positions of objects from the rejection catalog to objects in the SExtractor catalog. Any SExtractor object which has a rejection catalog object within a radius of $1.5\alpha_{SE} = 1.5\sqrt{A_{SE}B_{SE}}$ of the object center is flagged to be cleaned.

5.2.3 PSF-Dominated Object Selection

As noted in §5.1.1, objects which are too small with respect to the PSF are not good candidates for flexion analysis. Therefore I impose a size floor of 2 pixels. Any objects which have $\alpha < 2$ pixels are flagged to be cleaned.

5.2.4 Image Cleaning

Using the rejection catalog, the object, background and RMS images from SExtractor, and the original image,I create a "cleaned" data image as follows. For each object in the catalog, I select the SExtractor background image pixels which are both non-zero and connected to the object center pixel via a friends-of-friends algorithm, namely that pixels are friends if they adjoin on a side (but not corners).

The object counts are subtracted from the original image in these "dirty" pixels and replaced with a value drawn from a normal distribution centered on the background image value and with a standard deviation equal to the RMS image value. A new error image is also created. This new image is equal to the RMS image except where the pixels have been modified in the cleaned image. The cleaned pixels have an error value which is twice that of the RMS image, slightly more than the formal error-propagation value, to account for any systematic uncertainty in these modified areas due to the subtraction.

[2]The NASA/IPAC Extragalactic Database can be found at: http://nedwww.ipac.caltech.edu/

5.2.5 Final Catalog Generation

With the cleaned image produced, I return to SExtractor and generate a catalog of objects in that cleaned image which are at least $2\sigma_I$ above the background (note that σ_I is recalculated for the second pass) and `DETECT_MINAREA` set to 25 pixels. This generates a catalog of faint galaxy sources to be used for AIM analysis. Because of the low detection threshold, there will be some spurious detections, particularly near the edges of the regions where member galaxies were cleaned. However, these will be easily removed with size and peak surface brightness cuts. I cut out any objects with $\alpha < 2$ pixels. After fitting, I will remove any objects with a fit surface brightness $S_0/(2\pi\alpha^2)$ of 5×10^{-3} electrons per square pixel (the calibrated units of the mosaic image). I perform this latter cut after fitting because raising the detection threshold on SExtractor eliminate a similar amount would cut out $\sim 30\%$ of the usable objects as well. The background galaxies desired for this catalog are low-surface-brightness objects which are extended. A larger number of usable background galaxies is obtained by being more inclusive initially and applying quality cuts to the objects after the fitting process.

5.3 Fitting

The selection process described above produces a catalog of 764 objects to be fit using the AIM method described in Chapter 3. I excise "postage stamp" images from the full HST mosaic which are windowed to a radius of $1.5\alpha_{\rm SE}$. Initial parameters are determined with `AIM_START_PARS` and the fitting is performed with `AIM_FIT_IMAGE`. The input shear model is a simple non-singular isothermal sphere (NIS) mass model, with

$$\kappa(\theta) = \frac{\theta_e}{\sqrt{\theta\theta^* + \theta_c^2}} \tag{5.2}$$

and

$$\gamma = \frac{\theta_e \theta^2}{\sqrt{\theta\theta^* + \theta_c^2}} \left[\frac{2\theta_c \sqrt{\theta\theta^* + \theta_c^2} - \theta\theta^* - 2\theta_c^2}{(\theta\theta^*)^2} \right] \tag{5.3}$$

I use θ_e=49.″5 and θ_c=17″, corresponding to a typical redshift for background sources of $z \sim 1-3$, following results of Broadhurst et al. (2005). In that work, the authors note that there is enough uncertainty about the mass structure of A1689 that it is difficult to determine whether a NIS profile is more or less appropriate than the Navarro-Frenk-White (NFW) model (Navarro et al., 1997) typically used in cluster applications.

After fitting, additional cuts are made to the object catalog. First, as in the simulations in Chapter 4, I remove any fits where χ^2/D.o.F > 1.5 or $\sqrt{\sigma(\Psi_{11})^2 + \sigma(\Psi_{12})^2} < 1 \times 10^{-5}$ pixels^{-1}, and as mentioned above I remove any objects where $S_0/(2\pi\alpha^2) < 5 \times 10^{-3}$ e^-/s. This leaves 301 objects in the field, a density of 26.6 objects per arcmin^2. These objects have the set of measured flexion values which I will use to reconstruct a mass structure signal. Figure 5-1 shows the distribution of these 301 objects over the A1689 field. Figures 5-2, 5-3, and 5-4 show representative pairs of galaxies images where the fits were very good ($1.0 < \chi^2$/D.o.F.< 1.1), marginally acceptable ($1.4 < \chi^2$/D.o.F.< 1.5), and ($1.5 < \chi^2$/D.o.F.), respectively. Most of the unacceptable fits are either marginal detections (extremely low signal to noise ratio), or are closely separated pairs of objects. In these latter situations, the fit typically attempts to match the larger object, even if it is located far from the center of the postage stamp, and neither object is well fit (as is the for both galaxies in Figure 5-4).

The precision of the flexion measurements increases with surface brightness, as can be seen in Figure 5-5, though there is also a significant contribution to the accuracy from α, as is expected and can be seen in Figure 5-6.

Appendix A contains an example correlation matrix from one of the A1689 fits showing the typical parameter correlations. Additionally, the appendix contains the full fit parameters and errors for the 100 objects with the best constrained 1-flexion.

5.4 Mass Signal Reconstruction

The inversion of lensing field data to galaxy cluster mass maps in weak lensing, particularly for shear analysis, has converged on a primary method of mass measurements: the *aperture mass statistic*. Schneider (1996) described a method by which a weighted integral of the scaled surface mass density,

$$m(x_0) = \int_{\mathbb{R}^2} \mathrm{d}^2x \; \kappa(x) W(|x - x_0|), \tag{5.4}$$

where $W(z)$ is the window function, could be related to a similar integral of the shear field:

$$m(x_0) = \int_{\mathbb{R}^2} \mathrm{d}^2x \; \gamma_T(x; x_0) Q_{\gamma,W}(|x|), \tag{5.5}$$

where $Q_{\gamma,W}$ is the appropriate weight function for shear determined by the choice of W and

$$\gamma_T(x; x_0) = \gamma(x) \left(\frac{(x^* - x_0^*)}{|x - x_0|} \right)^2 \tag{5.6}$$

is the component of the shear at position x which is tangential to $x - x_0$. Schneider (1996) provides a full derivation of these formulae. This aperture mass statistic approach to mass reconstruction allows structure to be detected at a scale set by the weight function, which goes to zero beyond some radius, and is useful for both cluster mass estimates and for measuring the power spectrum of cosmologically induced shear (Schneider et al., 1998).

Leonard et al. (2009) adapted this approach to flexion, creating a mass-aperture signal for 1-flexion. Similar to shear, the weighted convergence integral can be related to an integral of the flexion:

$$m(x_0) = \int_{\mathbb{R}^2} \mathrm{d}^2x \; \mathcal{F}_E(x; x_0) Q_{\mathcal{F},W}(|x|), \tag{5.7}$$

where

$$\mathcal{F}_E(x; x_0) = \mathcal{F}(x) \left(\frac{(x^* - x_0^*)}{|x - x_0|} \right) \tag{5.8}$$

is the curl-free, or E-mode 1-flexion with respect to x_0 and $Q_{\mathcal{F},W}$ is the appropriate 1-flexion weight function determined by the choice of W. See Leonard et al. (2009) for a full derivation. Leonard et al. (2009) also describe two families of weight functions $Q_{\mathcal{F}}$ which are appropriate for flexion inversion, though these families are by no means exhaustive. This approach to mass reconstruction is a two-dimensional extension to the divergence theorem, though using a weighted window function instead of an infinitely thin surface to account for the discrete sampling of the flexion field by the background galaxy locations.

There is one problem: this aperture mass statistic assumes that the physical flexion is known and, due to the mass-sheet degeneracy, this is not possible until an inversion is performed and κ is measured. Leonard et al. (2007) and Leonard et al. (2010) both note significant systematic "B-mode", or divergence free, signals in their measurements. These B-modes are attributed to erroneous shapelet inversions, but it is possible that some of their error comes from not recognizing the significance of the mass-sheet degeneracy in the flexion regime.

However, this approach is not entirely without merit. The strength of this method is to isolate the flexion signal at a particular scale with the choice of the weight function, and measure the component of the flexion which is oriented towards a point (x_0) in the observed field. Ψ_1 can trace such a signal as well. Because the spin symmetry is the same, the E-mode signal of $\mathcal{F}$ and Ψ_1 are coaligned or anti-aligned, depending on the sign of $1-\kappa$. The mathematical description of $m(x_0)$ works analogously for Ψ_1, except that the statistic is $MK(x_0)$, where

$$MK(x_0) = \int_{\mathbb{R}^2} \mathrm{d}^2x \; \Psi_{1,E}(x; x_0) Q_{\mathcal{F},W}(|x|) = \int_{\mathbb{R}^2} \mathrm{d}^2x \; K(x) W(|x - x_0|), \tag{5.9}$$

where

$$K(x) = -\frac{1}{4} \log |1 - \kappa(x)|. \tag{5.10}$$

So instead of an weighted integral average of the surface density, it is a weighted integral average of the logarithm of the difference between the convergence and unity. But because it is a function of the surface mass density, K will trace the same mass

structure as κ.

For my selected, well-fit objects, I create a discrete version of this quantity (following Leonard et al., 2010):

$$MK(\theta^{(n)}) = \sum_j \Psi_{1,E}(\theta^{(j)};\theta^{(n)})Q(|\theta^{(j)}|;l,R)w_n. \tag{5.11}$$

Here $\theta^{(j)}$ indicates the position of the jth fit object, $\theta^{(n)}$ indicates the nth point in a 500×500 point grid of points which I build the reconstruction on, w_n is a weighting by the inverse square of the flexion error, and $Q(|\theta^{(j)}|;l,R)$ indicates the polynomial weight function

$$Q(r;l,R) = -A\frac{2+l}{2\pi}x\left(1-\frac{x^2}{R^2}\right)^{1+l} \qquad A = \frac{4}{\sqrt{\pi}}\frac{\Gamma(7/2+l)}{\Gamma(3+l)} \tag{5.12}$$

from Leonard et al. (2009). As in Leonard et al. (2009) and Leonard et al. (2010), I use three values of l and four values of R: 3,5, and 7, and 45″, 60″, 75″, and 90″, respectively. The peak signal arises from objects located near $0.2R-0.3R$, depending on l, and the weighting is narrower in r with increasing l. See Figure 5-7 for a plot of $Q(r;l,R)$ for several values of l. The variety of scales and cutoff powers is useful for separating out the signal from noise instances.

I therefore create twelve maps of the MK statistic, one with each of the filter functions. Because the systematics of the MK statistic are not well investigated to date, it is more appropriate to compare the observed signal from the 1-flexion to the distribution MK maps expected from the measurements of the flexions and their errors. This sort of "significance map" approach is common for shear aperture mass measurements. The signal map is divided by the standard deviation of a set of maps generated by randomly reorienting the measured ellipticities, in effect comparing the measured mass map to the error signal expected from randomly oriented ellipticities. Since the systematic particulars of such an approach using flexions remain to be investigated fully, I will refer to my maps as "pseudo-significance maps".

To turn the MK map into a pseudo-significance map, I follow a procedure that

differs from Leonard et al. (2010). Rather than randomly reorienting the flexions, I create the error maps by adding a normally distributed random value to each of the measured flexions components with a standard deviation equal to the estimated flexion parameter error, and construct a new MK map. I repeat this 100 times to measure the standard deviation of the randomized maps. I then construct the pseudo-significance map

$$\mathcal{S}(\theta^{(n)}) = \frac{MK(\theta^{(n)})}{\sigma_{MK}(\theta^{(n)})} \tag{5.13}$$

for each filter.

The twelve MK maps, grouped by l values, are presented in Figures 5-8–5-10 as contours overlaid on the A1689 four-filter mosaic image. In all twelve MK maps, there are structures which are coincident with observable galaxy overdensities. Moreover, these structures are persistent between different window indices l and different aperture radii R, indicating that they are a real signal in the data.

5.5 Discussion

What should be made of these results? The application of the flexion mass aperture statistic as I've done here seems to be workable in principle, due to the similarities in the derivative relations between the input flexion field $\mathcal{F}/\Psi_1$ and κ/K. However there may be some underlying restriction to this sort of straightforward application of theory. The aperture mass statistic is a relatively new development in the field of flexion analysis, and as such it does not have a well-formulated set of caveats and conditions for appropriate use, nor is there a solid verification of the mass calibration. Alternatively, these data do show a good agreement between the $\mathcal{S}$ map structure and the observable substructure in the cluster member galaxies.

Figure 5-11 shows a recent high-accuracy mass map from Coe et al. (2010) produced using a strong lensing analysis of multiply imaged galaxies. The figure has been rotated to be similarly aligned to my mass maps. In a broad sense, the mass maps are similar, though both suffer from a lack of data outside the displayed fields, so structures at the extreme edges of the images are tentative. It seems that there

may be some systematic offsets in the location of the $\mathcal{S}$ peaks near the edges of the field when compared to the structure visible in the optical. Within the convex hull of the Coe et al. map, the overdensities in the flexion maps are roughly aligned with the peaks of the strong lensing map. As noted by Coe et al., the strong lensing map presented is one of a family of valid lensing solutions (see the caption of Figure 5-11), so it is unclear what degree deviation between the flexion and strong lensing maps is expected.

A direct comparison of the two techniques and a full validation/calibration of flexion mass maps will require further investigation of the appropriate window functions and their systematics, and of the effect of the discrete distribution of background galaxies for which flexion is measured. Since the different window functions extract information about the flexion at different angular scales, a combination of measurements with different windows will likely be necessary for an accurate conversion of MK to κ.

Overall I deem this a qualified success for the AIM method of flexion measurement. The goal of this chapter was to use real observational data to produce a flexion measurement result using the AIM method, and to that end this is a successful measurement that shows good correlation to other indicators of mass structure. Further work needs to be done to convert the the mass reconstruction to a true, calibrated mass map, and ensure that the measurements can be made in a format that works well with standard weak lensing shear and strong lensing measurements.

5.6 Tables & Figures

Filter	Total Exposure (ks)
F475W Mosaic	9.5
F475W Mosaic	9.5
F475W Mosaic	9.5
F850LP Mosaic	16.6
Total Mosaic	45.1

Table 5.1: The filters and corresponding total exposure times in kiloseconds for the HST ACS WFC mosaic images used.

	DETECT_THRESH	DETECT_MINAREA	σ_I	N_{obj}
Pass 1	0.75	500	1.38×10^{-3}	1006
Pass 2	2.00	25	1.28×10^{-3}	1736
Final catalog	–	–	–	764

Table 5.2: SExtractor Catalog Summary. These are the important catalog input variables and the resulting number of objects detected. The final catalog is produced by removing detections from the pass 2 catalog which are too small.

	Mean/Median Fit Iterations	Mean/Median χ^2/D.o.F.
Pre-cut	28.1/19	5997/1.33
Post-cut	22.9/18	0.911/0.936

Table 5.3: Overview of the convergence properties for each dataset, including the fraction converged, the mean and median values for the number of iterations needed to converge, and the mean and median χ^2 per degree of freedom of the converged fits.

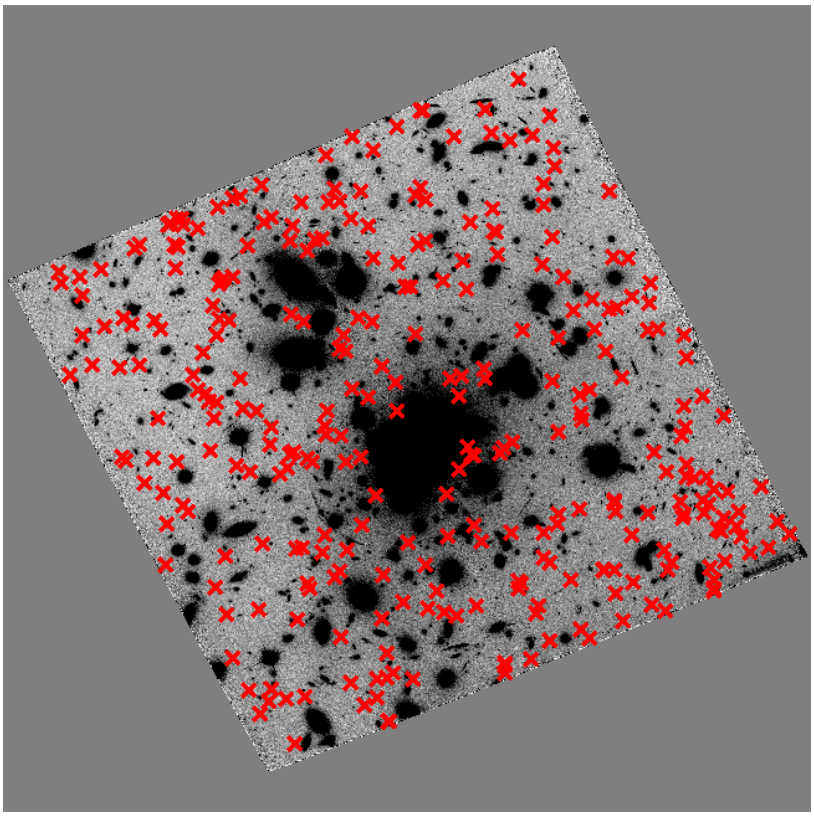

Figure 5-1: Distribution of flexion sources. Each red X marks the location of one of the objects which provided a flexion measurement suitable for use in the mass reconstruction.

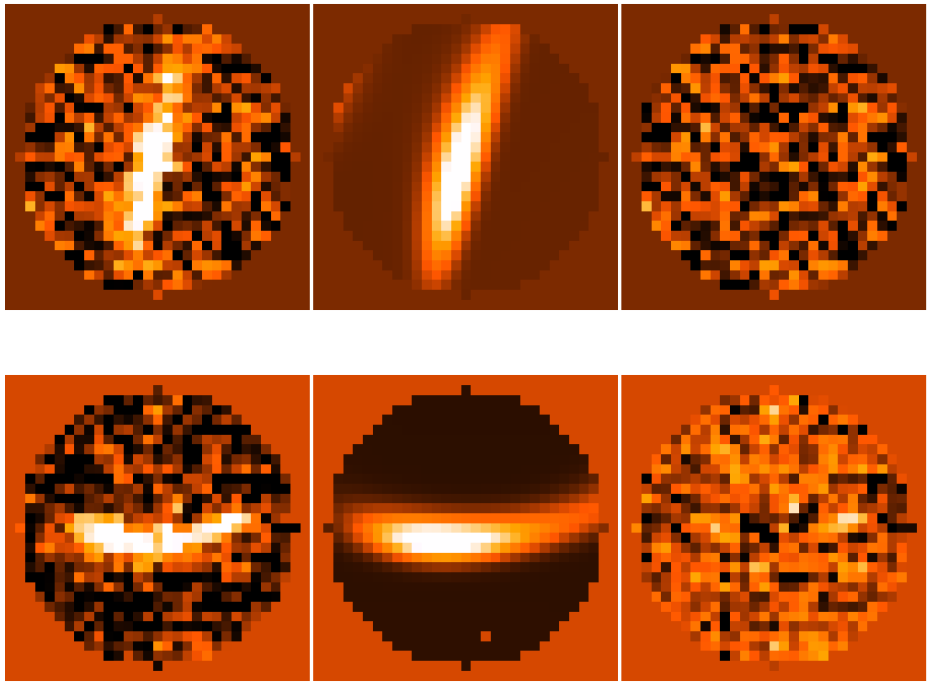

Figure 5-2: Two of the best fit galaxy images in the A1689 field. From left to right, presented are data, fit, and residual images. Both of these objects has $1.0 < \chi^2/\text{D.o.F.} < 1.1$. The color scales are constant horizontally, though they have been changed between the upper and lower objects to emphasize any structure.

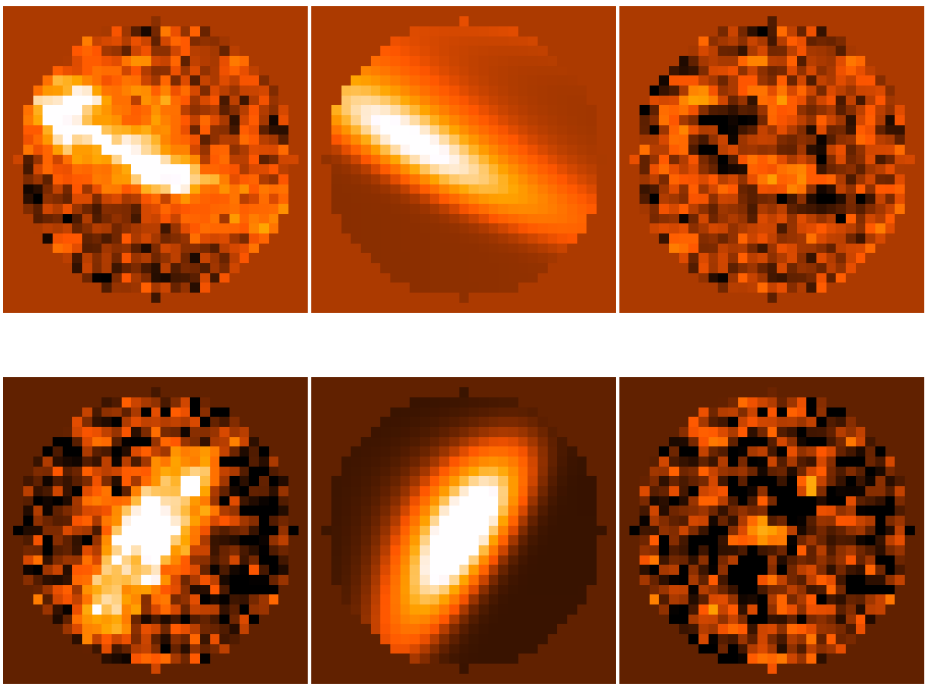

Figure 5-3: Two of the galaxy images in the A1689 field which are just below the selection cutoff of χ^2/D.o.F.< 1.5. Both of these objects has $1.4 < \chi^2$/D.o.F.< 1.5. From left to right, presented are data, fit, and residual images. The color scales are constant horizontally, though they have been changed between the upper and lower objects to emphasize any structure.

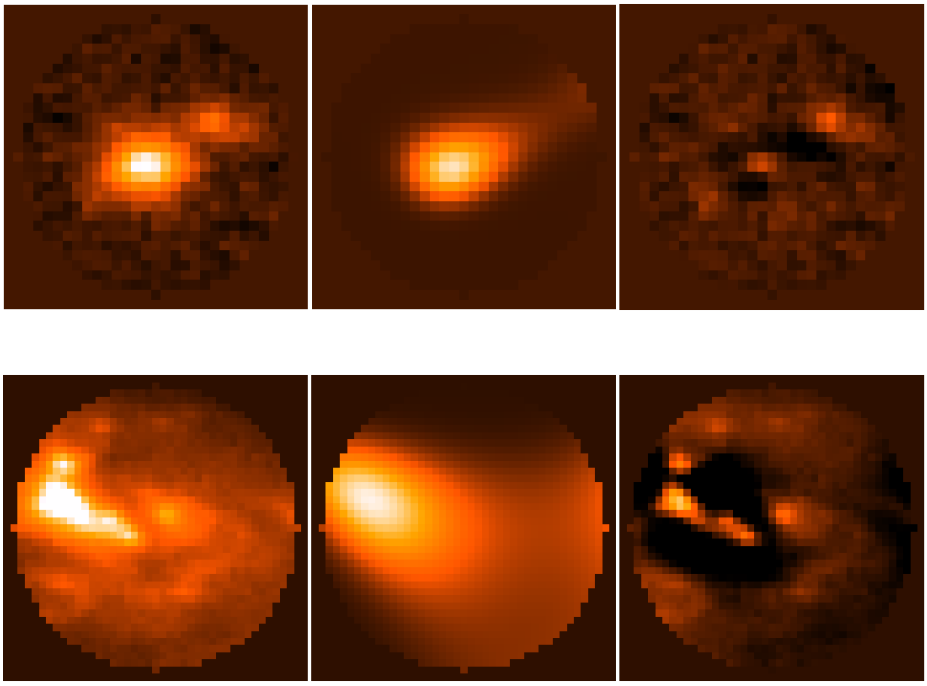

Figure 5-4: Two of the galaxy images in the A1689 field which exceed the selection cutoff of χ^2/D.o.F.$<$ 1.5. From left to right, presented are data, fit, and residual images. The color scales are constant horizontally, though they have been changed between the upper and lower objects to emphasize any structure.

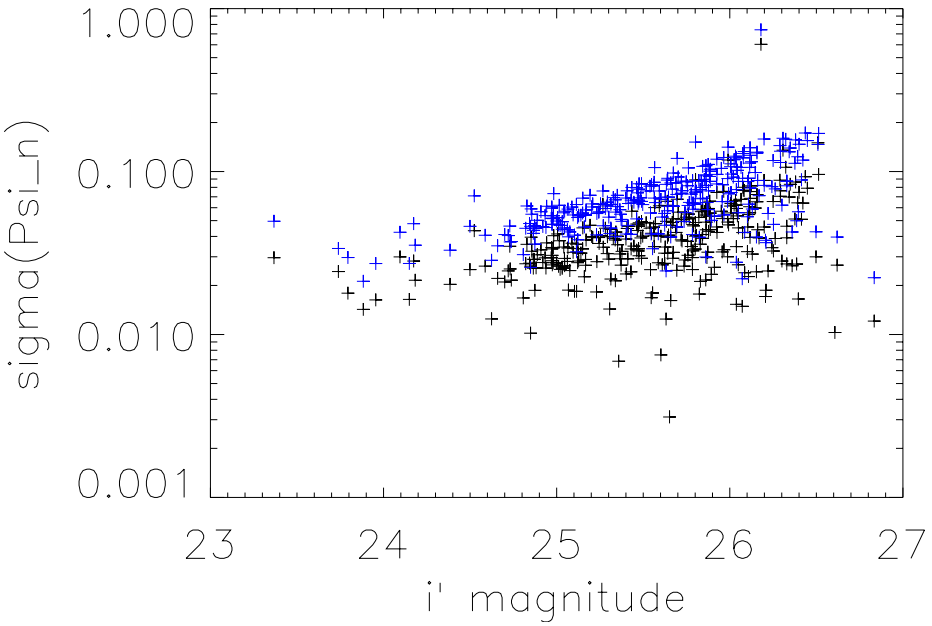

Figure 5-5: Measured flexion error versus observed F775W magnitude, calibrated to standard HST zeropoints. The black points are for $\sigma(\Psi_1) = \sqrt{\sigma(\Psi_{11})^2 + \sigma(\Psi_{12})^2}$, and the blue points are for $\sigma(\Psi_3) = \sqrt{\sigma(\Psi_{31})^2 + \sigma(\Psi_{32})^2}$. Note the drop in error by a factor of nearly 4 from F775W=26 to F775W=25, as well as the systematic larger error on Ψ_3 as compared to Ψ_1. Flexion errors are in units of arcsec^{-1}.

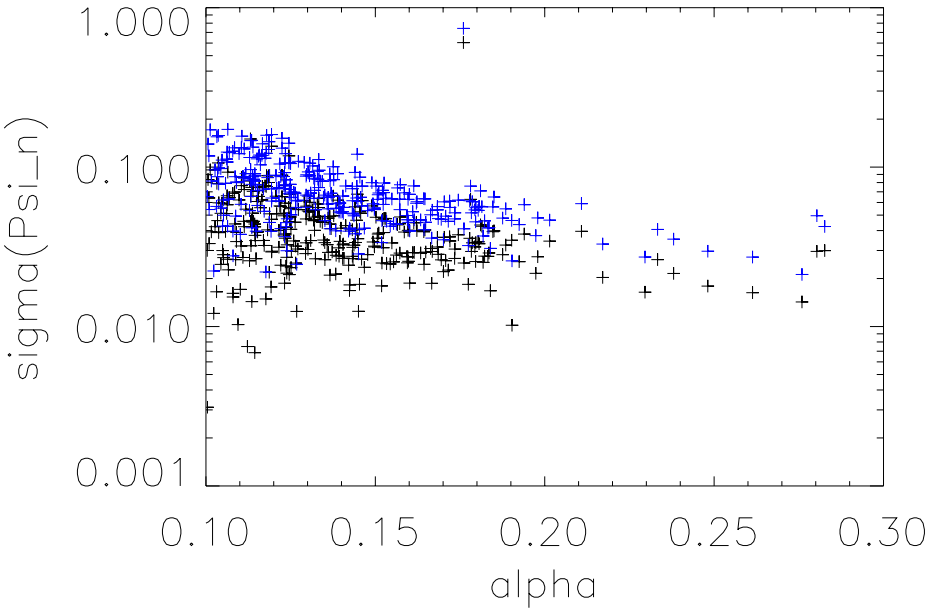

Figure 5-6: Measured flexion error (as in Figure 5-5) versus α. The black points are for $\sigma(\Psi_1)$, and the blue points are for $\sigma(\Psi_3)$. Note the systematic larger error on Ψ_3 as compared to Ψ_1. Flexion errors are in units of arcsec^{-1} and α is in units of arcseconds.

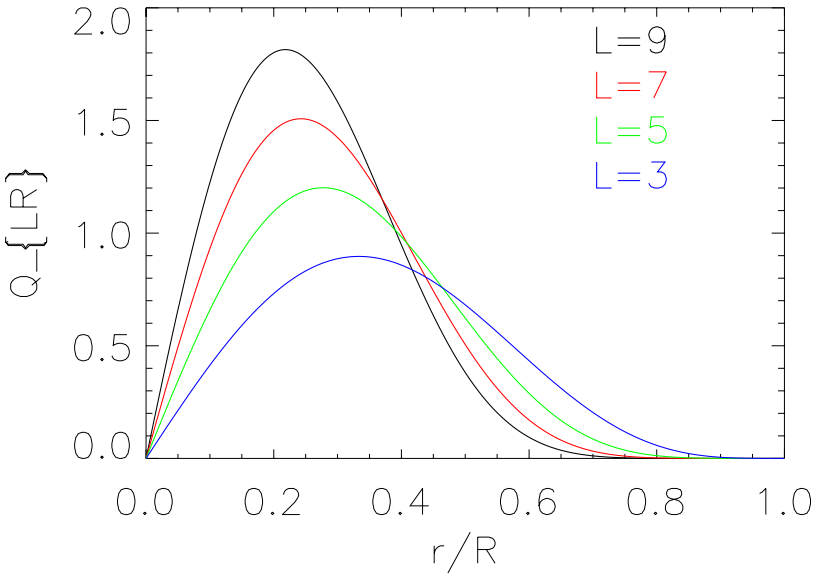

Figure 5-7: Mass reconstruction window functions. As a function of the fraction of the window aperture radius, the window functions are plotted for l =3, 5, 7, and 9. Note that the window contribution peaks at approximately 20–30% of the aperture size, and the width about that peak narrows for increasing l.

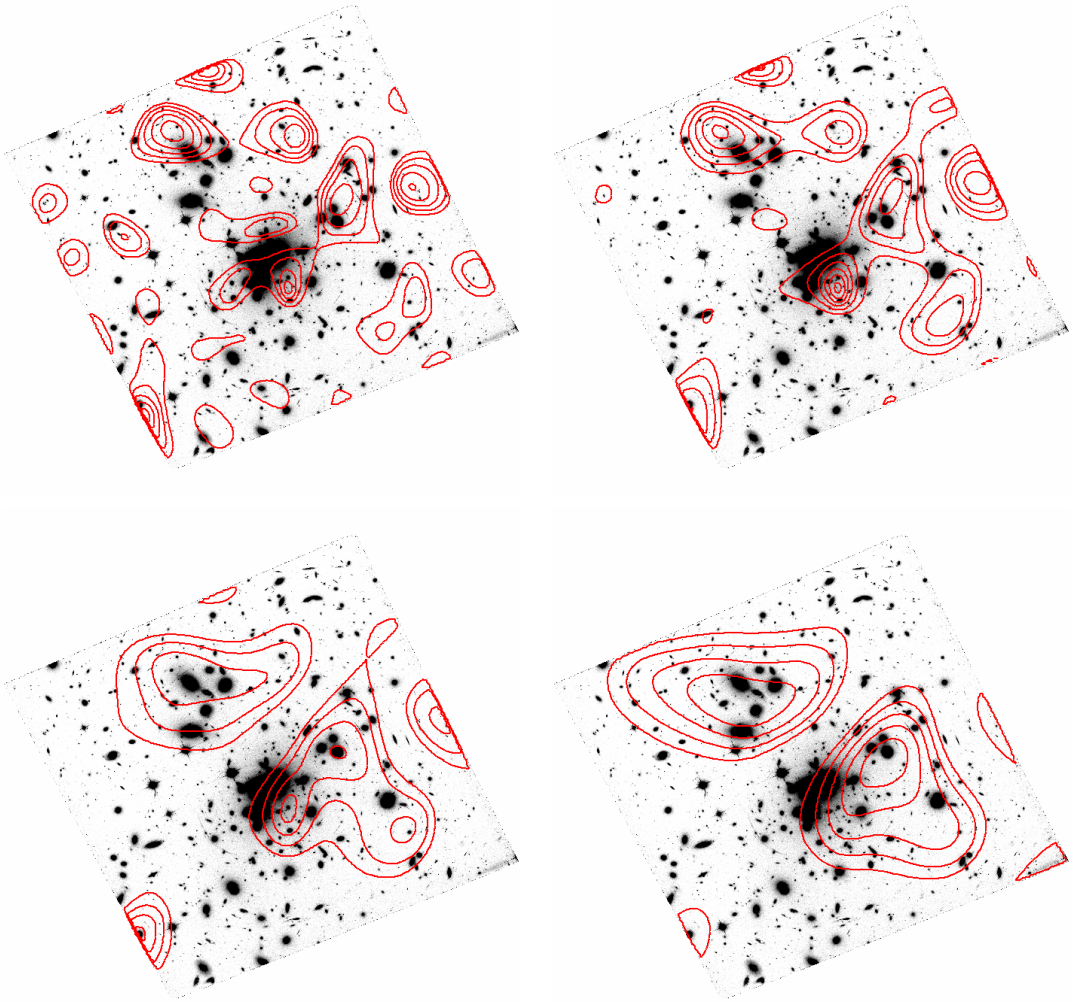

Figure 5-8: $\mathcal{S}$ mass reconstruction pseudo-significance contours with $l = 3$ overlaid on the four-filter A1689 mosaic image. Aperture radii are $45''$ (top left), $60''$ (top right), $75''$ (bottom left), and $90''$ (bottom right). Contours start at $\mathcal{S} = 5$ and increase by steps of 2. In each image, celestial north and east are up and left.

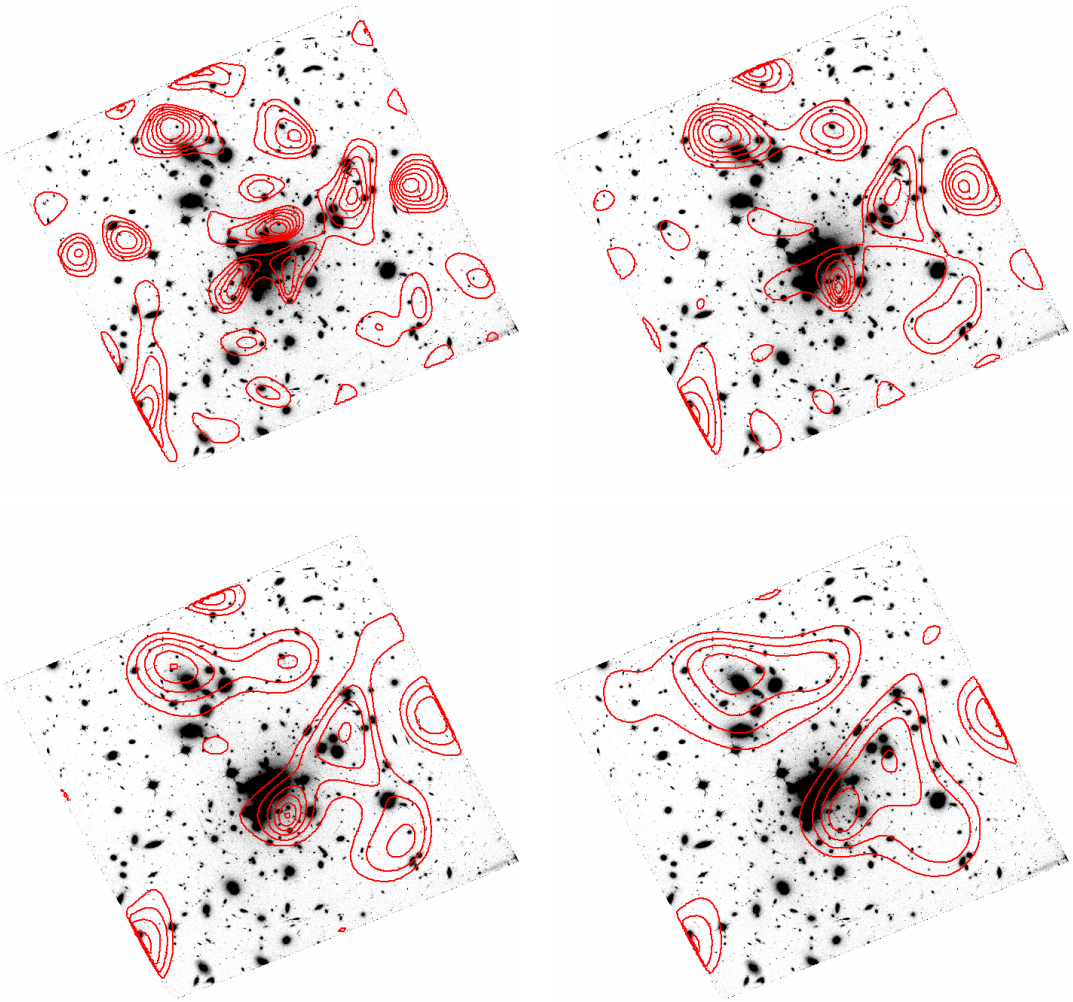

Figure 5-9: $\mathcal{S}$ mass reconstruction pseudo-significance contours with $l = 5$ overlaid on the four-filter A1689 mosaic image. Aperture radii are $45''$ (top left), $60''$ (top right), $75''$ (bottom left), and $90''$ (bottom right). Contours start at $\mathcal{S} = 5$ and increase by steps of 2. In each image, celestial north and east are up and left.

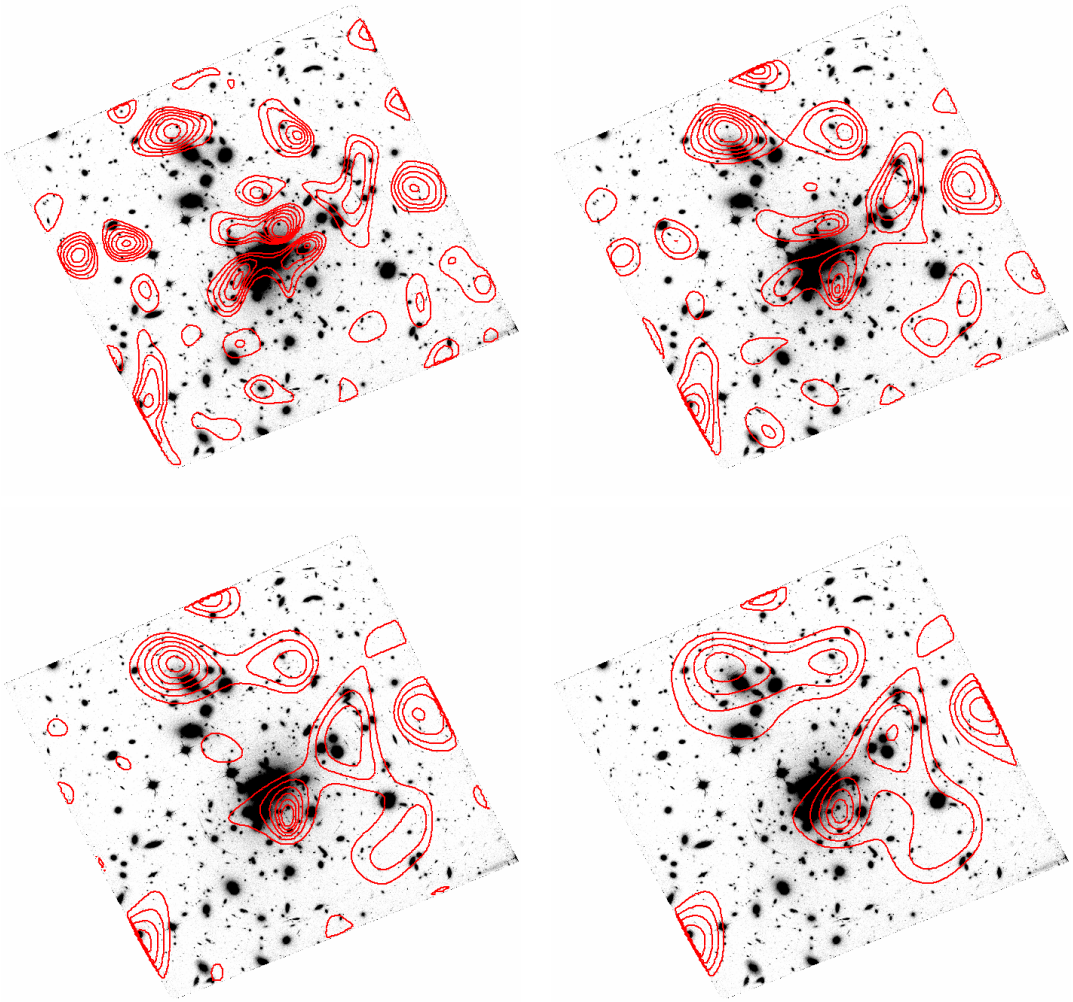

Figure 5-10: $\mathcal{S}$ mass reconstruction pseudo-significance contours with $l = 7$ overlaid on the four-filter A1689 mosaic image. Aperture radii are $45''$ (top left), $60''$ (top right), $75''$ (bottom left), and $90''$ (bottom right). Contours start at $\mathcal{S} = 5$ and increase by steps of 2. In each image, celestial north and east are up and left.

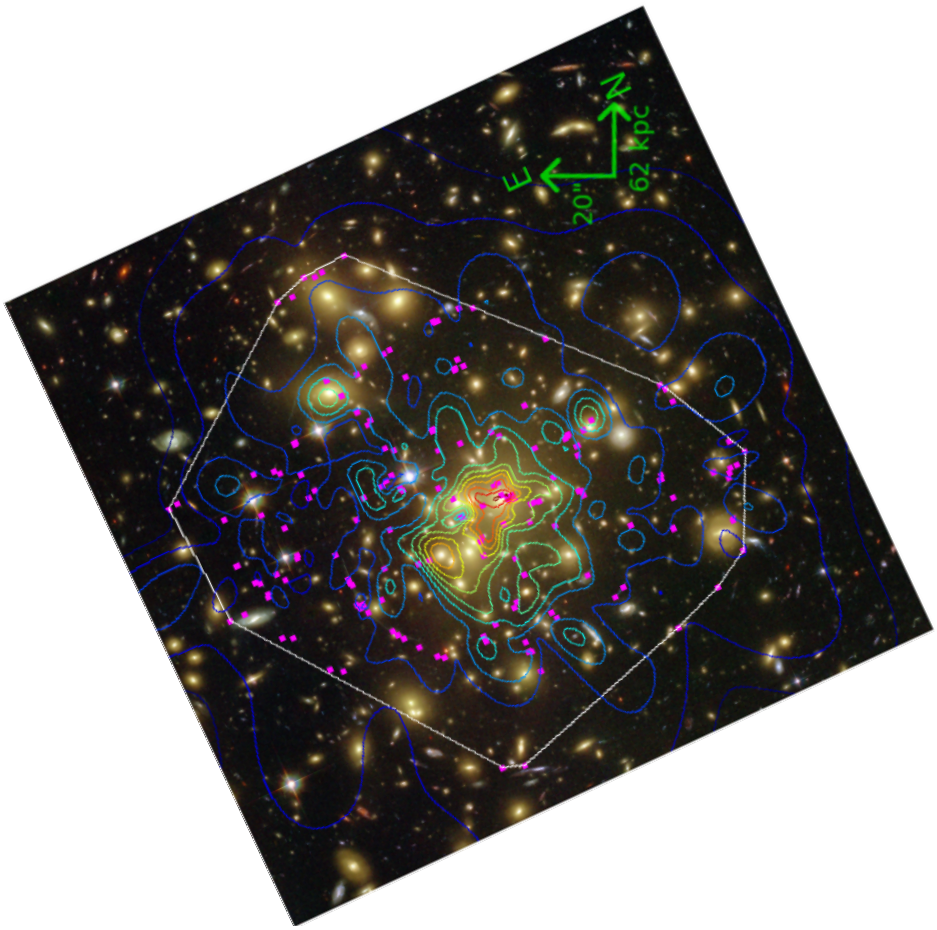

Figure 5-11: Strong lensing mass map from Figure 5 of Coe et al. (2010), rotated to be similarly aligned with the rest of the A1689 images presented. Original caption: *Mass map contours in units of κ_∞ = 1/3 laid over the 3.′2 by 3.′3 STScI ACS g'r'z' color image. The outermost contour, κ_∞ = 0, was also plotted in the previous figure. Pink squares indicate the 135 multiple image positions all perfectly reproduced by our model, and the white line indicates the convex hull. Outside this region, our solution should be disregarded. This solution is not unique but was the "most physical" we found.*

Chapter 6

Summary

Reconstructing the mass distribution of galaxy clusters is a difficult process. As with any measurement, the method used imposes restrictions and systematic biases on the inferred mass. In many cases, this is because the specific mass tracer being used only probes a certain scale or physical regime. For example, using the hot intra-cluster medium to measure the mass can lead to differing estimates depending on whether the plasma is measured with X-ray surface brightness or by the Sunyaev-Zel'dovich decrement. The former signal is dominated by the dense gas nearer to the cluster core, while the latter signal receives a much more significant contribution from the large volume of plasma away from the cluster center (e.g., Motl et al., 2005). As shown in Chapter 2, structure along the line of sight can further complicate mass estimates, particularly when the signal is low.

The same is true of gravitational lensing. Weak lensing shear mass reconstructions are good estimators of total cluster mass at large radii, but there is a resolution floor below which there aren't enough source galaxies per solid angle to overcome the shear signal noise of the intrinsic galaxy ellipticities. Strong lensing provides small scale information, however it can be dependent on the particular alignment of background galaxies with the cluster and it can be very observationally intensive to confirm observed objects as multiple images of the same source. There is also a concern that many strong lensing measurements are biased by line-of-sight structure that may not be directly associated with the cluster.

One solution to these problems is to approach mass reconstruction with numerous techniques valid on overlapping scales so as to maximize the amount of information obtained about the mass distribution while controlling for systematic effects. The specific sources of error for different techniques and the assumptions necessary to apply them to the cluster in question vary, such as hydrostatic equilibrium for X-ray observations, or a lack of significant line-of-sight structure unassociated with the cluster. Comparisons between techniques are necessary to find sources of systematic errors, as the signal dependences will vary.

It is in this context that third-order weak gravitational lensing, flexion, is a powerful tool for galaxy cluster mass measurements. The flexion signal is localized near the cluster core, where the weak lensing approximation of $\gamma \sim g$ breaks down and where there are too few galaxies and the lensing potential is varying too quickly to measure an accurate averaged shear signal. Flexion analysis also applies to a larger fraction of the area of the cluster than strong lensing. Though the strongly lensed *images* are larger than those images used for flexion analysis, strong lensing requires the source images to be located radially interior to the caustics of the lensing potential, whereas the background galaxies for flexion need not be on or immediately near any caustic, a region comprising a much larger fraction of the solid angle of the cluster. Furthermore, flexion does not require the identification of multiply imaged sources and so is less observationally expensive, as accurate strong lensing maps usually require extensive spectroscopy. Flexion analysis bridges the gap between strong lensing and weak lensing, in principle allowing a more detailed and accurate mass mapping than with either alone.

Flexion analysis is a growing subfield, and the specific analysis tools necessary for robust flexion measurements are still being developed. Current methods in the literature, such as shapelets and HOLICs, draw on the rich base of work already done in the strong and weak lensing communities. However, there are drawbacks to each and the best solution has yet to be found.

In order to explore an alternative path, I have developed another method for flexion analysis - the Analytic Image Model. Rather than making assumptions on the

values of derived quantities like shapelet coefficients or surface brightness moments, I instead assume that the lensed image can be well approximated by an analytically lensed elliptical Gaussian. This elliptical Gaussian is a proxy for the image isophotes, which are assumed to be roughly elliptical prior to lensing. The lensed model images are created using a mass-sheet invariant parametrization and the model is optimized over the space of possible model parameters. To validate the method, I have created simulated images with a variety of realistic noise, shape and lensing properties, and shown that the AIM method accurately reproduces the input lensing fields.

And finally, I have applied the AIM method to HST images of Abell 1689. This well-known galaxy cluster is the canonical testbed for flexion. Though the relationship to the physical mass of the cluster is not exact, I apply a modified version of the aperture mass statistic for flexion and measure substructure within the core of the galaxy cluster. This substructure is not newly discovered: it is traced by a local concentrations of cluster member galaxies and has been identified in several previous lensing studies. However, detecting it using this new technique is an important benchmark for validating the AIM method.

There is a great deal of work yet to be done in this field. Though I have shown the AIM method capable of detecting mass substructure in a galaxy cluster, I do not yet have a rigorous estimator of the statistical significance of this detection. Additional testing and simulations will need to be done to understand the statistics of flexion, both as a physical phenomenon and as a tool for mass reconstruction. Additional probes into what sorts of lensed images create problems for the AIM fitting procedure, either in terms of non-convergence or erroneous flexion estimation, as well as direct comparisons to the other methods to understand the strengths and weaknesses of each flexion measurement technique are needed to add robustness to this method of mass structure estimation. Window function optimization for the flexion aperture mass statistic and a thorough evaluation this method in comparison to other mass structure measurement techniques (such as parametric mass models) is necessary to determine the best approach for using flexion to detect substructure in galaxy clusters.

Weak gravitational lensing flexion is an extremely sensitive probe of small scale

substructures in galaxy clusters, and is an important ingredient for the next generation of high-resolution mass maps of galaxy clusters. The AIM method is a good alternative to shapelets and HOLICs as it avoids some of the systematic problems of each while still accurately measuring flexion.

Appendix A

Detailed AIM Results

In this appendix I present a sample correlation matrix for one of the fits in the 301 used for the mass reconstruction in Table A.1. As is typical for models with a large number of parameters, there are several moderate correlations between parameters. The largest of these is the well-known correlation between size and total flux. There are a few correlations between flexion parameters and ellipse parameters, but none of them are so large as to be problematic for the fitting procedure.

Also in this appendix are the detailed fit parameter for the 100 best AIM fit objects, as determined by their 1-flexion signal-to-noise. Tables A.2–A.7 list the fit shape parameters and their errors. Tables A.8–A.10 list the fit flexion parameters and their errors. The right ascension and declination of each object is also listed in Tables A.2–A.4. Each object can be identified with the catalog numbers in each table. The objects are sorted by the 1-flexion signal-to-noise estimate

$$\mathrm{SNR} = \left(\frac{\Psi_{11}^2 + \Psi_{12}^2}{\sigma(\Psi_{11})^2 + \sigma(\Psi_{12})^2} \right)^{1/2},$$

from high to low values of SNR with increasing object number. The SNR for each object is listed in Tables A.8–A.10.

	$\log S_0$	X_c	Y_c	α	E_+	$E_\times$	Ψ_{11}	Ψ_{12}	Ψ_{31}	Ψ_{32}
$\log S_0$	1	0.074	0.261	0.751	-0.028	0.140	-0.196	-0.660	0.160	-0.050
X_c	–	1	0.115	0.086	0.035	-0.021	-0.343	-0.237	-0.242	-0.184
Y_c	–	–	1	0.252	0.186	0.064	-0.292	-0.176	-0.017	0.054
α	–	–	–	1	-0.016	0.155	-0.204	-0.608	0.276	-0.031
E_+	–	–	–	–	1	-0.059	0.044	0.343	0.018	-0.383
$E_\times$	–	–	–	–	–	1	-0.319	-0.379	0.386	0.036
Ψ_{11}	–	–	–	–	–	–	1	0.561	0.405	0.604
Ψ_{12}	–	–	–	–	–	–	–	1	-0.161	0.155
Ψ_{31}	–	–	–	–	–	–	–	–	1	0.382
Ψ_{32}	–	–	–	–	–	–	–	–	–	1
σ	0.012	0.003	0.005	0.003	0.017	0.018	0.010	0.007	0.019	0.016

Table A.1: Sample correlation matrix typical of the Abell 1689 object fits. The matrix has been normalized by rows to the diagonal elements and since the matrix is symmetric, the elements below the diagonal have been removed for clarity. The last row lists the paramter errors for this particular fit.

Object	RA	Dec	$\log S_0$	$\sigma(\log S_0)$	X_c	$\sigma(X_c)$	Y_c	$\sigma(Y_c)$
1	13:11:31.53	-1:20:37.0	-0.301	0.0152	-0.011	0.0037	-0.128	0.0061
2	13:11:28.49	-1:20:59.9	-0.104	0.0116	0.009	0.0031	-0.076	0.0050
3	13:11:34.52	-1:19:32.1	0.077	0.0071	-0.049	0.0019	-0.086	0.0001
4	13:11:28.63	-1:20:31.7	-0.393	0.0223	0.031	0.0063	-0.107	0.0075
5	13:11:25.32	-1:19:57.7	-0.295	0.0154	0.006	0.0048	-0.050	0.0065
6	13:11:28.84	-1:20:13.4	-0.081	0.0001	-0.074	0.0053	-0.046	0.0036
7	13:11:29.87	-1:19:01.4	-0.424	0.0160	0.062	0.0001	-0.025	0.0001
8	13:11:32.36	-1:20:37.2	-0.183	0.0131	-0.032	0.0054	0.022	0.0048
9	13:11:25.38	-1:21:16.2	-0.159	0.0258	-0.091	0.0102	-0.023	0.0105
10	13:11:22.56	-1:21:02.1	-0.046	0.0219	-0.054	0.0145	-0.129	0.0157
11	13:11:35.83	-1:20:59.6	-0.194	0.0147	0.081	0.0058	-0.174	0.0065
12	13:11:33.55	-1:21:06.7	-0.383	0.0133	-0.024	0.0036	-0.113	0.0046
13	13:11:31.18	-1:19:00.1	-0.422	0.0224	0.049	0.0143	-0.022	0.0114
14	13:11:22.66	-1:21:01.2	-0.192	0.0190	-0.066	0.0099	-0.066	0.0191
15	13:11:24.16	-1:20:33.9	-0.479	0.0190	-0.048	0.0061	0.053	0.0069
16	13:11:30.52	-1:22:10.5	0.106	0.0292	0.021	0.0158	-0.080	0.0095
17	13:11:29.88	-1:19:51.4	-0.242	0.0152	-0.090	0.0052	-0.049	0.0074
18	13:11:28.25	-1:20:03.8	-0.401	0.0236	-0.072	0.0077	0.078	0.0100
19	13:11:26.62	-1:20:08.5	-0.072	0.0127	-0.113	0.0049	0.023	0.0061
20	13:11:22.48	-1:21:12.8	0.159	0.0089	0.008	0.0058	0.055	0.0037
21	13:11:33.69	-1:20:18.8	-0.185	0.0382	-0.031	0.0082	0.054	0.0199
22	13:11:36.81	-1:20:36.8	-0.313	0.0139	0.011	0.0042	-0.054	0.0048
23	13:11:26.11	-1:19:43.0	-0.234	0.0001	0.013	0.0035	-0.087	0.0043
24	13:11:33.52	-1:19:11.3	-0.293	0.0247	0.115	0.0142	0.014	0.0078
25	13:11:38.36	-1:19:32.9	0.049	0.0077	0.012	0.0036	-0.053	0.0023
26	13:11:28.57	-1:19:11.2	-0.134	0.0086	0.005	0.0032	-0.064	0.0027
27	13:11:25.12	-1:20:51.8	0.057	0.0388	-0.106	0.0126	-0.130	0.0211
28	13:11:34.64	-1:20:15.9	-0.266	0.0104	-0.056	0.0024	0.021	0.0035
29	13:11:24.09	-1:19:49.7	-0.029	0.0087	0.000	0.0034	-0.032	0.0092
30	13:11:29.75	-1:18:30.9	-0.298	0.0331	-0.103	0.0167	-0.046	0.0078
31	13:11:27.84	-1:20:34.3	0.221	0.0051	-0.025	0.0021	0.011	0.0022
32	13:11:27.07	-1:18:39.8	-0.133	0.0090	-0.069	0.0036	-0.040	0.0037
33	13:11:30.50	-1:22:10.7	0.216	0.0212	-0.278	0.0156	0.100	0.0095
34	13:11:28.20	-1:20:07.3	-0.103	0.0192	-0.088	0.0098	-0.040	0.0114

Table A.2: Sky location, fit and error values of $\log S_0$, X_c and Y_c for the 100 objects in the A1689 field with the best flexion estimates used in this analysis. The right ascension and declination coordinates are for the J2000 epoch.

Object	RA	Dec	$\log S_0$	$\sigma(\log S_0)$	X_c	$\sigma(X_c)$	Y_c	$\sigma(Y_c)$
35	13:11:23.94	-1:21:09.0	-0.460	0.0213	0.009	0.0090	-0.043	0.0069
36	13:11:32.88	-1:19:17.9	-0.220	0.0173	-0.083	0.0108	0.005	0.0072
37	13:11:34.92	-1:20:12.8	-0.401	0.0184	0.001	0.0054	-0.041	0.0171
38	13:11:26.85	-1:19:26.4	-0.462	0.0232	-0.013	0.0092	-0.076	0.0084
39	13:11:30.11	-1:19:34.5	-0.172	0.0500	0.440	0.0354	0.095	0.0092
40	13:11:33.34	-1:19:09.2	-0.255	0.0117	0.020	0.0047	-0.010	0.0038
41	13:11:30.69	-1:21:33.6	-0.177	0.0208	-0.037	0.0121	-0.084	0.0090
42	13:11:32.47	-1:21:20.8	-0.274	0.0128	0.013	0.0039	-0.040	0.0042
43	13:11:31.70	-1:19:56.8	-0.070	0.0130	0.028	0.0046	-0.025	0.0064
44	13:11:23.47	-1:20:17.1	-0.225	0.0126	0.019	0.0036	-0.060	0.0059
45	13:11:23.01	-1:20:50.9	-0.195	0.0173	0.061	0.0098	-0.048	0.0059
46	13:11:30.06	-1:21:06.4	-0.033	0.0126	-0.142	0.0060	-0.034	0.0053
47	13:11:34.34	-1:19:46.4	-0.434	0.0209	-0.058	0.0062	-0.056	0.0100
48	13:11:34.26	-1:21:47.7	0.229	0.0112	-0.077	0.0099	-0.077	0.0124
49	13:11:24.26	-1:19:32.9	-0.183	0.0143	-0.057	0.0051	-0.102	0.0059
50	13:11:26.59	-1:19:16.4	-0.236	0.0154	-0.066	0.0051	-0.034	0.0080
51	13:11:27.91	-1:19:22.5	-0.073	0.0091	0.001	0.0045	-0.006	0.0028
52	13:11:34.59	-1:19:45.8	0.156	0.0064	0.000	0.0043	0.006	0.0043
53	13:11:22.98	-1:20:55.6	-0.300	0.0141	-0.032	0.0067	-0.088	0.0038
54	13:11:34.08	-1:19:01.6	-0.416	0.0001	-0.004	0.0137	-0.012	0.0065
55	13:11:25.34	-1:21:16.2	0.126	0.0347	0.028	0.0211	-0.028	0.0124
56	13:11:34.71	-1:20:21.8	-0.344	0.0171	-0.016	0.0083	-0.050	0.0049
57	13:11:28.05	-1:19:06.3	-0.302	0.0177	-0.094	0.0066	-0.097	0.0071
58	13:11:26.47	-1:20:56.1	0.028	0.0098	-0.071	0.0065	-0.017	0.0041
59	13:11:22.73	-1:21:19.8	-0.400	0.0001	-0.043	0.0073	-0.084	0.0231
60	13:11:33.34	-1:21:59.1	-0.126	0.0169	-0.040	0.0087	-0.014	0.0124
61	13:11:32.81	-1:19:12.4	-0.239	0.0187	-0.088	0.0090	-0.067	0.0069
62	13:11:27.42	-1:21:22.7	-0.235	0.0189	-0.017	0.0102	0.014	0.0079
63	13:11:22.75	-1:21:22.9	-0.034	0.0100	-0.054	0.0060	-0.060	0.0036
64	13:11:34.41	-1:21:32.2	-0.085	0.0115	-0.068	0.0078	-0.017	0.0025
65	13:11:23.55	-1:20:51.6	-0.384	0.0151	-0.040	0.0034	0.052	0.0054
66	13:11:22.10	-1:21:03.8	-0.036	0.0196	0.020	0.0155	-0.037	0.0130

Table A.3: Same as Table A.2.

Object	RA	Dec	$\log S_0$	$\sigma(\log S_0)$	X_c	$\sigma(X_c)$	Y_c	$\sigma(Y_c)$
67	13:11:32.89	-1:20:34.5	-0.089	0.0109	-0.030	0.0059	0.018	0.0044
68	13:11:37.86	-1:19:37.4	-0.158	0.0102	-0.027	0.0039	0.013	0.0033
69	13:11:36.16	-1:20:36.1	-0.140	0.0119	-0.022	0.0049	-0.074	0.0043
70	13:11:35.63	-1:19:27.7	-0.151	0.0097	-0.031	0.0051	-0.070	0.0031
71	13:11:25.06	-1:19:41.8	0.339	0.0192	-0.025	0.0067	-0.141	0.0175
72	13:11:30.35	-1:20:08.9	-0.368	0.0342	-0.053	0.0118	0.041	0.0178
73	13:11:34.24	-1:19:02.6	-0.175	0.0178	0.017	0.0186	-0.056	0.0048
74	13:11:36.86	-1:19:45.6	0.026	0.0102	0.002	0.0040	0.049	0.0054
75	13:11:29.20	-1:21:31.4	-0.044	0.0182	-0.048	0.0102	-0.084	0.0125
76	13:11:29.63	-1:21:14.1	-0.487	0.0265	-0.024	0.0118	0.020	0.0088
77	13:11:26.57	-1:18:44.3	-0.101	0.0117	-0.033	0.0034	0.093	0.0063
78	13:11:34.97	-1:19:58.0	0.038	0.0080	0.002	0.0038	-0.027	0.0036
79	13:11:26.94	-1:21:29.0	-0.095	0.0116	-0.033	0.0048	0.004	0.0045
80	13:11:32.76	-1:22:18.7	-0.404	0.0299	0.010	0.0182	-0.043	0.0117
81	13:11:30.67	-1:20:03.0	-0.158	0.0170	0.018	0.0076	-0.043	0.0067
82	13:11:36.47	-1:19:19.1	0.109	0.0077	-0.013	0.0036	0.026	0.0038
83	13:11:27.33	-1:19:50.0	0.063	0.0106	-0.021	0.0067	-0.072	0.0050
84	13:11:31.69	-1:21:16.6	-0.087	0.0155	-0.071	0.0084	-0.029	0.0076
85	13:11:26.68	-1:18:32.7	-0.165	0.0157	0.021	0.0111	0.002	0.0097
86	13:11:35.09	-1:19:13.4	0.164	0.0068	0.036	0.0037	-0.015	0.0035
87	13:11:34.24	-1:19:30.6	-0.155	0.0155	-0.009	0.0059	0.028	0.0076
88	13:11:34.07	-1:20:07.2	-0.139	0.0121	-0.037	0.0045	-0.048	0.0054
89	13:11:25.10	-1:21:24.6	0.229	0.0040	-0.014	0.0025	-0.049	0.0014
90	13:11:24.30	-1:20:55.4	-0.290	0.0157	-0.017	0.0055	-0.015	0.0068
91	13:11:26.33	-1:19:30.9	-0.189	0.0130	-0.014	0.0052	0.015	0.0058
92	13:11:34.72	-1:19:41.2	0.027	0.0097	0.010	0.0045	-0.024	0.0050
93	13:11:25.24	-1:18:59.8	-0.067	0.0108	-0.068	0.0028	0.022	0.0056
94	13:11:36.03	-1:20:21.9	0.088	0.0084	-0.068	0.0033	-0.043	0.0077
95	13:11:33.40	-1:22:03.3	-0.360	0.0160	-0.057	0.0038	-0.100	0.0064
96	13:11:31.25	-1:19:45.5	-0.367	0.0259	-0.059	0.0093	0.016	0.0172
97	13:11:31.83	-1:21:18.6	-0.299	0.0193	-0.026	0.0185	-0.069	0.0123
98	13:11:35.20	-1:20:06.1	-0.232	0.0177	-0.040	0.0078	0.075	0.0082
99	13:11:22.51	-1:20:20.6	0.499	0.0079	-0.026	0.0092	-0.099	0.0058
100	13:11:26.46	-1:20:26.4	-0.196	0.0156	0.003	0.0067	-0.039	0.0057

Table A.4: Same as Table A.2.

Object	α	$\sigma(\alpha)$	E_+	$\sigma(E_+)$	$E_\times$	$\sigma(E_\times)$
1	0.1208	0.0030	-0.261	0.0215	-0.178	0.0191
2	0.1346	0.0027	-0.235	0.0172	0.027	0.0180
3	0.1482	0.0019	-0.187	0.0088	0.541	0.0085
4	0.1039	0.0039	-0.091	0.0374	-0.121	0.0397
5	0.1325	0.0036	-0.138	0.0232	-0.288	0.0236
6	0.1139	0.0017	0.231	0.0001	0.478	0.0163
7	0.1138	0.0035	0.531	0.0231	0.063	0.0001
8	0.1463	0.0034	0.041	0.0221	0.100	0.0219
9	0.2043	0.0077	-0.013	0.0366	0.071	0.0278
10	0.2204	0.0075	-0.051	0.0214	0.482	0.0264
11	0.1356	0.0036	-0.071	0.0176	-0.506	0.0187
12	0.1013	0.0025	-0.153	0.0229	-0.254	0.0234
13	0.1627	0.0055	0.117	0.0362	0.341	0.0298
14	0.2058	0.0059	-0.295	0.0253	-0.305	0.0269
15	0.1180	0.0040	-0.093	0.0315	0.234	0.0323
16	0.2053	0.0082	0.256	0.0205	-0.420	0.0270
17	0.1524	0.0041	-0.126	0.0252	-0.043	0.0253
18	0.1467	0.0060	-0.107	0.0374	-0.168	0.0359
19	0.1722	0.0038	-0.051	0.0201	-0.011	0.0206
20	0.1823	0.0027	0.155	0.0123	0.223	0.0130
21	0.2039	0.0111	-0.313	0.0420	0.151	0.0381
22	0.1183	0.0029	-0.061	0.0247	0.022	0.0239
23	0.1039	0.0015	-0.168	0.0163	-0.440	0.0154
24	0.1597	0.0066	0.346	0.0259	0.385	0.0262
25	0.1362	0.0018	0.179	0.0124	0.032	0.0122
26	0.1192	0.0019	-0.054	0.0146	-0.093	0.0152
27	0.2638	0.0138	-0.214	0.0354	0.295	0.0346
28	0.1003	0.0019	-0.133	0.0180	-0.001	0.0174
29	0.1482	0.0023	-0.472	0.0112	-0.265	0.0115
30	0.1822	0.0088	0.281	0.0495	0.048	0.0329
31	0.1179	0.0011	-0.036	0.0086	-0.168	0.0082
32	0.1184	0.0019	0.002	0.0155	-0.295	0.0139
33	0.2332	0.0075	0.308	0.0176	-0.516	0.0184
34	0.1973	0.0064	-0.028	0.0271	0.258	0.0283

Table A.5: Fit and error values of α, E_+ and $E_\times$ for the 100 objects in the A1689 field with the best flexion estimates used in this analysis.

Object	α	$\sigma(\alpha)$	E_+	$\sigma(E_+)$	$E_\times$	$\sigma(E_\times)$
35	0.1352	0.0051	0.093	0.0364	0.101	0.0361
36	0.1613	0.0048	0.198	0.0272	0.261	0.0242
37	0.1451	0.0044	-0.482	0.0226	0.171	0.0248
38	0.1438	0.0058	0.016	0.0368	-0.174	0.0379
39	0.2255	0.0163	0.487	0.0497	0.189	0.0394
40	0.1014	0.0023	0.211	0.0001	0.412	0.0001
41	0.1963	0.0069	0.094	0.0296	-0.145	0.0332
42	0.1122	0.0027	0.006	0.0205	-0.305	0.0205
43	0.1511	0.0034	-0.117	0.0209	-0.137	0.0208
44	0.1293	0.0029	-0.252	0.0203	0.090	0.0206
45	0.1714	0.0051	0.214	0.0268	0.065	0.0248
46	0.1661	0.0036	0.094	0.0189	0.144	0.0197
47	0.1397	0.0049	-0.170	0.0344	-0.084	0.0321
48	0.2529	0.0048	-0.096	0.0158	-0.382	0.0145
49	0.1317	0.0033	-0.131	0.0227	0.211	0.0230
50	0.1549	0.0041	-0.137	0.0240	0.023	0.0256
51	0.1294	0.0021	0.132	0.0143	0.121	0.0149
52	0.1692	0.0019	0.034	0.0098	-0.271	0.0107
53	0.1196	0.0031	0.223	0.0221	0.220	0.0236
54	0.1570	0.0042	0.387	0.0345	0.077	0.0355
55	0.2950	0.0140	0.167	0.0456	-0.021	0.0253
56	0.1347	0.0040	0.183	0.0272	-0.071	0.0284
57	0.1527	0.0047	-0.013	0.0289	0.139	0.0279
58	0.1627	0.0027	0.272	0.0133	0.236	0.0137
59	0.1383	0.0041	-0.609	0.0229	0.334	0.0244
60	0.1851	0.0053	-0.151	0.0245	-0.346	0.0224
61	0.1638	0.0053	0.077	0.0307	0.011	0.0286
62	0.1665	0.0054	0.081	0.0281	-0.205	0.0297
63	0.1459	0.0025	0.175	0.0159	-0.103	0.0159
64	0.1793	0.0038	0.417	0.0001	-0.368	0.0151
65	0.1063	0.0030	-0.287	0.0251	0.008	0.0249
66	0.2283	0.0073	0.094	0.0250	-0.315	0.0274

Table A.6: Same as Table A.5

Object	α	$\sigma(\alpha)$	E_+	$\sigma(E_+)$	$E_\times$	$\sigma(E_\times)$
67	0.1487	0.0028	-0.003	0.0172	-0.190	0.0171
68	0.1229	0.0022	0.040	0.0185	-0.059	0.0167
69	0.1401	0.0029	0.023	0.0192	-0.051	0.0195
70	0.1249	0.0021	0.178	0.0164	0.085	0.0160
71	0.2797	0.0075	-0.385	0.0164	0.156	0.0285
72	0.1787	0.0102	-0.169	0.0487	0.103	0.0505
73	0.1754	0.0052	0.511	0.0211	0.112	0.0197
74	0.1667	0.0029	-0.166	0.0144	0.011	0.0160
75	0.2236	0.0068	-0.090	0.0281	-0.160	0.0248
76	0.1401	0.0066	0.075	0.0442	0.066	0.0449
77	0.1464	0.0030	-0.364	0.0158	0.085	0.0161
78	0.1436	0.0020	0.009	0.0127	0.052	0.0130
79	0.1386	0.0028	0.055	0.0185	-0.079	0.0184
80	0.1444	0.0073	0.235	0.0351	-0.470	0.0321
81	0.1592	0.0046	0.095	0.0247	-0.138	0.0268
82	0.1572	0.0021	-0.060	0.0115	0.082	0.0122
83	0.1849	0.0033	0.104	0.0156	0.061	0.0168
84	0.1802	0.0047	0.059	0.0230	0.190	0.0233
85	0.1839	0.0049	0.030	0.0234	-0.340	0.0224
86	0.1580	0.0018	0.120	0.0102	0.206	0.0101
87	0.1654	0.0044	-0.122	0.0226	-0.022	0.0247
88	0.1384	0.0029	-0.116	0.0182	-0.135	0.0195
89	0.1097	0.0008	0.301	0.0068	0.011	0.0063
90	0.1355	0.0037	-0.108	0.0264	0.087	0.0260
91	0.1386	0.0031	-0.098	0.0205	0.114	0.0209
92	0.1633	0.0027	-0.017	0.0148	-0.032	0.0154
93	0.1150	0.0023	-0.254	0.0159	-0.235	0.0176
94	0.1689	0.0024	-0.396	0.0118	0.163	0.0108
95	0.1122	0.0033	-0.324	0.0251	-0.072	0.0252
96	0.1623	0.0072	-0.246	0.0368	-0.225	0.0387
97	0.1560	0.0052	0.232	0.0244	-0.504	0.0226
98	0.1636	0.0050	-0.118	0.0275	-0.197	0.0255
99	0.2722	0.0036	0.157	0.0123	-0.112	0.0110
100	0.1482	0.0040	0.104	0.0235	-0.006	0.0252

Table A.7: Same as Table A.5

Object	Ψ_{11}	$\sigma(\Psi_{11})$	Ψ_{12}	$\sigma(\Psi_{12})$	Ψ_{31}	$\sigma(\Psi_{31})$	Ψ_{32}	$\sigma(\Psi_{32})$	SNR
1	0.1019	0.0135	0.4372	0.0062	0.3110	0.0176	-0.0305	0.0132	30.1
2	-0.0713	0.0101	0.3445	0.0073	0.0681	0.0189	0.3160	0.0157	28.3
3	0.2676	0.0065	-0.0604	0.0078	-0.0627	0.0220	-0.2778	0.0136	26.9
4	-0.3025	0.0117	0.2579	0.0125	-0.2602	0.0271	-0.1786	0.0264	23.2
5	-0.3541	0.0100	0.0433	0.0146	0.1906	0.0319	-0.1743	0.0234	20.1
6	0.2244	0.0086	0.0910	0.0090	-0.0506	0.0050	-0.3528	0.0281	19.4
7	-0.1636	0.0100	0.2755	0.0132	-0.2280	0.0541	-0.2752	0.0167	19.4
8	0.1307	0.0142	-0.2938	0.0115	0.1758	0.0274	-0.0908	0.0304	17.6
9	0.4037	0.0116	-0.0753	0.0209	0.2279	0.0284	0.0664	0.0314	17.2
10	-0.1285	0.0124	0.2814	0.0136	-0.0690	0.0230	0.3090	0.0226	16.8
11	0.0262	0.0116	0.2795	0.0137	-0.0507	0.0239	0.1544	0.0236	15.6
12	0.2194	0.0152	0.2718	0.0168	0.2696	0.0387	-0.0568	0.0497	15.4
13	-0.2660	0.0180	0.3183	0.0202	-0.0668	0.0340	0.2092	0.0365	15.3
14	0.3533	0.0129	0.1412	0.0214	-0.0213	0.0294	0.1777	0.0286	15.2
15	0.1253	0.0209	-0.3322	0.0129	0.1769	0.0415	-0.1401	0.0366	14.5
16	0.3458	0.0187	0.0250	0.0163	-0.2031	0.0216	-0.3518	0.0403	14.0
17	0.2856	0.0125	0.1105	0.0180	-0.0733	0.0339	-0.1225	0.0295	14.0
18	0.2427	0.0138	-0.2188	0.0189	0.3237	0.0378	0.1050	0.0330	14.0
19	0.2483	0.0108	-0.0691	0.0153	-0.0779	0.0278	0.1781	0.0284	13.8
20	-0.0164	0.0136	-0.2294	0.0098	-0.1063	0.0208	-0.0134	0.0228	13.7
21	0.1209	0.0154	-0.3352	0.0219	0.4371	0.0384	0.0825	0.0407	13.3
22	-0.2941	0.0179	0.1769	0.0186	0.0412	0.0414	-0.2071	0.0337	13.3
23	-0.2787	0.0176	0.0240	0.0118	0.2315	0.0592	-0.1165	0.0337	13.2
24	-0.2974	0.0118	0.0888	0.0204	0.1984	0.0217	-0.0249	0.0352	13.2
25	-0.1878	0.0137	0.1518	0.0123	0.0593	0.0297	-0.2750	0.0278	13.1
26	-0.0135	0.0230	0.3117	0.0075	-0.0589	0.0324	0.0965	0.0254	12.9
27	-0.0467	0.0187	0.3443	0.0199	-0.2444	0.0393	0.0198	0.0254	12.7
28	0.1819	0.0148	-0.2698	0.0217	0.3238	0.0271	-0.2128	0.0412	12.4
29	-0.2491	0.0135	-0.0714	0.0165	-0.0634	0.0281	-0.2922	0.0282	12.1
30	0.2823	0.0198	-0.2490	0.0241	0.4248	0.0469	0.0513	0.0357	12.1
31	-0.1858	0.0156	-0.1703	0.0141	0.0781	0.0293	-0.0488	0.0288	12.0
32	0.1937	0.0172	0.2272	0.0182	0.0734	0.0405	0.0033	0.0381	11.9
33	0.1441	0.0174	0.2118	0.0128	-0.1850	0.0159	-0.1086	0.0253	11.8
34	0.2747	0.0127	-0.0885	0.0216	-0.0702	0.0321	-0.0090	0.0331	11.5

Table A.8: Fit flexion parameters and their errors for the 100 best A1689 1-flexion objects. The fixed input shears used for the image fits are included for reference.

Object	Ψ_{11}	$\sigma(\Psi_{11})$	Ψ_{12}	$\sigma(\Psi_{12})$	Ψ_{31}	$\sigma(\Psi_{31})$	Ψ_{32}	$\sigma(\Psi_{32})$	SNR
35	-0.1396	0.0253	0.3110	0.0161	-0.1695	0.0438	0.0333	0.0484	11.4
36	0.1976	0.0202	-0.2281	0.0174	-0.0699	0.0362	0.1195	0.0357	11.3
37	-0.3574	0.0117	0.0873	0.0304	-0.1769	0.0332	0.1083	0.0338	11.3
38	-0.0099	0.0224	0.3127	0.0172	-0.2097	0.0492	0.2316	0.0381	11.1
39	-0.0631	0.0217	-0.2864	0.0155	-0.2332	0.0321	0.1420	0.0232	11.0
40	-0.3045	0.0117	0.1145	0.0298	0.1972	0.0284	0.0228	0.0510	10.2
41	0.0404	0.0215	0.2661	0.0157	0.0730	0.0388	0.1218	0.0377	10.1
42	-0.3210	0.0196	0.0928	0.0267	0.1237	0.0461	-0.1647	0.0285	10.1
43	-0.2462	0.0172	-0.1020	0.0200	0.0287	0.0394	0.1390	0.0413	10.1
44	-0.2832	0.0244	0.0936	0.0169	0.1417	0.0513	-0.1088	0.0383	10.1
45	-0.1834	0.0190	0.1914	0.0188	-0.0169	0.0391	-0.1522	0.0352	9.9
46	0.2217	0.0138	-0.0147	0.0179	-0.2007	0.0282	-0.2163	0.0360	9.8
47	0.2613	0.0154	0.1638	0.0282	0.3524	0.0542	-0.1181	0.0366	9.6
48	0.1407	0.0123	0.1309	0.0161	0.1023	0.0247	0.1262	0.0217	9.5
49	-0.1030	0.0266	0.2677	0.0152	-0.0304	0.0474	0.1991	0.0399	9.4
50	0.2632	0.0162	-0.0545	0.0245	-0.0638	0.0429	0.0844	0.0436	9.2
51	-0.0407	0.0243	-0.2622	0.0161	-0.0596	0.0375	0.0340	0.0398	9.1
52	-0.1099	0.0115	-0.1256	0.0147	0.1264	0.0248	-0.2951	0.0259	8.9
53	-0.0382	0.0260	0.3045	0.0228	0.0169	0.0541	0.1426	0.0555	8.9
54	-0.1122	0.0137	-0.2069	0.0234	-0.1217	0.0713	0.4128	0.0506	8.7
55	-0.2830	0.0210	-0.0518	0.0261	-0.3456	0.0495	0.0639	0.0349	8.6
56	-0.0478	0.0297	0.2916	0.0178	-0.1781	0.0529	0.0172	0.0499	8.5
57	0.2255	0.0187	0.1110	0.0230	0.0287	0.0491	-0.2523	0.0420	8.5
58	0.1826	0.0127	-0.1022	0.0211	-0.1775	0.0265	-0.0787	0.0333	8.5
59	-0.2361	0.0230	0.1662	0.0251	-0.2261	0.0633	0.2519	0.0503	8.5
60	0.1538	0.0170	0.1877	0.0231	0.2001	0.0436	0.1187	0.0351	8.5
61	0.1749	0.0261	0.1951	0.0184	-0.0224	0.0432	-0.2290	0.0436	8.2
62	-0.0805	0.0268	-0.2600	0.0202	0.0262	0.0473	-0.1102	0.0472	8.1
63	0.1348	0.0228	0.1732	0.0162	-0.1529	0.0403	-0.1907	0.0378	7.8
64	-0.0141	0.0024	-0.1296	0.0166	0.2121	0.0403	-0.0579	0.0094	7.8
65	0.0595	0.0363	-0.2991	0.0153	0.1365	0.0646	-0.2469	0.0458	7.7
66	-0.0874	0.0216	-0.2257	0.0230	-0.0198	0.0380	-0.1731	0.0403	7.7

Table A.9: Same as Table A.8

Object	Ψ_{11}	$\sigma(\Psi_{11})$	Ψ_{12}	$\sigma(\Psi_{12})$	Ψ_{31}	$\sigma(\Psi_{31})$	Ψ_{32}	$\sigma(\Psi_{32})$	SNR
67	-0.0054	0.0308	-0.2513	0.0115	0.1194	0.0351	0.2302	0.0373	7.6
68	-0.1392	0.0222	-0.1750	0.0191	-0.3176	0.0409	0.3845	0.0512	7.6
69	-0.0566	0.0235	0.2244	0.0194	-0.2064	0.0465	0.0990	0.0464	7.6
70	-0.0020	0.0246	0.2381	0.0196	0.3534	0.0483	-0.0244	0.0376	7.6
71	-0.1555	0.0189	-0.1559	0.0221	0.3727	0.0346	-0.0110	0.0314	7.6
72	0.1279	0.0260	-0.2609	0.0289	0.1964	0.0528	-0.2083	0.0600	7.5
73	-0.1098	0.0266	0.2165	0.0189	-0.0365	0.0475	-0.2428	0.0344	7.4
74	-0.0086	0.0205	-0.1864	0.0144	-0.0063	0.0345	-0.1848	0.0314	7.4
75	0.1590	0.0204	0.1375	0.0204	0.0576	0.0382	-0.0371	0.0383	7.3
76	0.1060	0.0414	-0.3162	0.0205	0.1026	0.0596	0.0009	0.0635	7.2
77	0.0786	0.0302	-0.2191	0.0117	0.0042	0.0398	-0.1252	0.0294	7.2
78	-0.0894	0.0203	0.1769	0.0187	0.0316	0.0370	0.0988	0.0369	7.2
79	-0.2117	0.0215	-0.1107	0.0258	0.0784	0.0473	0.1061	0.0471	7.1
80	-0.0207	0.0327	0.2765	0.0216	-0.3449	0.0444	0.0471	0.0687	7.1
81	-0.2330	0.0207	-0.0527	0.0278	0.2003	0.0463	-0.0058	0.0508	6.9
82	-0.0594	0.0197	-0.1636	0.0161	0.0646	0.0316	-0.1059	0.0310	6.8
83	-0.0139	0.0190	0.1732	0.0176	0.0059	0.0348	0.0631	0.0348	6.7
84	0.1828	0.0215	-0.0984	0.0229	-0.1155	0.0421	0.1206	0.0450	6.6
85	-0.1582	0.0273	-0.1530	0.0193	0.1705	0.0422	0.1138	0.0469	6.6
86	-0.1588	0.0125	0.0146	0.0211	-0.0465	0.0295	0.0726	0.0277	6.5
87	-0.0650	0.0242	-0.1993	0.0217	-0.1092	0.0470	-0.2157	0.0462	6.4
88	0.0660	0.0269	0.2113	0.0214	0.0317	0.0515	0.2176	0.0467	6.4
89	-0.0197	0.0157	0.1715	0.0222	0.1659	0.0320	-0.2067	0.0315	6.4
90	-0.2351	0.0293	-0.0164	0.0231	0.1881	0.0490	0.4242	0.0656	6.3
91	0.1010	0.0304	-0.2173	0.0230	-0.0210	0.0528	-0.1619	0.0505	6.3
92	-0.1712	0.0188	0.0433	0.0211	0.0678	0.0379	-0.0682	0.0375	6.3
93	0.2826	0.0327	-0.0087	0.0328	-0.0296	0.0505	0.0079	0.0594	6.1
94	0.1702	0.0235	0.0173	0.0154	0.1003	0.0314	-0.2146	0.0306	6.1
95	0.0634	0.0422	0.2708	0.0174	0.0332	0.0645	0.2354	0.0510	6.1
96	0.2667	0.0245	0.0014	0.0365	-0.0319	0.0629	0.2073	0.0618	6.1
97	0.0799	0.0316	0.2231	0.0231	-0.3264	0.0420	0.0869	0.0575	6.1
98	-0.1041	0.0370	-0.2261	0.0179	-0.1269	0.0462	0.0921	0.0507	6.1
99	0.0148	0.0139	0.1073	0.0113	0.0013	0.0210	-0.1288	0.0210	6.0
100	-0.2200	0.0234	-0.0410	0.0293	0.1956	0.0512	0.1602	0.0566	6.0

Table A.10: Same as Table A.8

Bibliography

Anders, E. & Grevesse, N. 1989, GeCoA, 53, 197.

Andersson, K.E., & Madejski, G.M. 2004, ApJ, 607, 190.

Arnaud, K. A. Astronomical Data Analysis Software and Systems V, eds. Jacoby, G. & Barnes J. 1996, ASPC, 101, 17.

Arnaud, M. & Evrard, A. E. 1999, MNRAS, 305, 631.

Astier,P., et al. 2006, A&A, 447, 31.

Bacon, D.J., Goldberg, D.M., Rowe, B.T.P., & Taylor, A.N. 2006, MNRAS, 365, 414.

Barrientos, L. F., Gladders, M. D., Yee, H. K. C., Infante, L., Ellingson, E., Hall, P. B. & Hertling, G. 2004, ApJ, 617, L17.

Bartelmann, M., & Schneider, P. 2001, Phys. Reports, 340, 291.

Bertin, E., & Arnouts, S. 1996, A&AS, 117, 393.

Blindert, K., Yee, H. K. C., Ellingson, E., Gladders, M. D., Gilbank, D. G. & Barrientos, L. F., 2007, ApJS, submitted.

Blindert, K. et al. 2008. In preparation.

Bower, R.G., Lucey, J.R., & Ellis, R.S. 1992, MNRAS, 254, 601.

Bower, R. G., Böhringer, H., Briel, U. G., Ellis, R. S., Castander, F. J. & Couch, W. J. 1994, MNRAS, 268, 345.

Broadhurst, T., et al. 2005, ApJ, 621 53.

Brodwin, M., et al. 2010, ApJ, 721, 90.

Bryan, G. L. & Norman, M. L. 1998, ApJ, 495, 80.

Cain, B., et al. 2008, ApJ, 679, 293.

Carlberg, R. G., et al. 1997, ApJ, 476, L7.

Cavaliere, A. & Fusco-Femiano, R. 1976, A&A, 49, 137.

Clowe, D., Bradač, M., Gonzalez, A.H., Markevitch, M., Randall, S.W., Jones, C., & Zaritsky, D. 2006, ApJ, 648, L109.

Coe, D., et al. astro-ph/1005.0398

Coe, D., Fuselier, E., Benítez, N., Broadhurst, T., Frye, B., & Ford, H. 2008, ApJ, 681, 814.

Cohn, J. D., Evrard, A. E., White, M., Croton, D. & Ellingson, E. 2007, MNRAS, 382, 1738.

Dickey, J. M. & Lockman, F. J. 1990, ARA&A, 28, 215.

Diego, J.M., Sandvik, H.B., Protopapas, P., Tegmark, M., Benítez, N., & Broadhurst, T. 2005, MNRAS, 362, 1247.

Duc, P.-A., et al. 2002, A&A, 382, 60.

Dunkley, J., et al. 2009, ApJS, 180, 306.

Donahue, M., et al. 2001, ApJ, 552, L93.

Ettori, S., et al. 2004, MNRAS, 354, 111.

Falco, E.E., Gorenstein, M.V., & Shapiro, I.I. 1985, ApJ, 289, L1.

Frye, B.L., et al. 2007, ApJ, 665, 921.

Gladders, M. D. 2002, Ph.D. Thesis, University of Toronto.

Gladders, M. D. & Yee, H. K. C. 2005, ApJS, 157, 1.

Gladders, M. D., Yee, H. K. C., Majumdar, S., Barrientos, L. F., Hoekstra, H., Hall, P. B. & Infante, L. 2007, ApJ, 655, 128.

Gilbank, D. G., Bower, R. G., Castander, F. J. & Ziegler, B. L. 2004, MNRAS, 348, 551.

Gilbank, D. G., Yee, H. K. C., Ellingson, E., Gladders, M. D., Barrientos, L. F. & Blindert, K. 2007, AJ, 134, 282.

Goldber, D.M., & Bacon, D.J. 2005, ApJ, 619, 741.

Goldberg, D.M., & Leonard, A. 2007, ApJ, 660, 1003.

Goldberg, D.M., & Natarajan, P. 2002, ApJ, 564, 65.

Hicks, A. K., Ellingson, E., Bautz, M., Yee, H. K. C., Gladders, M. & Garmire, G. 2004, AdSpR, 36, 706.

Hicks, A. K., Ellingson, E., Hoekstra, H. & Yee, H. K. C. 2006, ApJ, 652, 232.

Hicks, A.K., Ellingson, E., Bautz, M., Cain, B., Gilbank, D.G., Gladders, M.G., Hoekstra, H., Yee, H.K.C., & Garmire, G. 2008, ApJ, 680, 1022.

Hogg, D.W. astro-ph/9905116

Irwin, J., & Shmakova, M. 2005, New Astr. Rev., 49, 83.

Irwin, J., & Shmakova, M. 2006, ApJ, 645, 17.

Jee, M. J., et al. 2007, ApJ, 661, 728.

Jeltema, T. E., Canizares, C. R., Bautz, M. W. & Buote, D. A. 2005, ApJ, 624, 606.

Jenkins, A., et al. 2001, MNRAS, 321, 372.

Kaiser, N., Squires, G., & Broadhurst, T. 1995, ApJ, 449, 460.

Koester, B. P., et al. 2007, ApJ, 660, 239.

Kravtsov, A. V., Vikhlinin, A. & Nagai, D. 2006, ApJ, 650, 128.

Krist, J. 1993, ASP Conf. Series 52, Astr. Data Analysis & Software Syst. II, 536.

Lasky, P.D., & Fluke, C.J. 2009, MNRAS, 396, 2257.

Leonard, A., Goldberg, D.M., Haaga, J.L., & Massey, R. 2007, ApJ, 666, 51.

Leonard, A., King, L.J., & Wilkins, S.M. 2009, MNRAS, 395, 1438.

Leonard, A., King, L.J., & Goldberg, D.M. astro-ph/1009.1018

Lin, Y.-T., Mohr, J. J. & Stanford, S. A. 2003, ApJ 591, 749.

Longair, M. S. & Seldner, M. 1979, MNRAS, 189, 433.

Lopes, P. A. A., de Carvalho, R. R., Capelato, H. V., Gal, R. R., Djorgovski, S. G., Brunner, R. J., Odewahn, S. C. & Mahabal, A. A. 2006, ApJ, 648, 209.

Lubin, L. M., Oke, J. B. & Postman, M. 2002, AJ, 124, 1905.

Mantz, A., Allen, S.W., Ebeling, H., & Rapetti, D. 2008, MNRAS, 387, 1187.

Mantz, A., Allen, S.W., Rapetti, D. & Ebeling, H. 2010, MNRAS, 406, 1759.

Massey, R., Rowe, B., Refregier, A., Bacon, D.J., & Bergé, J. 2007, MNRAS, 380, 229.

Markwardt, C. B. 2009, ASP Conf. Series, 411, 251.

Mason, B.S., et al. 2010, ApJ, 716, 739.

Mathiesen, B. F. & Evrard, A. E. 2001, ApJ, 546, 100.

Maughan, B. J., Jones, L. R., Ebeling, H. & Scharf, C. 2006, MNRAS, 365, 509.

Melchior, P., Böhnert, A., Lombardi, M., & Bartelmann, M. 2010, A&A, 510, 75.

Mewe, R., Gronenschild, E. H. B. M. & van den Oord, G. H. J. 1985, A&AS, 62, 197.

Mewe, R., Lemen, J. R. & van den Oord, G. H. J. 1986, A&AS, 65, 511.

Motl, P.M., Hallman, E.J., Burns, J.O., & Norman, M.L. 2005, ApJ, 623, L63.

Nagai, D., Kravtsov, A. V. & Vikhlinin, A. 2007, ApJ, 668, 1.

Navarro, J., Frenk, C.S., & White, S.D.M. 1997, ApJ, 490, 493.

Neumann, D. M. 2005, A&A, 439, 465.

Newman, A.B., et al. 2009, ApJ 706, 1078.

Okura, Y., Umetsu, K., & Futamase, T. 2007, ApJ, 660, 995.

Okura, Y., Umetsu, K., & Futamase, T. 2008, ApJ, 680, 1.

Peng, E.-H., Andersson, K., Bautz, M.W., & Garmire, G.P. 2009, ApJ, 701, 1283.

Peng, C.Y., Ho, L.C., Impey, C.D., & Rix, H.-W. 2010, AJ, 139, 2097.

Popesso, P., Böhringer, H., Brinkmann, J., Voges, W. & York, D. G. 2004, A&A, 423, 449.

Refregier, A. 2003, MNRAS, 338, 35.

Refregier, A., & Bacon, D.J. 2003, MNRAS, 338, 48.

Rix, H.-W., et al. 2004, ApJS, 152, 163.

Rosati, P., Borgani, S. & Norman, C. 2002, ARA&A, 40, 539.

Sadat, R., et al. 2005, A&A, 437, 31.

Sandage, A. 1972, ApJ, 176, 21.

Sirianni, M., et al. 2005, PASP, 117, 1049.

Saha, P., Williams, L.L.R., & Ferreras, I. 2007, 663, 29.

Sanderson, A. J. R., Ponman, T. J., Finoguenov, A., Lloyd-Davies, E. J. & Markevitch, M. 2003, MNRAS, 340, 989.

Schneider, P. 1996, MNRAS, 283, 837.

Schneider, P., van Waerbeke, L., Jain, B., & Kruse, G. 1998, MNRAS, 296, 873.

Schneider, P., & Er, X. 2008, A&A, 485, 363.

Spergel, D.N., et al. 2007, ApJS, 170, 377.

Tinker, J., et al. 2008, ApJ, 688, 709.

Vikhlinin, A., et al. 2003, ApJ, 590, 15.

Vikhlinin, A., Kravtsov, A., Forman, W., Jones, C., Markevitch, M., Murray, S. S. & Van Speybroeck, L. 2006, ApJ, 640, 691.

Vikhlinin, A., et al. 2009, ApJ, 692, 1060.

Wen, Z.L., Han, J.L., & Liu, F.S. 2010, MNRAS 407, 533.

White, S. D. M., Navarro, J. F., Evrard, A. E. & Frenk, C. S. 1993, Nature, 366, 429.

Yee, H. K. C. & López-Cruz, O. 1999, AJ, 117, 1985.

Yee, H. K. C. & Ellingson, E. 2003, ApJ, 585, 215.

Zwicky, F. 1937, ApJ, 86, 217.